STRUCTURE AND MAGNETIC PROPERTIES OF MECHANICALLY ALLOYED NANOCRYSTALLINE Fe-Si (- M) [M=Al, B, Cr] POWDERS

A thesis submitted

by

Manos Pratim Chakrapani Kalita

to

Indian Institute of Technology Guwahati

in

partial fulfillment of the requirement for the award of the degree of
Doctor of Philosophy in Physics

Department of Physics
Indian Institute of Technology Guwahati
Guwahati – 781039, Assam, India

November 2008

Statement

The work contained in the thesis entitled "Structure and magnetic properties of mechanically alloyed nanocrystalline Fe-Si(-M) [M=Al, B, Cr] powders" has been carried out by me under the supervision of Prof. A. Srinivasan and Dr. A. Perumal, at Department of Physics Indian Institute of Technology Guwahati. This work has not been submitted elsewhere for the award of any degree.

Manos Pratim Chakrapani Kalita

12 November 2008

(Manos Pratim Chakrapani Kalita)

Roll No: 04612105

Department of Physics

Indian Institute of Technology Guwahati

Guwahati - 781039

Certificate

It is certified that the work contained in the thesis entitled “Structure and magnetic properties of mechanically alloyed nanocrystalline Fe-Si(-M) [M=Al, B, Cr] powders” submitted by Manos Pratim Chakrapani Kalita, a Ph. D. student of the Department of Physics, Indian Institute of Technology Guwahati for the award of degree of Doctor of Philosophy has been carried out under the supervision of myself and Dr A. Perumal. This work has not been submitted elsewhere for the award of any degree.

12 November 2008

(Dr. A. Srinivasan)

Professor

Department of Physics

Indian Institute of Technology Guwahati

Guwahati – 781039

Certificate

It is certified that the work contained in the thesis entitled "Structure and magnetic properties of mechanically alloyed nanocrystalline Fe-Si(-M) [M=Al, B, Cr] powders" submitted by Manos Pratim Chakrapani Kalita, a Ph. D. student of the Department of Physics, Indian Institute of Technology Guwahati for the award of degree of Doctor of Philosophy has been carried out under the supervision of myself and Dr A. Srinivasan. This work has not been submitted elsewhere for the award of any degree.

15 May 2009

(Dr. A. Perumal)

Associate Professor

Department of Physics

Indian Institute of Technology Guwahati

Guwahati – 781039

Dedicated

to

my parents

Acknowledgements

At the outset, I would like to express my deepest gratitude to my thesis supervisors Prof. A. Srinivasan and Dr. A. Perumal for giving me the opportunity to carry out my Ph.D. thesis work under their supervision. I am grateful to them for introducing me to the world of nanostructured magnetic materials and for their keen interest in the progress of my thesis work. I am especially thankful to Srinivasan Sir for his constant encouragement, confidence and patience with me through all the years of my studentship.

I am grateful to my doctoral committee members, Dr. S. Ravi, Dr. P. K. Giri and Dr. G. Krishnamoorty for reviewing my research work regularly and for all their valuable suggestions for my doctoral research. I am thankful to the Head of the Department, Prof. A. Khare and all the faculty members of the Department of Physics for their support.

I express my sincere thanks to the staff members of Physics Department, Mr. Sidananda Sarma, Mr. Lokesh Chakraborty, Mr. Atul Deka, Mr. Bimal K. Sarma, Mr. Pankaj Goswami, Mr. Jyoti Bora and Mr. Modan Deka for their relentless support and cooperation during the course of my Ph.D. work. Jon was always there to help me in moving heavy equipment between laboratories.

Mr. Chandan Borgohain and Mr. Kula Senapati, Scientific Officers of CIF, and all the members of mechanical workshop have patiently and enthusiastically extended their expertise in SEM/TEM imaging work and in fabrication of essential components required for my research work.

I am fortunate to have Sida da, Debabrata and Rajendra as my fellow researchers in the same group. Thanks to them for providing an amiable ambience in the lab. Anto, Sandeep, Amal da, Purabi ba, Santanu da, Poulumi, Bishwanath, Gaurav, Mera, Veena, Samantray, Arpita, Annesh and all the research scholars of Physics Department will always be remembered for the wonderful time we shared together.

I thank Rajen, Rajesh, Gunin, Bolin, Ballav, Sonit and all my friends for the memorable life in IITG campus.

I am deeply indebted to my parents and brothers for their support and encouragements. Finally, my sincere thanks are due to all those who have helped me in whatever manner during my Ph.D. work, some of whom I may have inadvertently forgotten to mention in this acknowledgement.

M. P. C. Kalita

PREFACE

Fe-Si based alloys are traditionally well known soft magnetic materials which find applications in split-core current transformers, magnetic cores of electrical appliances, magneto-fluids, magnetic shielding, electromagnetic noise suppression, *etc.* Nanocrystalline materials prepared from melt-spun amorphous precursors with the average crystallite size less than the ferromagnetic exchange length exhibit ultra soft magnetic properties with very low coercivity ~10^{-3} Oe. Mechanical alloying (MA) is an alternate and commercially viable route for preparing nanocrystalline materials. Preparing mechanically alloyed soft magnetic nanocrystalline Fe-Si powders and understanding the correlation between the structure and magnetic properties of these materials are important from basic physics as well as application view points.

This thesis work aims to understand (i) the correlation between the microstructure and magnetic properties of mechanically alloyed Fe-Si based nanocrystalline materials and (ii) to explore the possibility of improving their soft magnetic properties. The following atomic compositions were studied in the present work: $Fe_{75}Si_{25-x}M_x$ (x = 0, 5, 10; M = Al, B, Cr).

The thesis work is presented in six chapters. The first chapter serves as a general introduction to the materials of interest to this thesis work, the theoretical formalisms relevant to them and the content of the thesis. The experimental techniques used in the preparation, processing and characterization of Fe-Si-M powders are discussed in the second chapter.

In the third chapter, the results and discussion on Fe-Si and Fe-Si-M (M = Al, B, Cr) powders milled for various time periods have been presented. Milling was carried out for 80

hours in a planetary ball mill. MA was found to produce non-equilibrium solid solution α–Fe (Si) in case of $Fe_{75}Si_{25}$ powders with an average crystallite size of about 10 nm and dislocation density of 10^{18} m^{-2} after 80 hours of milling. The 80 hours milled powders showed coercivity of 128 Oe. An increase of coercivity with increasing milling time periods was observed, which has been mainly attributed to the introduction of dislocations and the reduction of average particle sizes in the course of the milling process. Domain wall pinning results increased coercivity in the milled powders. The Curie temperature (T_C) of the powders milled for 80 hours was found to be higher than that of melt-spun ribbons of similar compositions. Such higher T_C has been attributed to the lattice distortions caused by the presence of strain in the powders, induced during MA process. Similar studies were carried out on $Fe_{75}Si_{25-x}M_x$ (x = 5, 10) powder compositions, which also showed good correlations between the structure and magnetic properties. However, the structural and magnetic parameters were different for different alloy compositions.

In the fourth chapter, the results and discussion on heat-treated nanocrystalline Fe-Si and Fe-Si-M (M = Al, B, Cr) powders have been detailed. Annealing has been found to have a significant effect on the microstructure and improvement of the soft magnetic properties of the powders. Annealing resulted in a gradual transformation of the disordered α-Fe(Si) phase of as-milled powders to ordered DO_3 superlattice phase in the case of $Fe_{75}Si_{25}$ powders, as revealed by X-ray diffraction (XRD) studies. In a particular range of annealing temperatures, coercivity varied as the sixth power of crystallite size, revealing the influence of nanocrystallites present in the powders. However, coercivity was in the range of 50 Oe to 100 Oe in the annealed powders. Similar studies have also been carried out on $Fe_{75}Si_{25-x}M_x$ (x = 5, 10) powder compositions. These powders exhibited microstructure quite similar to

$Fe_{75}Si_{25}$. But their structural and magnetic parameters were dependent on alloy compositions. Coercivity of $Fe_{75}Si_{15}Al_{10}$ powders annealed at 1223 K for 4 hours yielded the lowest coercivity value of 9 Oe amongst all the samples. These results show that the presence of strain introduced during MA could not be completely relieved by the annealing procedure adopted.

The fifth chapter contains the results and discussion on the microstructure and magnetic properties of nanocrystalline Fe-Si-Cr powders prepared from mechanically alloyed amorphous precursor. Amorphous $Fe_{75}Si_{15}Cr_{10}$ powders were obtained by MA. Non-equilibrium solid solution α-Fe(Si,Cr) with nanocrystalline structure could be produced by annealing the as-milled amorphous powders near and above the crystallization temperature. A progressive increase in coercivity with increasing crystallite size, even beyond the ferromagnetic exchange length of Fe-Si alloys was seen. Hence, no improvement in the soft magnetic properties of the nanocrystalline powders was observed in these ternary alloy powders. This behavior has been attributed to the possible stresses induced in the nanocrystallites during annealing. Presence of domain wall pinning in both the amorphous and nanocrystalline powders might have also contributed to the observed high coercivity of the powders. The above results have been used to understand the evolution of the structure and magnetic properties of as-milled and heat-treated Fe-Si and Fe-Si-M powders.

Conclusions and scope of future work on these materials are presented in the last chapter. The references cited in the thesis are listed at the end of the thesis.

Contents

Chapter 1

Introduction

During the last few decades, research on soft magnetic materials has shifted its focus from coarser grained materials to amorphous and nanocrystalline materials. While amorphous materials do not exhibit long range translational periodicity, nanocrystalline materials have crystallite sizes ranging from a few nanometers to several tens of nanometer. The coercive field or simply coercivity, is known to depend on the composition and microstructure of the material, and is commonly used as a key parameter in characterizing magnetic materials as either 'soft' or 'hard'. However, soft and hard magnetic materials are classified quite arbitrarily. Usually, materials with coercivity less than 100 Oe are considered to be soft, while those with coercivity above 1000 Oe are termed hard magnetic materials. In the early days, magnetic materials were mainly prepared by casting process. These early magnetic materials are known to get harder (*i.e.* exhibit an increase in coercivity) with a decrease in their crystallite size [1]. Therefore, early research activities on soft magnetic materials were mainly confined to the development of appropriate alloys with large crystallite sizes, so that materials with better soft magnetic properties could be obtained [2]. However, this approach changed after the

discovery of amorphous soft magnetic materials prepared by rapid solidification technique [3] and more recently after the advent of ultra fine magnetic materials with crystallite size of the order of 10 nm prepared by controlled crystallization of melt-spun amorphous precursor [4].

Fe-Si based alloys are one of the earliest known and widely used soft magnetic alloys [5]. These alloys are commonly used in transformer cores, electromagnets, magnetic recording media, *etc.* [6]. Nanocrystalline Fe-Si based alloys derived from melt-spun amorphous ribbons exhibit ultra soft magnetic properties and therefore are very important from technological point of view [1]. Mechanical alloying is an alternative and commercially viable technique for the mass production of nanocrystalline alloys in powder form [7]. Preparing mechanically alloyed soft magnetic nanocrystalline Fe-Si powders and understanding the correlation between the structure and magnetic properties of these materials are important from basic physics as well as application view points.

1.1. Ferromagnetic materials

Ferromagnetic materials are spontaneously magnetized materials that exhibit a large magnetization when placed in a small magnetic field. The response of a ferromagnetic material to an applied magnetic field is non-linear and is characterized by a hysteresis phenomenon as shown in Figure 1.1. The dotted curve OA shows the initial magnetization curve of a demagnetized material. The magnetization increases with increasing applied magnetic field and saturates at higher magnetic fields. The maximum (saturated) magnetization achievable is known as saturation magnetization M_S. The typical hystersis loop of a ferromagnetic material is shown by the solid curve ABA in

Figure 1.1. Significant parameters characterizing a magnetic material associated with the hysteresis loop are remanence M_R (value of magnetization when $\boldsymbol{H}$=0) and coercivity H_C (reverse magnetic field required to reduce the net magnetization to zero or to demagnetize the material). Another important parameter is the magnetic induction $\boldsymbol{B}$ [= $\mu_o(\boldsymbol{H} + \boldsymbol{M})$, where μ_o is the permeability of free space], which is the total flux of magnetic field lines through a unit cross sectional area of the material. Saturation magnetization M_S is also expressed as $J_S=\mu_o M_S$, where J_S is known as saturation polarization. From the initial magnetization curve, the initial magnetic permeability μ_I (= B/H, for very small applied magnetic field) and maximum permeability $\mu_{max}=(B/H)_{max}$ can be obtained. These parameters indicate the amount of induction generated by the material in a given magnetic field, and are useful in characterizing magnetic materials. Initial permeability and coercivity have a reciprocal relationship. So, materials exhibiting low coercivity necessarily have a high initial permeability.

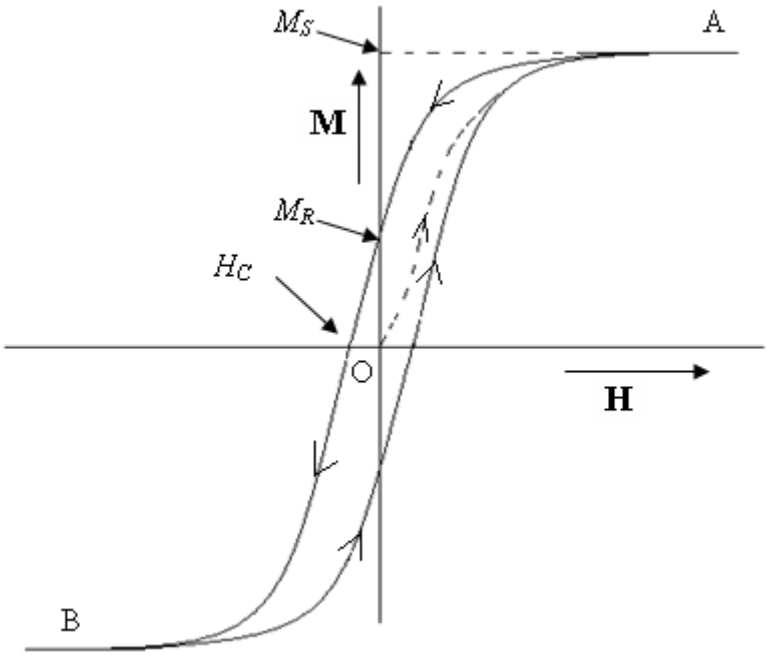

Figure 1.1: Response of a ferromagnetic material to the applied magnetic field.

All ferromagnetic materials become paramagnetic above a particular temperature. The temperature at which the transition from ferromagnetic to paramagnetic phase occurs is known as Curie temperature, which is also an important parameter characterizing a ferromagnetic material.

1.2. Soft magnetic materials and their applications

As mentioned earlier, soft magnetic materials (SMM) belong to a class of ferromagnetic materials which can be easily magnetized and demagnetized. SMM are characterized by high saturation magnetization and narrow hysteresis loops, *i.e.* low coercivity.

The applications of SMM fall into two broad categories, *viz.* AC and DC applications. For AC applications, the important consideration is how much energy is lost in the system as the material is cycled around its hysteresis loop. The energy loss originates from two main sources *viz.* hysteresis loss (which is the area enclosed by the hysteresis loop) and eddy current loss (which is related to the generation of electric currents in the magnetic material and the associated resistive losses). Hysteresis losses can be reduced by the reduction of the coercivity, with a consequent reduction in the area enclosed by the hysteresis loop. Eddy current losses can be reduced by increasing the electrical resistivity of the material and by laminating the material. In DC applications, the material is magnetized in order to perform an operation and then demagnetized at the conclusion of the operation.

The development of SMM has been mainly driven by the search for superior soft magnetic alloys and to meet the requirements of applications. Recent research has been focused on achieving materials with low coercivity, high permeability and high saturation

magnetization in a cost effective way. The continuing development of better materials has considerably improved the efficiency of key building blocks of present electrical appliances like motors, generators, transformers, inductors, *etc.*

1.2.1. Conventional soft magnetic alloys

Among the soft magnetic alloys (SMA) which find wide applications, Fe-Si is one of the earliest to be discovered. Barrett *et al.* [5] reported the improvement in the soft magnetic properties of Fe with the addition of Si in 1900. Significant progress occurred after the discovery of grain-oriented Fe-Si alloys and Ni-Fe alloys such as permalloy in the 1940s [8]. The range of SMM was further extended by the development of ferrites in the 1950s [8]. The major families of the conventional SMA with important applications are briefly discussed below.

Fe-Si alloys: In electrical power generation and transmission, the highest demand is for transformer cores. Fe-Si alloys are used for transformer cores in exclusion of all other SMA and are commonly known as 'electrical steels' or 'silicon steels'. In the power industry, electrical voltage is almost always AC and at low frequency (50 - 60 Hz). At these frequencies, eddy currents are generated in the transformer core. Silicon is a less costly and easily available material and therefore gets importance to meet the huge demands of transformer core materials in large quantities. Addition of Si in Fe reduces the magnetocrystalline anisotropy and magnetostriction (*i.e.* length change on magnetization) of Fe and thereby reduces the coercivity. Further, the resisitivity of Fe increases with the addition of Si and thereby reduces the eddy current losses. The addition of too much of Si makes the material extremely brittle and difficult to produce,

resulting in a practical limitation of the additive to 4 wt %. Often Al is added in Fe-Si alloys to increase the ductility of the alloy. Alloys with atomic composition $Fe_{75}Si_{15}Al_{10}$ (known as Sendust) are used as electrical steels for some special applications. Selected magnetic properties of some Fe-Si alloys are listed in Table 1.1.

Table 1.1: Selected magnetic properties of some Fe-Si alloys [Ref. 6].

Fe-Si Alloy	**Composition**	**Maximum Permeability, μ_{max}**	**Coercivity, H_C (Oe)**	**Saturation Polarization, J_S (T)**
Fe-Si (Non-oriented)	$Fe_{96}Si_4$	4000 - 15000	0.4 - 1.5	2.1
Fe-Si (Non-oriented)	$Fe_{97.5}Si_{2.5}$	4000 - 12000	0.15 - 1.5	2.0
Fe-Si (Non-oriented)	$Fe_{96}Si_4$	5000 - 20000	0.5 - 1	2.0
Fe-Si (Grain-oriented)	$Fe_{97}Si_3$	40000	0.1	2.0

Ni-Fe alloys: These alloys, known as permalloy, are extremely versatile and are used over a wide range of compositions (from 30 to 80 wt% Ni). Over this composition range, the properties vary considerably and the optimum composition must be selected for a particular application. There are special grades of Ni-Fe alloys that have zero magnetostriction and zero magnetic anisotropy, such as mumetal which is produced by a careful heat treatment and minor additions of Cu and Cr. These alloys have extremely high relative permeability (up to 300000), and coercivity as low as 0.005 Oe. However, low saturation magnetization and the high cost of Ni as compared to Si limits these alloys

only for some special applications. Selected magnetic properties of some Ni-Fe alloys are listed in Table 1.2.

Table 1.2: Selected magnetic properties of some Ni-Fe alloys [Ref. 6].

Alloy	**Composition**	**Maximum Permeability, μ_{max}**	**Coercivity, H_C (Oe)**	**Saturation Polarization, J_S (T)**
78 Permalloy	$Ni_{78}Fe_{22}$	8000	0.05	1.08
Hipernik	$Ni_{50}Fe_{50}$	4000	0.05	1.60
Supermalloy	$Ni_{79}Fe_{16}Mo_5$	100000	0.005	0.79
Mumetal	$Ni_{77}Fe_{16}Cu_5Cr_2$	20000	0.05	0.65

Table 1.3: Selected magnetic properties of some Fe-Co alloys [Ref. 6].

Alloy	**Composition**	**Maximum permeability, μ_{max}**	**Coercivity, H_C (Oe)**	**Saturation Polarization, J_S (T)**
Permendur	$Fe_{50}Co_{50}$	5000	0.05	2.45
Supermendur	$Fe_{49}Co_{49}V_2$	60000	1	2.40

Fe-Co alloys: These alloys have higher saturation magnetization than pure Fe. They have both AC and DC applications, but high cost of Co has limited their applications only for

some special purposes. Selected magnetic properties of some Fe-Co alloys are listed in Table 1.3.

Soft Ferrites: At high frequencies, metallic SMM simply cannot be used due to the eddy current losses. Therefore, soft ferrites, which are ceramic insulators, become the most desirable material. These materials are ferrimagnetic with the general chemical formula $MO.Fe_2O_3$, where M is a transition metal. Mn-Zn ferrite, commercially known as ferroxcube, can be used at frequencies up to 10 MHz, for example in telephone signal transmitters / receivers and in switch mode power supplies [6].

1.2.2. Amorphous and nanocrystalline soft magnetic alloys

Remarkable progress in SMM took place in 1970s and 1980s with the advent of rapid solidification technique (RST) which provided a route to produce magnetic materials with new compositions and microstructure. Amorphous materials (also called metallic glasses) produced by RST are attractive candidates to replace the conventional spectrum of SMM in both DC and AC applications. Selected magnetic properties of some amorphous materials prepared by RST are listed in Table 1.4.

Since the discovery of amorphous SMA in 1970s, crystallization of the amorphous precursors was known to yield coarse grain microstructure with crystallite size of about 0.1-1μm with deterioration of the soft magnetic properties. However, a historical milestone in magnetic materials was achieved by Yoshizawa *et al.* [4] in 1988, who found that crystallization of Fe(Si,B) glasses with the combined addition of small amounts of Cu and Nb yields an ultrafine grain structure of bcc Fe(Si) with crystalline size ~10-15 nm embedded in a minority amorphous matrix. These nanocrystalline alloys

were found to exhibit coercivity ~10^{-3} Oe previously obtained only in case of permalloys and Co-based amorphous alloys. The significance of the these nanocrystalline alloys is that ultra low coercvity could be obtained in Fe-Si based alloys with high saturation polarization of 1.2 T or even more with the potential of a huge impact in all soft magnetic applications. Typical structural and magnetic parameters of some nanocrystalline alloys are listed in Table 1.5.

Table 1.4: Selected magnetic properties of some amorphous alloys prepared by RST [Ref. 9].

Alloy composition	**Coercivity, H_C (Oe)**	**Saturation polarization, J_S (T)**
$Co_{68}Fe_4(MoSiB)_{28}$	0.004	0.55
$Co_{72}(FeMn)_5(MoSiB)_{23}$	0.006	0.8
$Fe_{76}(SiB)_{24}$	0.04	1.45

Table 1.5: Typical structural and magnetic parameters of some nanocrystalline alloys.

Alloy composition	**Crystallite size, D (nm)**	**Coercivity, H_C (Oe)**	**Saturation Polarization, J_S (T)**	**Reference**
$Fe_{73.5}Cu_1Nb_3Si_{13.5}B_9$	13	0.006	1.24	[4]
$Fe_{73.5}Cu_1Nb_3Si_{15.5}B_7$	14	0.005	1.23	[9]
$Fe_{84}Nb_7B_9$	9	0.1	1.49	[10]
$Fe_{86}Cu_1Zr_7B_6$	10	0.04	1.52	[10]
$Fe_{91}Zr_7B_2$	17	0.07	1.63	[10]

1.3. Preparative methods of nanocrystalline materials

Nanocrystalline materials are usually prepared by two methods *viz*. crystallization of melt-spun amorphous precursor and mechanical alloying. A brief description of these two processing routes is given below.

1.3.1. Crystallization of melt-spun amorphous precursor

Melt spinning is a widely used technique for the preparation of amorphous metallic alloys. Nanocrystalline microstructure is obtained by proper heat treatment of the melt-spun amorphous precursor. Melt spinning essentially involves the ejection of a molten alloy through a crucible orifice onto a metallic wheel surface rotating at a high speed. A copper wheel is usually used due to its high heat conductivity. This technique provides quenching rates of the order of 10^5-10^7 K s^{-1}, sufficient to freeze the molten metallic alloy into the glass phase and thereby avoiding nucleation and crystal growth. The alloys are produced as thin (~30 μm) and wide (≥ 20 mm) ribbons which are typically many meters long. Only compositions that are close to the deep eutectics allow the glass phase to form at such high quenching rates. In addition to choosing compositions near deep eutectics, the crucible-orifice size, wheel speed and the pressure of ejection gas are the other entities which play important roles in determining the morphology of the resulting ribbons. Therefore, these parameters are needed to be optimized to obtain an amorphous phase by melt-spinning technique. Further, small amounts of elements like B, Si, P, C, *etc*. are usually used to stabilize the amorphous phase. Crystallization of the amorphous phase is usually carried out in vacuum or inert gas atmosphere. Crystallization of conventional amorphous alloys yields coarse grained microstructure with crystallite sizes of the order of 0.1-1 μm. Only certain alloy compositions of amorphous melt-spun

ribbons yield nanocrystalline microstructure. The optimum alloy composition which was first reported to lead nanocrystalline microstructure is $Fe_{73.5}Cu_1Nb_3Si_{13.5}B_9$ [4]. The combined addition of Cu and Nb is essentially responsible for the formation of the particular nanocrystalline structure. Subsequently, preparation of nanocrystalline alloys of various other compositions like $Fe_{84}Nb_7B_9$, $Fe_{86}Cu_1Zr_7B_6$, $Fe_{91}Zr_7B_2$ *etc.* [10], through this procedure have been reported.

1.3.2. Mechanical alloying

Mechanical alloying (MA) is a powder processing route for the production of homogeneous materials starting from mixtures of elemental metal powders. MA was developed in the 1970s as a technique for the production of oxide dispersion-strengthened alloys [11]. Since then, MA has evolved as a technique for the preparation of various equilibrium and non-equilibrium materials [7]. Synthesis of non-equilibrium phases like nanocrystalline and amorphous alloys by MA has gained a lot of research interest in recent years. The advantage of MA in the production of nanocrytalline materials lies in its ability to produce materials in powder form in large quantities by using simple equipment. The powders can be consolidated in any desired shape and dimension, and sintered, which is important from practical application point of view. Further, MA has been reported to be capable of preparing various alloys which are not possible by any other methods [7]. Thomson and Politis [12] in 1987 reported for the first time the formation of nanostructured materials by MA. Koch *et al.* [13] have summarized the literature on nanocrystalline materials prepared by MA route.

MA essentially involves milling of a blend of elemental powders with a particular composition along with the grinding media (generally hardened steel balls) in a mill for a definite time period until the formation of the alloy with the desired morphology. The important components of MA process are the raw material, the mill and the process variables. The process variables like ball to powder weight ratio, rotating speed of the vials (which contains the powders and the balls), volume of the vial used *etc.* play important roles in the MA process. Various types of mills like planetary ball mill, SPEX shaker mill, attrition mill *etc.* are usually used for MA process [7]. The MA technique produces nanostructured materials by the structural disintegration of coarser grained structure as a result of severe plastic deformation. The decrease of crystallite size from coarser grain to nanocrystalline structure during MA can be explained by the mechanism proposed by Fecht [14]. At the initial stage, the lattice microstrain increases sharply, resulting from a rapid increase in dislocation density caused by the plastic deformation. When a critical strain level is locally reached, the dislocations annihilate and rearrange into low-angle grain boundaries, separating the original crystallites into subcrystallites. On continued milling the subcrystallite structure extends throughout the sample resulting in nanocrystallites.

1.4. Soft magnetism in nanocrystalline ribbons

Brief discussions on some fundamentals of ferromagnetism and the origin of soft magnetism in nanocrystalline ribbons have been presented below.

1.4.1. Itinerant ferromagnetism

In transition metals Fe, Co and Ni, magnetism arises from the 3*d* levels which are partly filled according to Hund's rule [6] and thereby forms a net magnetic moment. In the case of metals, the atomic orbitals will overlap and form bands. For these 3*d* metals, the high lying 3*d* electrons will become delocalize and hence itinerant. The origin of ferromagnetism in 3*d* metals Fe, Co and Ni can be simply explained by the band theory of ferromagnetism (BTF) first proposed by Stoner [15] and later independently by Slater [16]. BTF is a simple extension of band theory of paramagnetism by the introduction of exchange coupling between the electrons. The Stoner criterion of ferromagnetism is briefly reviewed below.

Let us consider that the paramagnetic density of states (DOS) is known and it does not depend on the band filling. Thus, the energy of electrons of the band is

$$E_B = \int_0^{E_\uparrow} E D_S(E) dE + \int_0^{E_\downarrow} E D_S(E) dE \tag{1.1}$$

where $E_\uparrow$ and $E_\downarrow$ are the Fermi energies of the spin up and spin down bands, respectively. $D_S(E)$ is the paramagnetic DOS per spin. The DOS can be related to the number of electrons in the *d* band, *N*, and spin polarization, *s*, through the relation

$$\int_0^{E_\uparrow} D_S(E) dE - \int_0^{E_\downarrow} D_S(E) dE = sN \tag{1.2}$$

By assuming a small spin polarization, replacing $D_S(E)$ by $D_S(F)$, and subtracting the zero point energy term, the electron energy can be simplified as

$$\Delta E_B = \frac{N^2}{4 D_S(E_F)} s^2 \tag{1.3}$$

The exchange interaction term can be expressed in terms of the energy term as proposed by Stoner [17] as

$$E_{ex} = -\frac{I}{4}(N_{\uparrow} - N_{\downarrow})^2 = -\frac{I}{4}s^2N^2 \tag{1.4}$$

where I is the Stoner exchange parameter. The above equation contains a contribution from the Coulomb repulsion that arises from the fact that two electrons with the same spin cannot occupy the same local orbital (*cf.* Pauli's exclusion principle for atoms). In addition it contains the magnetic exchange between the electrons. Addition of equations (1.3) and (1.4) gives

$$\Delta E_B = \frac{N^2}{4}\left(\frac{1}{D_S(E_F)} - I\right)s^2 \tag{1.5}$$

To obtain a spontaneous spin polarization, the factor inside the parenthesis has to be negative, that is

$$D_S(E_F) \geq \frac{1}{I} \tag{1.6}$$

This is known as Stoner criterion of ferromagnetism which is satisfied only by the elements Fe, Co and Ni [18,19].

The reason for magnetism in the metals at the end of the 3*d* series is mainly the large DOS at the Fermi level. The reasons for the large DOS for the late 3*d* metals are several. First of all, the 3*d* band must accommodate 10 electrons, and secondly the *d* band is contracted with increasing atomic number due to the increasing nuclear charge. In fact, it would be intuitive to believe that elements such as Rh and Pd should also be ferromagnetic. But, the 4*d* electrons are further away from the core they also extend further out. Consequently, the bands broaden and have a lower DOS at the Fermi level. Hence, the only pure transition metals that exhibit ferromagnetism are the late 3*d* metals.

1.4.2. Magnetic moment

Magnetic moment in an atom arises due to the motion and interaction between the electrons. Orbital magnetic moment and spin magnetic moment mainly contribute to the total magnetic moment of the atom. Nuclear magnetic moment contribution is negligible by comparison. The maximum magnetic moment, μ, of a single atom in a particular direction is given by [20]

$$\mu = gJ\mu_B \tag{1.7}$$

where g is the Lande factor (ratio of the magnetic moment to the angular momentum), μ_B is the Bohr magnetron ($1\ \mu_B = 9.274 \times 10^{-24}$ JT^{-1}) and J is the total angular momentum of the atom. J is defined as $J = L \pm S$, where L is orbital angular momentum and S is the spin angular momentum. The sign (±) is determined by Hund's rule.

The magnetic moments of the transition elements Fe, Co and Ni originate due to the 3*d* band electrons. To explain the measured magnetic moments (presented in Table 1.6) in a simple way, the concept of strong and weak ferromagnetism has been introduced. Co and Ni are the strong ferromagnets, where the spin up band is completely filled with 5 electrons. Fe, on the other hand, is an example weak ferromagnet in which the spin up band is partially filled. Since, a strong ferromagnet has the spin up band completely filled, its magnetic moment can be estimated from the number of valence electrons in the atom [6]. As the spin up band is completely filled and contains 5 electrons, and the atom has n valence in total (the number of 3*d* and 4*s* electrons), the atomic magnetic moment can be calculated as

$$\mu = 5 - (n - x - 5) = (10 - n + x)\mu_B \tag{1.8}$$

where x is the number of 4s electrons per atom. In isolated atoms of Fe, Co and Ni, the number of 4s electrons is 2 but in a metallic crystal, the 4s electrons will spill into 3d band. In order to reproduce the measured magnetic moments, the 4s band must contain only about 0.65 electrons [19]. This will lead to the relation

$$\mu = (10.65 - n)\mu_B \tag{1.9}$$

which for Fe with n = 8, Co with n = 9, and Ni with n = 10 gives the magnetic moments of 2.65μ_B, 1.65μ_B and 0.65μ_B, respectively. These estimates agree well with the measured values presented in Table 1.6.

Table 1.6: No of valence electrons, n, atomic magnetic moment, μ, for the ferromagnetic 3d metals [Ref. 21].

Element	***n***	**μ (μ_B)**
Fe	8	2.23
Co	9	1.73
Ni	10	0.62

1.4.3. Exchange interaction

The orientation of adjacent local magnetic moments is determined by the exchange interaction between them. The exchange interaction between the neighboring atoms can be expressed in terms of a Heisenberg's Hamiltonian [20]

$$\hat{H}^{spin} = -\sum_{ij} J_{ij} S_i S_j \tag{1.10}$$

where J_{ij} is the exchange constant between the i^{th} and j^{th} spins. J_{ij} is positive for a ferromagnetic interaction (spins coupled parallel) and negative for antiferromagnetic interaction (spins coupled antiparallel).

In metals like Fe, Co and Ni the exchange interaction between the atoms can be mediated by the conduction electrons. A localized magnetic moment spin polarizes the conduction electrons and this polarization in turn couples to a neighbouring localized magnetic moment at a distance *r* away. It is known as RKKY (named after the initials of surnames of the discoverers Ruderman, Kittel, Kasuya and Yoshida) interaction or also as itinerant exchange [20].

1.4.4. Magnetocrystalline anisotropy

In ferromagnetic materials, there exist certain preferred crystallographic directions (easy axes) of magnetization along which less field is necessary to magnetize the material than along other axes called hard axes. The origin of this feature is attributed to the spin-orbit coupling which can be simply visualized as the interactions between crystal lattice, orbit, and spin of the electron. The orbits are strongly coupled to the lattice and even large fields cannot change them. The microscopic explanation is that neighbouring atoms in a crystal will exert an electric field, known as the crystal field, on the orbiting electrons. This will force the orbits to align themselves with the crystal fields. Further, there is also a coupling between the spin and the orbital motion of each electron called spin-orbit coupling. If an external magnetic field is applied it tries to reorient the spin of the electron, the orbit of that electron also tends to get reoriented. As the orbit is strongly coupled to the lattice, it tries to resist the attempt to rotate the spin axis. The energy

required to spin away from the easy axis is the just the energy required to overcome the spin-orbit coupling which is known as magnetocrystalline anisotropy energy (MAE).

The angular dependence of magnetocrystalline anisotropy relates to the symmetry of the crystal itself. Thus, magnetocrystalline anisotropy can be expanded as a power series of direction cosines which satisfies the crystal symmetry. For a cubic crystal, the lowest order direction cosine is the fourth order and the anisotropy energy in spherical polar coordinate can expressed as [20]

$$E_a = K_1\left(\frac{1}{4}\sin^2\theta\sin^2 2\phi + \cos^2\theta\right)\sin^2\theta + \frac{K_2}{16}\sin^2 2\phi\sin^2 2\theta\sin^2\theta \qquad (1.11)$$

In cubic anisotropy, a one-constant anisotropy equation can be used as a first approximation [6], leading to the relation

$$E_a = K_1\left(\cos^2\theta_1\cos^2\theta_2 + \cos^2\theta_2\cos^2\theta_3 + \cos^2\theta_3\cos^2\theta_1\right) \qquad (1.12)$$

where θ_1, θ_2, θ_3 are the angles which the magnetization makes relative to the three crystal axes.

Table 1.7: Magnetocrystalline anisotropy constants of Fe, Co and Ni [Ref. 6].

Material	K_1 (10^5 Jm^{-3})	K_{u1} (10^5 Jm^{-3})	K_2 (10^5 Jm^{-3})	K_{u2} (10^5 Jm^{-3})
Fe (cubic)	0.480	-	0.050	-
Ni (cubic)	-0.045	-	0.023	-
Co (hexagonal)	-	4.1	-	1.0

In case of hexagonal crystals, the anisotropy constant can be expressed by the one-constant approximation as [6]

$$E_a = K_{u1} \sin^2 \phi \tag{1.13}$$

where, ϕ is the angle of magnetization with respect to the unique axis, which for $K > 0$ it is the easy axis, where as, for $K < 0$ it is the hard axis. The anisotropy constants of Fe, Co and Ni are presented in Table 1.7.

1.4.5. Magnetoelastic anisotropy

When a ferromagnetic material is exposed to a magnetic field, its dimensions changes and thereby it experiences a strain. This effect is known as magnetostriction. The inverse effect *i.e.* the change of magnetization with stress also occurs and produces a unique easy axis of magnetization giving rise to magnetoelastic anisotropy. The anisotropy energy associated to the magnetoelastic effect can be expressed as [21]

$$E_{me} = -K_{me} \cos^2 \phi \tag{1.14}$$

where ϕ is the angle between the magnetization and the plane of isotropic anisotropy and

$$K_{me} = -\frac{3}{2}\lambda\sigma = -\frac{3}{2}\lambda E\varepsilon \tag{1.15}$$

here λ is the magnetostriction coefficient and σ is the stress which relates to the strain, ε, through the elastic modulus E.

1.4.6. Magnetic domains

A ferromagnetic material consists of magnetic domains. In a domain, the magnetic moments are aligned parallel within volumes containing large number of atoms. But

these domains are still on the microscopic scale in most cases. In the demagnetized state, domains are randomly oriented but get aligned in a magnetized material. In a material with sufficiently large crystallites, the number and size of domains are governed by a balance between the domain wall energy produced by the splitting into domains and lowering the magnetostatic energy. The change of the spontaneous magnetization from a domain to its neighbour occurs at the domain wall. The spins in the wall points in the non-easy directions. Therefore, the anisotropy energy is higher within the wall than in its adjacent domains. The exchange energy tries to make the wall as wide as possible. In order to make the angle between the adjacent spins as small as possible, the anisotropy energy tries to make the wall thin *i.e.* reducing the number of spins pointing in non-easy directions. This competition leads to certain finite domain wall width by minimization of the total energy. The domain wall width δ is related to the exchange length, $L_{ex} = \sqrt{\frac{A}{K}}$ (where A is the exchange stiffness constant and K is the magnetocrystaline anisotropy constant of the material) by the relation [20]

$$\delta = \pi L_{ex} \tag{1.16}$$

1.4.7. Magnetization processes

In demagnetized ferromagnetic materials, the domains are randomly oriented with no spontaneous magnetization. When a magnetic field is applied, the domains start aligning along the field direction. At low fields, the first domain process that occurs is the growth of magnetic domains aligned favourably with respect to the field according to the minimization of field energy, by domain wall motion and a consequent reduction of domains aligned in a direction opposing the field [6]. At moderate applied fields, a

second process becomes significant in which the magnetic moments within a unfavourably aligned domain overcome the anisotropy energy and suddenly rotate from their original direction of magnetization into the crystallographically easy axes nearest to the field direction. Finally, at higher applied fields magnetic moments along the preferred magnetic crystallographic easy axes gradually rotates into the field direction, completing the magnetization processes (*cf.* path OA in Figure 1.1.).

The domain mechanisms involved in magnetization processes, *viz*. wall motion and domain rotation can be manifested as either reversible or irreversible processes. Domain wall motion occurring by bowing of domain walls is usually reversible until the wall is sufficiently deformed such that the expansion continues without further increase of field. The domain wall motion is usually irreversible unless the material is sufficiently pure so that the domain wall can exist in a region of the material that is free of defects. Through the magnetoelastic coupling, dislocations pin the domain walls. So, with higher dislocation density within a ferromagnet, higher impedance is offered to the domain wall motion. Rotation of magnetic moments within domains for the low applied field is a reversible process. At intermediate to high fields, rotation of moments within the domains from their original easy axis to the easy axis closest to the field direction is an irreversible process. This occurs when the field energy overcomes the anisotropy energy [6]. At higher fields, the rotation of the magnetic moments to the field direction is a reversible process.

Because of the irreversible magnetic processes occurring during magnetization certain magnetic field in the reverse direction is necessary to make the magnetization zero from the saturation magnetization which known as the coercivity of the material.

The value of the coercivity mainly depends on the magnetocrytalline anisotropy and the microstructure of the material. During the demagnetization of the material two mechanisms namely nucleation of reverse domains and domain wall pinning can occur in the material resulting in certain value of coercivity. These two mechanisms are not mutually exclusive, since both occur in technical magnets. In the case of nucleation of reverse domains, coercivity corresponds to the inverse field required to nucleate a reverse domain. On the other hand, in case of domain wall pinning mechanism, the domain wall is pinned by crystallographic defects or non magnetic impurities (pinning centers). The magnetization reversal can only be realized by overcoming the maximum pinning force.

1.4.8. Origin of soft magnetism in nanocrystalline ribbons

The coercivity of a material is strongly dependent on its microstructure. The crystallite size and defects like grain boundaries, non-magnetic inclusions and internal stresses influence the coercivty. According to Mager [22], the coercivity determined by grain boundaries is a linear function of the reciprocal of the diameter of the crystallite, D, according to the relation

$$H_C \approx 3\frac{\gamma_W}{J_S}\frac{1}{D} \tag{1.17}$$

where, γ_W is the domain wall energy and J_S is the saturation polarization. The wall energy can be expressed as [20]

$$\gamma_W = \sqrt{kT_C K / a} \tag{1.18}$$

where k is the Boltzmann constant, T_C is the Curie temperature of the material, K is the magnetocrystalline anisotropy and a is the lattice parameter. From equations (1.17) and (1.18), one can write

$$H_C \approx 3\frac{\sqrt{kT_C K/a}}{J_S}\frac{1}{D} \tag{1.19}$$

However, the D^{-1} dependence on coercivity is valid only when the crystallite size is higher than the ferromagnetic exchange length (FEL) where the magnetization is governed mainly by the magnetocrystalline anisotropy of the crystallites [23]. FEL is a basic parameter in domain theory which characterizes a minimum range over which the magnetization can vary appreciably and can be expressed as [20]

$$L_{ex} = \sqrt{\frac{A}{K}} \tag{1.20}$$

where A is the exchange stiffness constant and K is the magnetocrystalline anisotropy constant. FEL determines the size barrier between multi-domain and single-domain structures.

For crystallite size less than the ferromagnetic exchange length, magnetization process is governed by the interplay of magnetocrystalline anisotropy of the crystallites and the ferromagnetic exchange energy. The theoretical model by Herzer known as random anisotropy model (RAM) [23] which explains the origin of ultra low coercivity in nanocrytalline ribbons is briefly discussed below. The RAM was originally proposed by Alben *et al.* [24] for amorphous ferromagnets. Herzer applied it to explain the ultra low coercivity in nanocrystalline ribbons.

The basic idea of RAM is depicted in Figure 1.2. It shows an assembly of randomly oriented ferromagnetically coupled crystallites of size D with magnetocrystalline anisotropy constant K.

The effective magnetocrystalline anisotropy affecting the magnetization process results from averaging over the $N = (L_{ex} / D)^3$ crystallites within the volume $V = L_{ex}^{\ 3}$ of the exchange length. For a finite number, there will always be some easiest direction determined by the statistical fluctuations. As a consequence, the resulting anisotropy $\langle K \rangle$ is determined by the mean fluctuating amplitude of anisotropy energy of N crystallites, which is given by

$$\langle K \rangle \approx \frac{K}{N} = K\left(\frac{D}{L_{ex}}\right)^{3/2} \tag{1.21}$$

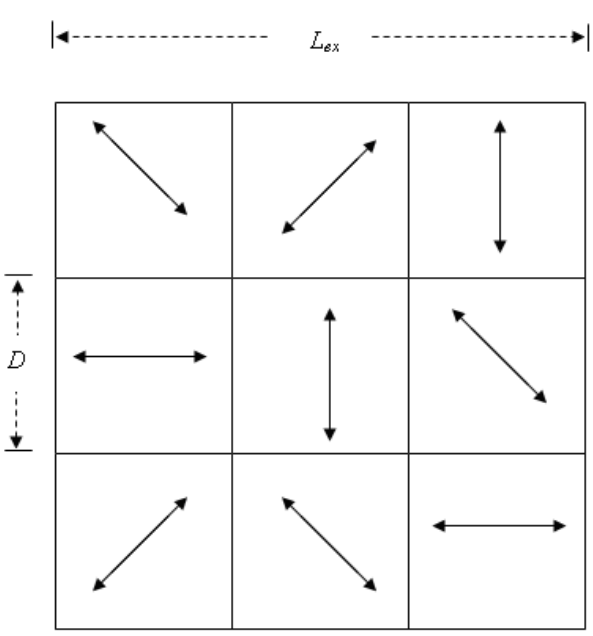

Figure1.2: Schematic representation of RAM. The solid arrows indicate the randomly fluctuating magnetocrystalline anisotropy.

In turn, the exchange constant is now related self consistently to the average anisotropy by substituting $\langle K \rangle$ for K in equation (1.21), *i.e.*

$$L_{ex} = \sqrt{\frac{A}{\langle K \rangle}} \tag{1.22}$$

As magnetocrystalline anisotropy is suppressed by exchange interaction, the scale on which exchange interaction dominate expands at the same time, and thus local anisotropies are averaged out more effectively. The combination of equations (1.21) and (1.22) results in

$$\langle K \rangle \approx \frac{K^4}{A^3} D^6 \tag{1.23}$$

This relation is valid as long as the crystallite size is less than the ferromagnetic exchange length L_{ex}. The coercivity (H_C) can be related to $\langle K \rangle$ using the relation between H_C and magnetocrystalline anisotropy for coherent rotation of spins [25]

$$H_C = p_C \frac{K}{J_S} \approx p_C \frac{KD^6}{J_S A^3} \tag{1.24}$$

where p_C is a dimentionless parameter, J_S is the saturation polarization and A is stiffness constant. Accordingly, coercivity varies as D^6 when D is less than the ferromagnetic exchange length. This is known as D^6 law for nanocrystalline materials and it explains the origin of soft magnetism in nanocrystalline ribbons.

1.5. Mechanically alloyed soft magnetic materials

In recent years, mechanical alloying (MA) has drawn a lot of research interest because of its versatility to prepare nanocrystalline soft magnetic alloys in a wide range of compositions in powder form with relatively inexpensive equipments. Melt spun

nanocrystalline ribbons are thin and usually brittle, which restricts their applications mainly to toroidal cores. These limitations can be overcome by the preparation of soft magnetic alloys by MA. Table 1.8 summarizes the coercivity of mechanically alloyed nanocrystaline soft magnetic powders reported in the literature. The reports on mechanically alloyed Fe-Si based alloys have been highlighted due to their relevance to this thesis work, while reports on some other alloy systems have also been included.

The crystallite size of the nanocrystalline powders mentioned in Table 1.8 is mostly in the range 10-20 nm. However, the value of coercivity in the mechanically alloyed nanocrystalline powders has been reported to be higher as compared to nanocrystalline melt-spun ribbons (H_C ~10^{-3} Oe). The higher values of coercivity have been mainly attributed to the high strain and dislocations induced during the milling process. In most of these reports, saturation magnetization has been reported to be slightly less than that of pure Fe and independent of microstructure.

The reports on mechanically alloyed Fe-Si alloys [26-29] show the formation of non-equilibrium solid solution α-Fe(Si) during the milling process. Ding *et al.* [27] reported that annealing preserved the disordered α-Fe(Si) phase of the as-milled $Fe_{75}Si_{25}$ powders. However, crystallite size increased with a significant decrease of coercivity. The decrease of coercivity has been attributed to the relaxation of strain during annealing.

In the literature, there are some reports on systematic studies pertaining only to structure of as-milled and annealed Fe-Si powders [40, 41]. Perez *et al.* [40] reported on the synthesis of nanocrystalline $Fe_{80}B_{13}Si_7$ powders. The lattice parameter estimation from X-ray peaks have indicated of about 75% dissolution of Fe and only 35% dissolution of B after 128 hours of milling. Zuo *et al.* [41] reported on the effect of

Table 1.8: Coercivity of mechanically alloyed nanocrystalline powders.

Material	**Processing**		**Coercivity (Oe)**	**Ref.**
	MA (Milling time in hours)	**Heat Treatment** (time; Temperature)		
$Fe_{100-x}Si_x$ (x = 6.5 – 25)	40	—	120 - 140	[26]
$Fe_{100-x}Si_x$ (x = 0 – 40)	40	20 min.; 473 – 973 K	2.4 - 7.4	[27]
$Fe_{100-x}Si_x$ (x = 6.5 –20); $Fe_{83.5}Si_{13.5}Nb_3$	40	20 min.; 643 - 773 K	53 - 65	[28]
$Fe_{100-x}M_x$ (M = Al, Si, Cu; x = 0 – 50)	60	—	3.8 - 50	[29]
$Fe_{90}Ni_{10}$; $Fe_{80}Ni_{20}$	0 –100	—	50 - 200	[30]
$Fe_{100-x}Co_x$ (x = 0 – 80)	100	30 min.; 973 – 1273 K	6.3 - 17	[31]
Fe; $Fe_{50}Co_{50}$	0 – 40	—	50 - 72	[32]
Co; $Co_{90}Ni_{10}$	0 – 100	—	40 - 160	[33]
$Fe_{73.5}Cu_1Nb_3Si_{13.5}B_9$; $Fe_{82}Si_{18}$	0 – 60	—	85 - 125	[34]
$Fe_{80}Cu_{20}$; $Fe_{92}Al_2Si_6$	30	60 min.; 373 – 673 K	10 - 100	[35]
$Fe_{50}(SiC)_{50}$	0 – 40	—	154 - 320	[36]
$Fe_{75}Si_{20}Ni_5$	35 – 100	—	30 - 80	[37]
$Fe_{73.5}Cu_1Nb_3Si_{13.5}B_9$	0 – 3500	—	80 - 320	[38]
$Fe_{75}Nb_{10}Si_5B_{10}$	5 – 200	600K, 800 K	50 - 95	[39]

annealing on the structure of $Fe_{90}Si_{10}$, $Fe_{75}Si_{25}$ and $Fe_{75}Si_{15}Al_{10}$ powders milled for 100 hours and annealed in the temperature range 573 K – 973 K each for 30 minutes. For $Fe_{75}Si_{25}$ and $Fe_{75}Si_{15}Al_{10}$ powders, annealing resulted in a transformation of the disordered phase of as-milled powders to ordered DO_3 phase accompanied with growth of crystallite size and relaxation of strain. Although, growth of crystallites and stress relaxation was observed in $Fe_{90}Si_{10}$ powders as well, there was no change of the disordered phase of as-milled powders. The transformation of phase of as-milled $Fe_{75}Si_{25}$ powders after annealing differs from the earlier observation by Ding *et al.* [27]. There are only a few reports on the Curie temperature of mechanically alloyed Fe-Si alloys. Kohomoto *et al.* reported that there is slight decrease of Curie temperature in $Fe_{93.6}Si_{6.5}$ powders after mechanical alloying [42].

The above mentioned reports are on nanocrystalline alloys prepared directly by MA. However, MA is capable of preparing amorphous alloys. Appropriate heat treatment of the amorphous alloys may result in nanostructured phases. However, there are only a few reports on the preparation of nanocrystalline phase from mechanically alloyed amorphous precursors [43, 44]. Ji *et al.* [43] observed that annealing of mechanically alloyed amorphous powders of $(Fe_{0.5}Co_{0.5})_{60}Cu_2V_8B_{30}$ results in precipitation of nanocrystalline α-($\alpha^{/}$)FeCo phase in the amorphous matrix. Pizzaro *et al.* [44] reported that segregation of α-Fe with crystallite size of 30 nm occurs after annealing amorphous $Fe_{75}Zr_{25}$ powder prepared by MA. However, there are no systematic studies on the microstructure and coercivity of these powders and thereby this area of research has been relatively unexplored.

1.6. Motivation and preview of the thesis work

Soft magnetism in nanocrystalline ribbons has brought a revolutionary change in the understanding of magnetism and in the design of soft magnetic alloys. MA being a completely different route of processing of nanocrystalline alloys provides huge scope for exploring the properties of nanocrystalline alloys. Further, MA has certain advantages over melt-spun ribbons as pointed out earlier. Considering these aspects, MA has been chosen as the synthesis route for the preparation of the alloys in the present thesis work.

Fe-Si based alloys have been taken up for study in the present thesis work mainly because of their importance as conventional soft magnetic alloys as well as their excellent soft magnetic properties in melt-spun nanocrystalline form. In spite of considerable number of studies on mechanically alloyed nanocrystalline Fe-Si alloys existing in the literature, the lack of proper understanding and the urge to improve the soft magnetic properties in mechanically alloyed powders continue to instill interest in this topic in recent years.

The present thesis work attempts to gather a comprehensive understanding of the correlation between microstructure and magnetic properties in mechanically alloyed powders. For this purpose, Fe-Si powders with composition of $Fe_{75}Si_{25}$ (at%) have been chosen as the parent material. $Fe_{75}Si_{25}$ (Fe_3Si) was chosen as the base material due to the finding that MA of Fe and Si powders in the ratio 3:1 yields a solid solution of α-Fe(Si) [41]. Further, Fe_3Si is a composition of the ordered DO_3 phase and the influence of structural ordering on magnetic properties has not been well explored even in coarser grained alloys. A systematic study on the effects of additive elements on structure and soft magnetic properties of the alloys is also lacking in literature. Based on these

considerations, $Fe_{75}Si_{25}$, $Fe_{75}Si_{20}M_5$ (M = Al, B, Cr) and $Fe_{75}Si_{15}M_{10}$ (M = Al, B, Cr) have been taken up for investigation in the present thesis work. It is worth pointing out that Al is known to reduce the magnetostriction and hence coercivity [45]. Moreover, B is known to increase the grain boundaries in melt-spun nanocrystalline ribbons, while there are some reports on improvement of soft magnetic properties in Fe-Si alloys after the addition of Cr [46].

A systematic study on the evolution of nanocrystalline phase and the relation between the structure and magnetic properties of Fe-Si-M powders has been carried out. Effect of annealing on structure and soft magnetic properties of milled powders has also been explored. Considering the relatively unexplored area of nanostructured alloys prepared from mechanically alloyed amorphous precursor, amorphous $Fe_{75}Si_{15}Cr_{10}$ powder was obtained by MA. These powders and the nanocrystalline powders obtained from them have been investigated.

Chapter 2

Experimental techniques

In the course of the present investigations, several experimental techniques have been used for processing and characterizing the alloy powders. The different experimental techniques employed are briefly explained in this chapter.

2.1. Material processing

Material processing carried out in this thesis work involve two processes, *viz.* high energy ball milling of the elemental powders and heat treatment of as-milled powders under very low ambient pressures. Both the techniques and the corresponding equipment are briefly discussed below.

2.1.1. High energy ball milling

Mechanical alloying (MA) of elemental powders has been carried out by high energy ball milling in a planetary ball mill (Insmart, India). A planetary ball mill comprises of a horizontal support disc on which vials are mounted. A photograph of the ball mill used in the studies is shown in Figure 2.1 (a). The disc rotates in a direction opposite to that of

the vial, thereby simulating a planetary motion. This planetary motion results in large centrifugal force acting on the balls kept inside the vial [*cf.* Figure 2.1(b)]. This causes the balls to collide with themselves and the wall of the vial with a high impact. When a mixture of elemental powders is placed in the vial along with the balls, the powders are subjected to repeated cold welding and fracture at the surfaces of the balls and the vial. As mentioned in the previous chapter, this process leads to disintegration of the powders leading to crystallite size refinement and ultimately atomic level mixing which results in alloy formation. As mentioned earlier, size refinement is a natural consequence of a MA process. The refinement and alloying processes are determined by the milling parameters such as powder to ball weight ratio, ball size, rotation speed, milling time, *etc*. Nature of the milling vial and balls also plays an important role in the process along with the milling media. Various liquids such a toluene are used as milling media.

(a) (b)

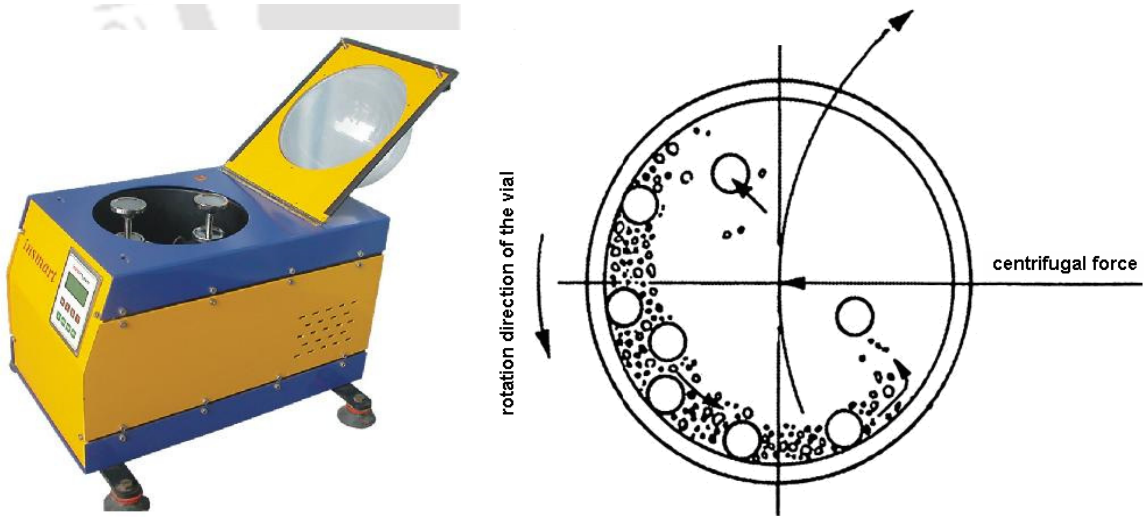

Figure 2.1: (a) Photograph of the planetary ball mill used, (b) Schematic diagram of the horizontal section of a vial depicting the movement of the balls generated inside the vial due to its planet like movement.

In the present work, dry milling of high purity elemental powders has been carried out in high purity Ar atmosphere. Hardened steel vial and hardened steel balls were used for milling all the compositions. MA is a low temperature process. Prolonged milling under dry conditions results in a temperature rise inside the vial which usually deteriorates the final product. Hence, the mill was programmed to halt for 30 minutes after every 30 minutes of continuous operation.

2.1.2. Heat treatment at elevated temperatures

For the purpose of heat treatment of the mechanically alloyed powders at elevated temperatures (annealing), a resistive tubular furnace (Okay, India) was used. The tubular furnace could be used up to a temperature of 1600 ˚C. The temperature of the constant temperature heat zone at the centre of the furnace extends to 150 mm, which could be controlled to ± 2 ˚C with a temperature controller.

Since, the as milled powders would oxidize if heated to high temperature under ambient conditions, they were sealed in evacuated fused silica ampoules prior to the heat treatment. For this, ~80 mm long ampoules with a constriction were fabricated from fused silica tubes of 8 mm internal diameter. As milled powders were transferred into the well cleaned and dried ampoules and connected to a pumping system. The pumping system (Vacuum Techniques, India) consisted of a diffusion pump capable of creating a low pressure of 10^{-4} Pa. After creating the low pressure, the constricted (neck) portion of the ampoule was flame sealed with a neutral oxygen-liquid petroleum gas flame and the sealed ampoule was detached from the tube. These ampoules were then loaded in the annealing furnace for heat treatment.

2.2. Structural characterizations

2.2.1. X-ray diffractometer (XRD)

Three different powder X-ray diffractometers *viz*. Seifert 3003 T/T, Bruker D8 and Rigaku RINT 2000 were used in the thesis work depending upon the availability. CuK_{α} X-ray radiation with wavelength 0.15406 nm was used in all the cases. The theta-theta ($\theta - \theta$) goniometer was used in the reflection (Bragg-Brentano) geometry (*cf.* Figure 2.3) [47]. The X-ray diffraction (XRD) technique allows identification of various crystalline phases present in the material and provides other structural information such as the size of the crystallites, strains present inside the crystallites, *etc*.

An ideal crystal has a periodic arrangement of atoms. Diffraction of X-rays occurs through constructive interference of X-rays scattered from atoms of a set of parallel planes in crystal lattice at a particular angular positions of the incident wave known as Bragg angles [47]. This condition for obtaining constructive interference is known as Bragg's law given by the relation [47]

$$2d_{hkl} \sin\theta_0 = n\lambda \qquad (2.1)$$

where d_{hkl} is the interplaner spacing, θ_0 is the glancing angle, λ is the wavelength of the X-ray and n is the order of diffraction. A series of these angles can be used to determine the Miller indices (*hkl*) values and the crystal structure can be identified from the systematic behaviour of these indices [47]. Figure 2.2 shows the diffraction of X-rays from crystal lattice planes illustrating Bragg's law.

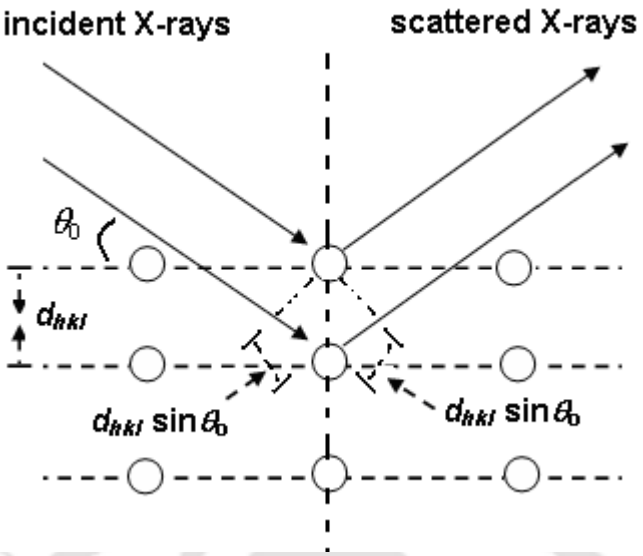

Figure 2.2: Diffraction of X-rays by a crystal.

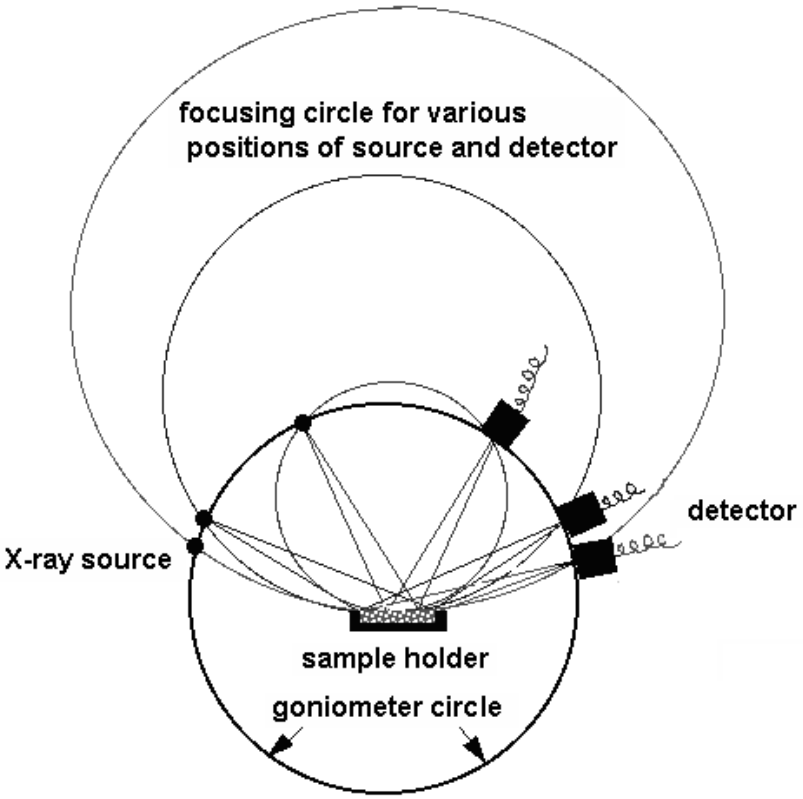

Figure 2.3: Bragg-Brentano geometry of a powder X-ray diffractometer.

The crystallite size and the strain present in the crystallites can be estimated from the width of the diffraction peaks. Reduction in the crystallite size results in less number of diffracting planes. This is analogous to the diffraction of light from a grating where the line width is proportional to the number of diffracting grooves in the grating. The broadening $\delta_{size}(2\theta)$ due to crystallite size can be quantified by Scherrer's formula [47]

$$\delta_{size}(2\theta) = \frac{0.9\lambda}{D\cos\theta_0} \tag{2.2}$$

where $\delta_{size}(2\theta)$ is broadening due to crystallite size, θ_0 is the peak position, λ is the wavelength of the X-ray and D is the size of the average crystallite of the material. Presence of strain also broadens the peak which can be quantified as [47]

$$\delta(2\theta_{strain}) = 4e\tan\theta \tag{2.3}$$

where e is the lattice strain. In a material in which both these broadening effects occur, the crystallite size and strain can be estimated using the Williamson-Hall method [48] for a set of Bragg peaks. The Williamson-Hall method is a linear representative of the total broadening effect expressed as

$$\delta(2\theta)\cos\theta_0 = \frac{0.9\lambda}{D_{WH}} + 4e\sin\theta_0 \tag{2.4}$$

where $\delta(2\theta)$ is the total broadening which is the full width half maxima of the peak after instrumental correction.

In case of elastically anisotropic materials, certain Bragg peaks are more affected by strain than other and modified Williamson-Hall method [49,50] can be used to analyze the diffraction peaks. The modified Williamson-Hall proposed by Ungar *et al.* [49,50] is expressed as

$$(\Delta K)^2 = \left(\frac{0.9\lambda}{D_{MWH}}\right)^2 + \left(\frac{\pi b^2 \rho}{2B}\right) K^2 C_{hkl} \qquad (2.5)$$

where $\Delta K = (2\cos\theta_B \Delta\theta_B)/\lambda$, $K = 2\sin\theta_B/\lambda$, C_{hkl} is the dislocation contrast factor for different Bragg peaks, b is modulus of the Burgers vector of dislocations, ρ is the average dislocation density and B is a constant.

2.2.2. Scanning electron microscope (SEM)

Scanning Electron Microscope (SEM, Leo 1430VP) with Energy Dispersive Spectroscopy (EDS) attachment (Oxford) has been used to study the morphology of the powders and to determine the chemical composition of phases present in the powders.

SEM is a powerful microscope that uses electrons rather than light to form an image of objects such as study of morphology of powders, fractured metal components, foreign particles and residues, polymers, electronic components, biological samples and countless others. The shorter wavelength of electrons permits image magnifications of up to 100,000×, as compared to about 2,000× for conventional light microscopy. A SEM also provides a greater depth of field than a light microscope, allowing complex, three-dimensional objects to remain sharp and in focus. This capability reveals details that cannot be resolved by light microscopy.

A schematic representation of a SEM has been shown in Figure 2.4. The electrons are accelerated in a potential difference typically of the order of 10-20 keV and focused on a spot volume of the specimen, resulting in the transfer of energy to the spot. These bombarding electrons, also referred to as primary electrons, dislodge electrons from the specimen itself. The dislodged electrons, also known as secondary electrons, are attracted

and collected by a positively biased grid or detector, and then translated into a signal. To produce the SEM image, the electron beam is swept across the area being inspected, producing many such signals. These signals are then amplified, analyzed, and translated into images of the topography being inspected. Finally, the image is shown on a CRT.

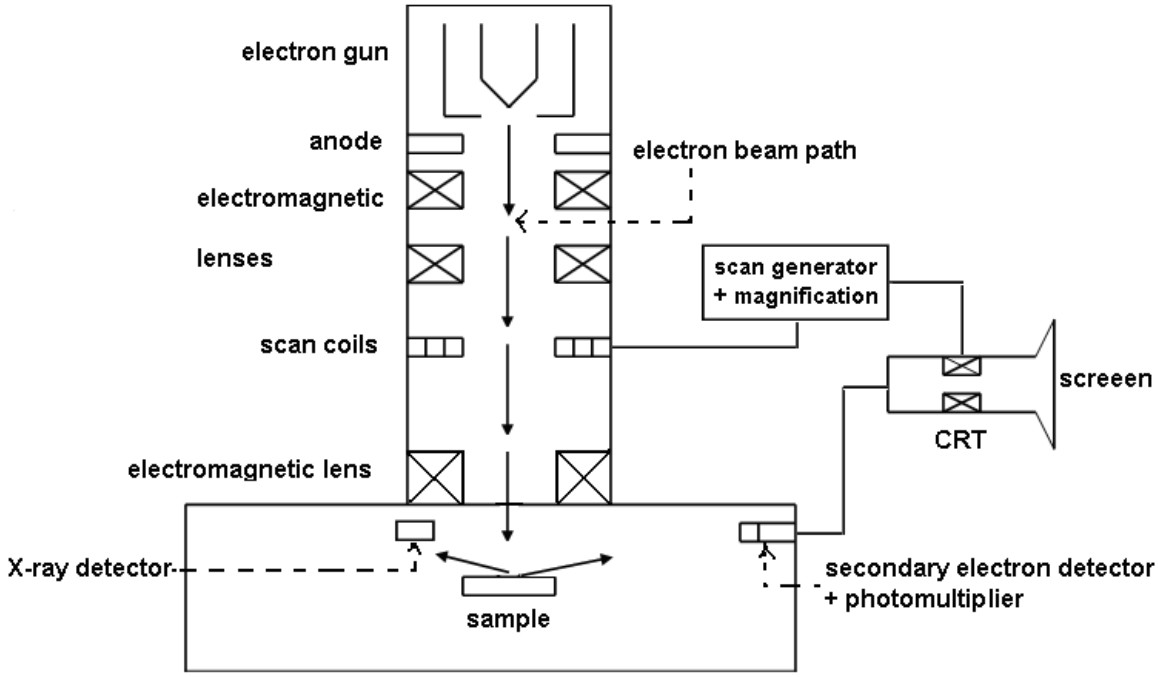

Figure 2.4: Schematic diagram of a SEM.

The energy of the primary electrons determines the quantity of secondary electrons collected during inspection. The emission of secondary electrons from the specimen increases as the energy of the primary electron beam increases, until a certain limit is reached. Beyond this limit, the collected secondary electrons diminish as the energy of the primary beam is increased, because the primary beam is already activating

electrons deep below the surface of the specimen. Electrons coming from such depths usually recombine before reaching the surface for emission.

The most common imaging mode relies on detection of this very lowest portion of the emitted energy distribution. Their very low energy means they originate from a sub-surface depth of no larger than several angstroms. The signal is captured by a detector consisting of a scintillator-photomultiplier combination, and the output serves to modulate the intensity of cathode ray tube (CRT), which is rastered (formation consisting of the set of horizontal lines composed of pixels that is used to form an image on a CRT is known as raster) in synchronism with the raster-scanned primary beam. Resolution specifications on research quality SEMs are ~ 50 Å.

Apart from secondary electrons, the primary electron beam results in the emission of backscattered (or reflected) electrons from the specimen. Backscattered electrons possess more energy than secondary electrons and have a definite direction. As such, they can not be collected by a secondary electron detector, unless the detector is directly in their path of travel. All emissions above 50 eV are considered to be backscattered electrons.

Backscattered electron imaging is useful in distinguishing one material from another, since the yield of the collected backscattered electrons increases monotonically with the specimen's atomic number Z (~$0.05Z^{1/2}$). Backscatter imaging can distinguish elements with atomic number differences of at least 3, *i.e*. materials with atomic number differences of at least 3 would appear with good contrast on the image.

A SEM may be equipped with an EDS (energy dispersive spectoroscopy) system to enable it to perform compositional analysis on specimens. EDS analysis is useful in

identifying materials and contaminants, as well as estimating their relative concentrations on the surface of the specimen. During EDS analysis, the specimen is bombarded with an electron beam inside the SEM. The bombarding electrons collide with the specimen atoms own electrons, knocking some of them off in the process. A position vacated by an ejected inner shell electron is eventually occupied by a higher-energy electron from an outer shell. To be able to do so, however, the transferring outer electron must give up some of its energy by emitting X-rays.

The amount of energy released by the transferring electron depends on which shell it is transferring from, as well as which shell it is transferring to. Furthermore, the atom of every element releases X-rays with unique amounts of energy during the transferring process. Thus, by measuring the amounts of energy present in the X-rays being released by a specimen during electron beam bombardment, the identity of the atom from which the X-ray was emitted can be established.

The output of an EDS analysis is an EDS spectrum. The EDS spectrum is just a plot of how frequently an X-ray is received for each energy level. An EDS spectrum normally displays peaks corresponding to the energy levels for which the most X-rays had been received. Each of these peaks is unique to an atom, and therefore corresponds to a single element. The higher a peak in a spectrum, the more concentrated the element is in the specimen.

In the present work, a thin layer of powder was spread on carbon coated tape and then gold coated to yield an electrically conducting surface for SEM observation.

2.2.3. Transmission Electron Microscope (TEM)

Transmission electron microscope (TEM, Jeol 2100) has been used to study the microstructure of the powders. TEM is an optical analogue to the conventional light microscope. It is based on the fact that electrons can be ascribed a wavelength (of the order of 0.25 nm), but at the same time interact with magnetic fields as a point charge. A beam of electrons is applied instead of light, and the glass lenses are replaced by magnetic lenses. The lateral resolution of the best microscopes is down to atomic resolution. A schematic diagram of a TEM is shown in Figure 2.5.

Electrons thermionically emitted from a hot filament (electron gun) are accelerated to 100 keV or higher and first projected on to the specimen by means of the electromagnetic lens systems. The scattering processes are experienced by electrons during their passage through the specimen determine the kind of information obtained. Elastic scattering, involves no energy loss when electrons interact with the potential field of the ion cores, gives rise to diffraction pattern. In-elastic scattering between beam and matrix electron at heterogeneities such as grain boundaries, dislocations, second-phase particles, defects, density variations, cause complex absorption and scattering effects. The generation of characteristic X-rays and Auger electrons also occurs, but these by-products are not usually collected in a typical TEM measurement.

The emergent primary and diffracted electron beams are now made to pass through a series of post-specimen lenses. The objective lens produces the first image of the object. Depending on how the beams reaching the back focal plan of the objective lens are subsequently processed distinguishes the operation modes. Basically, either

magnified images or diffraction patterns are obtained. The image can be studied directly by the operator or photographed with a camera.

For TEM observation, the sample in the form of powder was dispersed in dimethyl formamide (DMF) solvent using an ultrasonicator. A drop of the colloidal solution was placed on a copper coated TEM grid and allowed to dry in a clean environment. The grid with the dried powder particles was then used for the TEM observation.

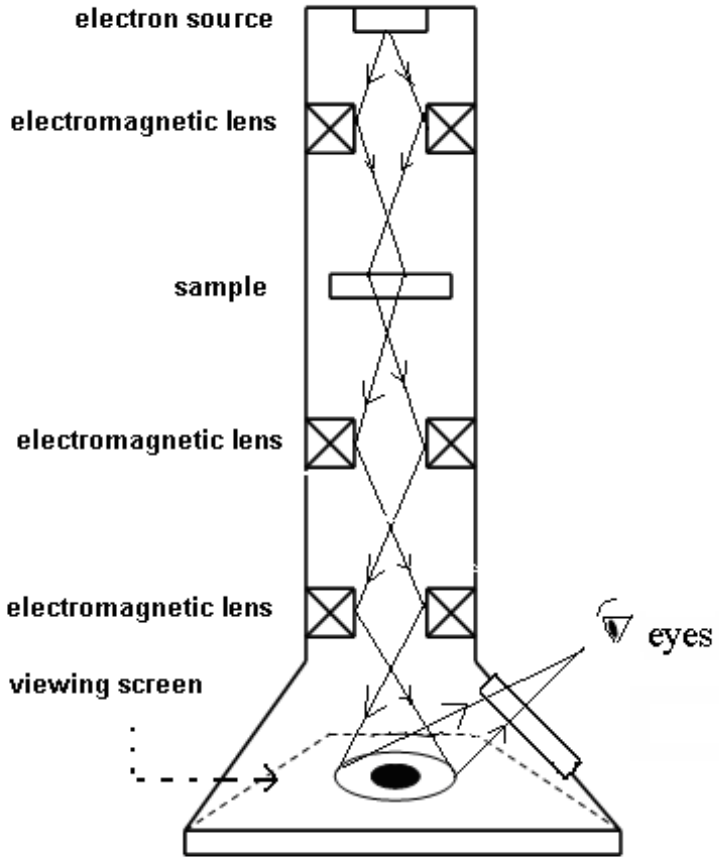

Figure 2.5: Schematic diagram of a TEM.

2.3. Thermal measurements

Thermal measurements involving the measurement of endothermic and exothermic reactions, their enthalpies and specific heats can be performed using an adiabatic calorimeter or a differential scanning calorimeter. The latter technique is rapid, requires small amounts of samples and easy to perform with commercially available equipment.

2.3.1. Differential scanning calorimeter (DSC)

A Differential Scanning Calorimeter (DSC, Perkin-Elmer DSC 7) has been used in the present thesis work for thermal characterization of powders. DSC is a thermo-analytic technique in which the difference in the amount of heat required to increase the temperature of a sample and a reference material is measured as a function of temperature. The DSC curves are recorded either under a constant heating (or cooling) rate or under isothermal conditions (time scan at a constant temperature). A typical DSC consists of two isolated sealed pans, one containing the sample and the other a reference material (generally, Al_2O_3 or just the empty Al pan). The pans are covered with Al covers, which act as a radiation shield (Figure 2.6). The two pans are heated or cooled uniformly while the heat flow difference between the two is monitored. The basic principle underlying this technique is that, when the sample undergoes a physical transformation such as phase transition, more or less heat will need to flow to it than the reference in order to maintain both at the same temperature. More or less heat flowing would depend on the process being exothermic or endothermic. In the power compensation type DSC, the heat is supplied to either of the pans so that both are maintained at the same temperature. The heat flow (dH/dt) is then estimated from this

data. In a DSC based on the heat-flux technique, the temperature difference (ΔT) between the two isolated pans is measured from which the heat flow is estimated.

A commercial DSC (PerkinElmer, DSC7) based on the power compensation technique was used in the current investigations. About 10 mg of powder was put in an alumina pan and the thermal transformations occurring during heating cycle under a constant heating rate was studied. The runs were programmed and the DSC curves (dH/dt versus T data) were recorded and analyzed using the Pyris™ software. Temperature and enthalpy calibrations were performed using standard samples (In and Zn). High purity nitrogen gas was purged continuously throughout the runs.

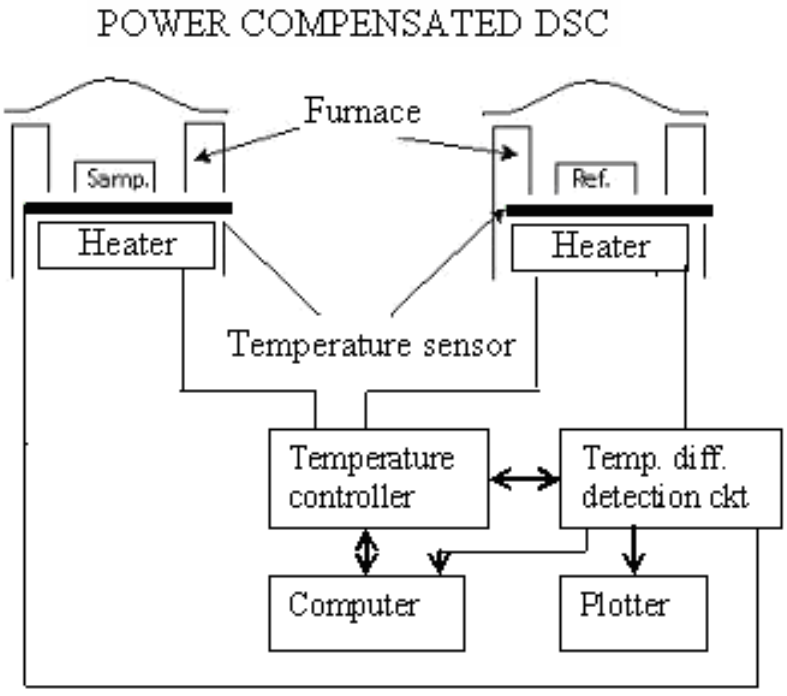

Figure 2.6: Schematic diagram of a DSC.

2.4. Magnetic measurements

2.4.1. Vibrating sample magnetometer (VSM)

Vibrating Sample Magnetometer (VSM, Lakeshore 7410) has been used for the magnetic measurements. A schematic diagram of a VSM has been shown in Figure 2.7.

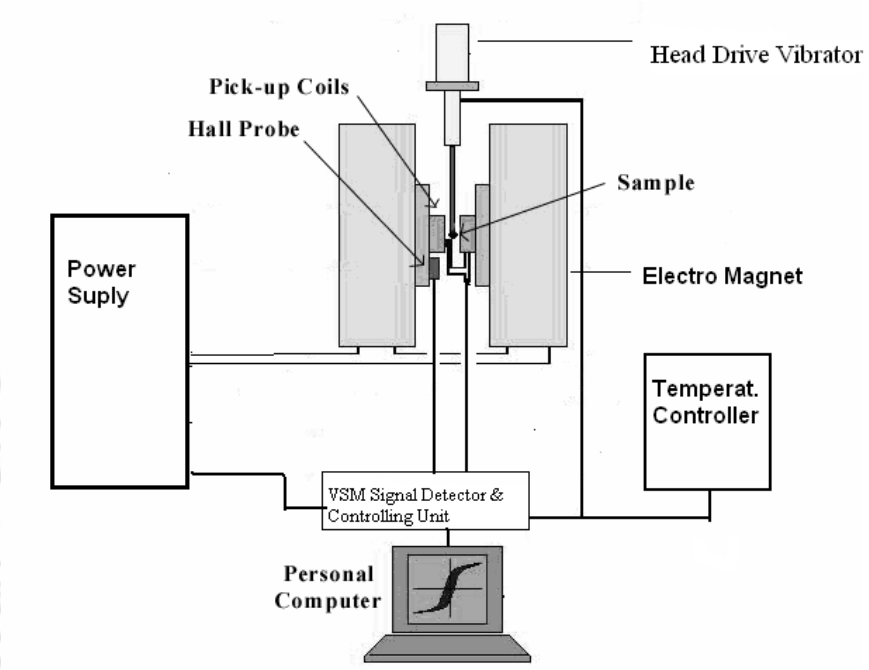

Figure 2.7: Schematic diagram of a VSM.

When a sample is placed in a uniform magnetic field, a dipole moment proportional to the product of the sample susceptibility and the applied field is induced in the sample. If the sample is made to undergo sinusoidal motion, an electrical signal can be induced in suitably located stationary pickup coils (Figure 2.7). This signal has amplitude proportional to the magnetic moment of the sample, the vibrating amplitude and the vibration frequency. Through the use of lock-in-amplifier and feedback techniques, only that portion of the signal arising from the magnetic moment is picked up and is converted into direct read-out in the unit of magnetization on a digital panel meter. The VSM consists of the following major parts, 1. water cooled electromagnet and power

supply, 2. vibration exciter and sample holder (with angular position indicator), 3. sensing coils, 4. Hall probe, 5. amplifier, 6. control chassis, 7. lock-in amplifier and 8. computer interface.

The sample is fixed to the lower end of the quartz sample holder. The measurement sequence is then programmed using the software provided with the instrument. The vibration exciter is then started and the signal received from the probe and the pick up coils is converted into the magnetic moment value of the sample. Magnetic field up to 20,000 Oe can be applied to the sample. Normally, magnetic field is automatically increased in steps at a constant temperature (magnetization, M, *versus* magnetic filed, H, measurements] by setting the program. For high temperature measurements (magnetization, M, *versus* temperature, T, measurements), a high temperature attachment (Lakeshore) capable of providing a controlled heating/cooling of the sample from room temperature to 1223 K was used. For $M - T$ measurements a constant (slow) heating rate was maintained using the software supplied with the instrument.

Chapter 3

Mechanical alloying of Fe-Si and Fe-Si-M (M = Al, B, Cr) powders

A systematic study of the evolution of nanocrystalline structure in Fe-Si and Fe-Si-M (M = Al, B, Cr) powders on mechanical alloying and the correlation between structure and magnetic properties of the milled powders are presented in this chapter.

3.1. Experimental details

Weighed quantities of high purity (> 99.9%) elemental Fe, Si and M powders corresponding to atomic compositions $Fe_{75}Si_{25}$ and $Fe_{75}Si_{25-x}M_x$(M = Al, B, Cr; x = 5, 10) were taken in a hardened steel vial together with 7 mm diameter hardened steel milling balls. The powder to ball weight ratio was maintained at 1:10. The vial was filled with high purity argon gas to prevent oxidation of the high purity elemental powder during milling. The planetary ball mill (Insmart, India) was operated at 300 rpm. Powder

samples were taken from the mill at selected time intervals for the structural and magnetic properties analysis. The powder samples were analyzed by X-ray diffractiometer (XRD, Seifert 3003 T/T), transmission electron microscope (TEM, JEOL 2100) and scanning electron microscope (SEM, Leo 1430VP) with energy dispersive spectroscopy (EDS) attachment as per procedures outlined in the previous chapter. XRD data was collected at a slow scan rate of 0.005^{o}/s for the careful determination of average crystallite size and dislocation density of the milled powders. Room temperature and high temperature magnetic properties of the samples were measured using vibrating sample magnetometer (VSM, Lakeshore 7410) described in chapter 2.

3.2. Mechanical alloying of Fe-Si powders and evaluation of their properties

3.2.1. Structural evolution during milling

Figure 3.1 depicts the XRD patterns of $Fe_{75}Si_{25}$ and powders milled for various time periods. The as-mixed powders show the Bragg reflections from the planes of the individual elements Fe and Si. After 5 hours of milling, the reflections corresponding to Si disappeared, leaving behind only bcc α-Fe reflections. This shows that Si has dissolved in the α-Fe matrix, forming a non-equilibrium solid solution α-Fe(Si). Further, the widths of α-Fe(Si) reflections increased with increasing milling time periods, indicating the formation of highly refined and strained alloy powders. In addition, there is a measurable shift in the peak positions with milling time, which showed that there is a change in the lattice parameter during the milling process.

Figure 3.2 summarizes the variation of lattice parameter with increasing milling time periods. The changes in the lattice parameter indicate the occurrence of atomic

disorder during the milling process. The lattice parameter decreased from 0.2866 nm to nearly stable values after 40 hours of milling. This behaviour could be attributed to substitutional dissolution of Si in Fe matrix since atomic radius of Si (0.118 nm) is smaller than Fe (0.123 nm). The degree of dissolution of Si in α-Fe may be estimated quantitatively from the studies performed on rapidly quenched Fe-Si alloys [40] which indicated a decrease in the α-Fe lattice parameter of approximately 0.000065 nm per atomic percent of Si in bcc α-Fe. In the present study, the 80 hours milled powders showed a change of 0.00133 nm in lattice parameter which accounts for nearly 82% of Si occupancy in bcc α-Fe with the rest 18% predominantly residing in grain boundaries.

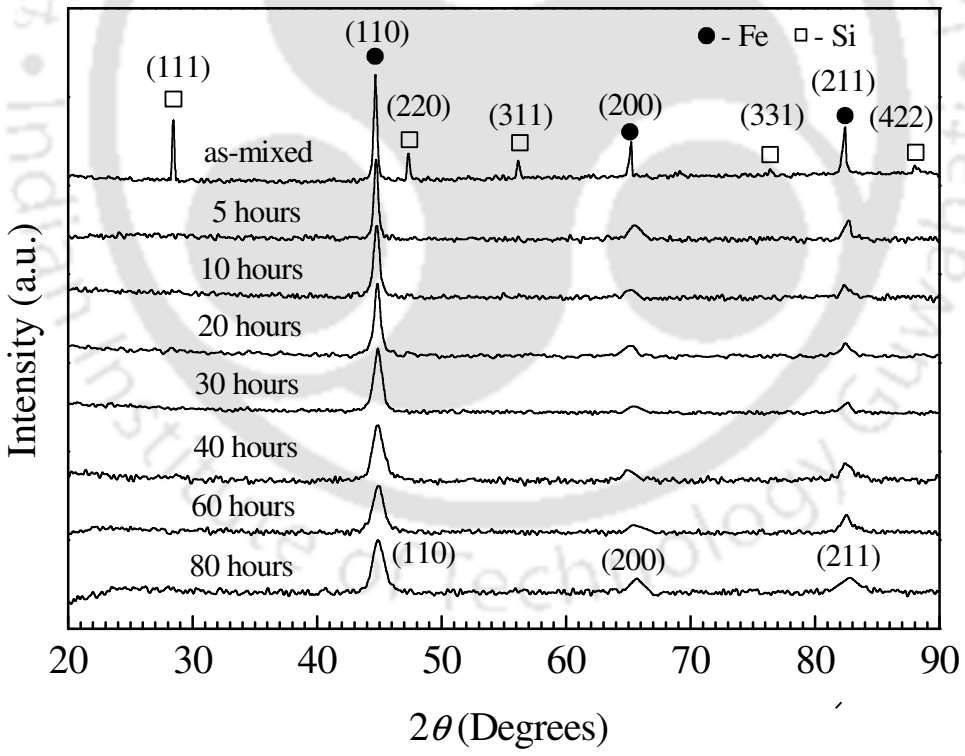

Figure 3.1: XRD patterns of $Fe_{75}Si_{25}$ powders milled for various milling time periods.

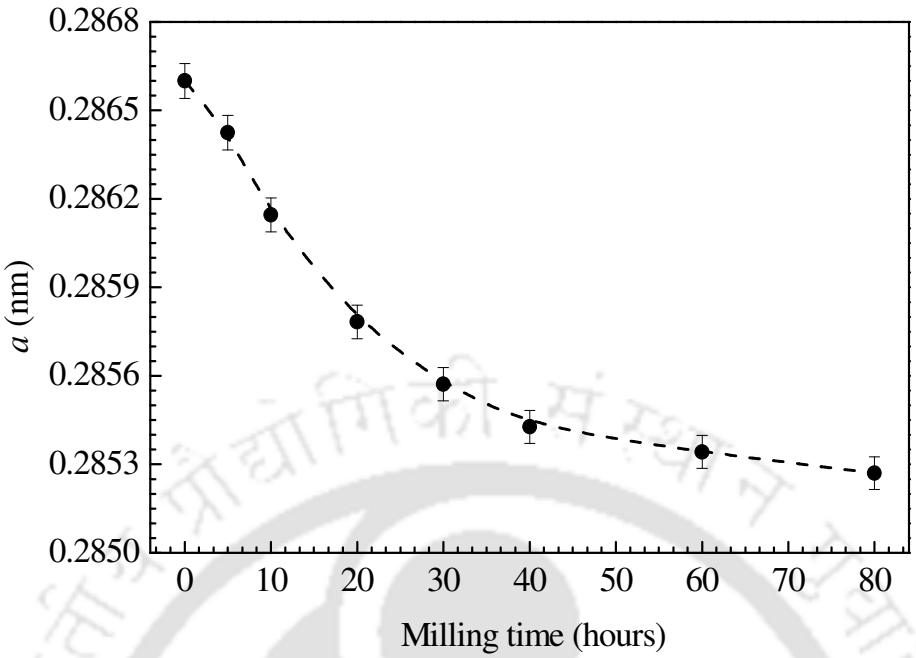

Figure 3.2: Variation of lattice parameter (a) of $Fe_{75}Si_{25}$ powders with milling time.

The Bragg peak profiles in the XRD pattern have been analyzed using the Williamson-Hall (WH) method. According to this method [48], the individual contributions to the broadening of the Bragg reflections can be expressed as

$$\delta(2\theta)\cos\theta_0 = \frac{0.9\lambda}{D_{WH}} + 4e\sin\theta_0 \qquad (3.1)$$

where $\delta(2\theta)$ is full width at half maximum (FWHM) of the Bragg peaks (in radians), θ_0 is the Bragg angle of the analyzed peak and λ is the wavelength of the X-rays (λ = 0.154056 nm for Cu-K_α), D_{WH} is the average crystallite size and e is the strain. The FWHM $\delta(2\theta)$ of each reflection has been corrected using for instrumental broadening using the parabolic approximation correction relation [47]

$$\delta(2\theta) = B\left(1 - \frac{b^2}{B^2}\right)^{1/2} \qquad (3.2)$$

where B and b are the FWHM of the same Bragg reflection for experimental and reference powders respectively. Pure Fe powder annealed at 1273K for 24 hours have been used as the reference powder to find values of b for different Bragg reflections.

All Fe reflections within the 2θ range of 20° to 90° were used to construct a linear plot of $\delta(2\theta)\cos\theta_0$ versus $\sin\theta_0$ (*cf.* inset of Figure 3.3), from which the average crystallite size and the strain were obtained using equation (3.1). Figure 3.3 shows the variation of the average crystallite size and strain of milled $Fe_{75}Si_{25}$ powders determined using equation (3.1). It is apparent from Figure 3.3 that the average crystallite size decreases and the internal strain increases with increasing milling time period and subsequently attain saturation values.

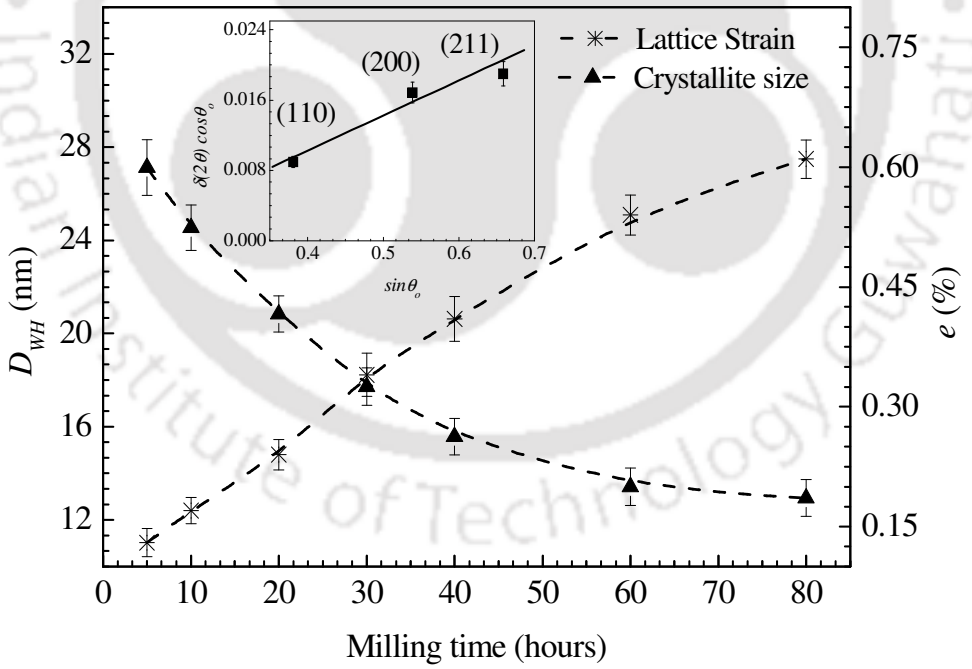

Figure 3.3: Variation of average crystallite size (D_{WH}) and lattice strains (e) with milling time periods for $Fe_{75}Si_{25}$ powders, determined using WH method. Inset: The WH plot for 5 hours milled powder.

The inset in figure 3.3 shows a typical linear fit to the data corresponding to equation (3.1). It is evident that the data does not entirely obey the linear WH formulation. The deviation observed in the data might be due to the existence of anisotropic variation in the residual strain. Hence, certain Bragg reflections may exhibit a larger strain component than others. Ungar *et al.* modified the WH method by the introduction of a dislocation contrast factor in what is known as the modified Williamson-Hall (MWH) method [49,50]. According to the MWH method

$$(\Delta K)^2 = \left(\frac{0.9\lambda}{D_{MWH}}\right)^2 + \left(\frac{\pi b^2 \rho}{2B}\right) K^2 C_{hkl} \tag{3.3}$$

where, $\Delta K = (2\cos\theta_B \Delta\theta_B)/\lambda$, θ_B is the Bragg angle of the analyzed peak (in degree), $\Delta\theta_B$ is full-width at half maximum (FWHM) of the peak in radian, λ is the wavelength of X-rays (= 0.15406 nm for Cu-K_α line), D_{MWH} is the average crystallite size, b is the modulus of the Burger vector of dislocation, ρ is the average dislocation density, B is a constant that can be taken as 10 for a wide range of dislocation distributions [51], $K = 2\sin\theta_B/\lambda$ and C_{hkl} is the dislocation contrast factor for different Bragg reflections (where *hkl* denote the Miller indices of the reflections). The modulus of Burger vector b is related to the lattice constant a by the relation $b = \sqrt{3}/2\ a$ [35]. The values of C_{hkl} can be calculated using the relation [51]

$$C_{hkl} = C_{hoo}(1 - qH^2) \tag{3.4}$$

where $H^2=(h^2k^2+k^2l^2+h^2l^2)/(h^2+k^2+l^2)^2$ for a cubic crystal system and q is a constant. Equations (3.3) and (3.4) lead to the relation

$$(\Delta K)^2 = \left(\frac{0.9}{D}\right)^2 + \left(\frac{\pi b^2 \rho}{2B}\right) K^2 C_{h00}(1 - qH^2) \tag{3.5}$$

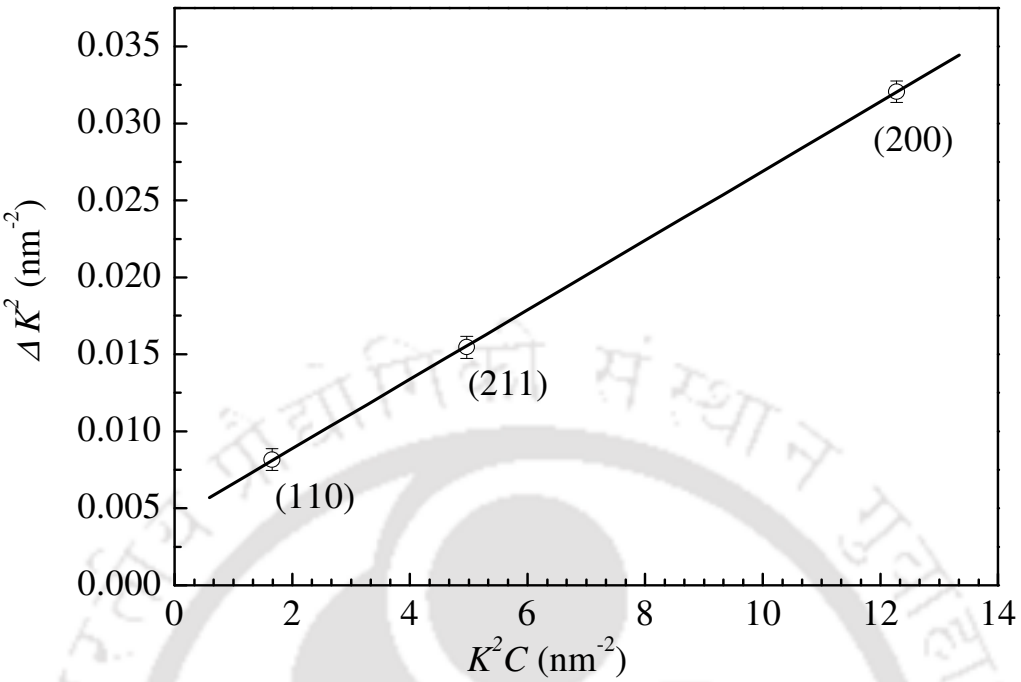

Figure 3.4: MWH plot for 5 hours milled $Fe_{75}Si_{25}$ powder.

The above equation can be rearranged as

$$\frac{(\Delta K^2 - \alpha)}{K^2} = \left(\frac{\pi b^2 \rho}{2B}\right) C_{h00}(1 - qH^2) \tag{3.6}$$

where $\alpha = (0.9/D)^2$. The usual procedure of estimating the value of q is to plot the left hand side of equation (3.6) against H^2 and extract the value of α corresponding to the best (least squares) linear fit to the data [51]. In the present case, there are two independent values of H^2 for the three measured reflections. However, it is obvious that in order to satisfy a linear relation, the left hand side of equation (3.6) should have the same value corresponding to the reflections having the same value of H^2. So, α (= 7.43 × 10^{-4} nm^{-2}) was determined by equating the values $(\Delta K^2 - \alpha)/K^2$ corresponding to the reflections from (110) and (211) planes. The value of q (= 2.9) was calculated from the slope and the

intercept of $(\Delta K^2 - \alpha)/K^2$ versus H^2 plot, which is in good agreement with the values obtained by Shen *et al*. [35] for Fe-Cu and Fe-Al-Si alloys. The average value of C_{200} was taken as 0.252 [35] and the values of C_{110} and C_{211} were evaluated using equation (3.4). Figure 3.4 shows the plot between K^2C and ΔK^2 of 5 hours milled $Fe_{75}Si_{25}$ powders according to equation (3.3). The average crystallite size and average dislocation density have been estimated using this method. It can be seen that all the reflections falls on a straight line in Figure 3.4 showing better applicability of the MWH method as compared to WH method for the present data.

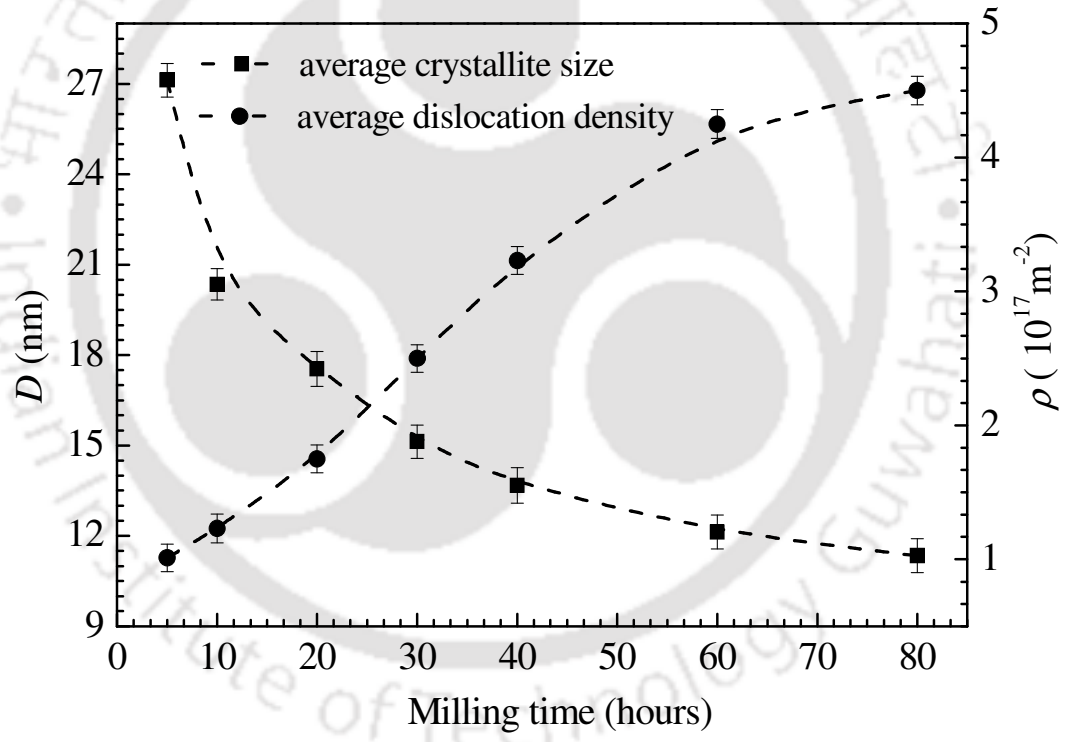

Figure 3.5: Variation of average crystallite size (D) and average dislocation density (ρ) of $Fe_{75}Si_{25}$ powders as a function of milling time.

Figure 3.5 summarizes the variation of average crystallite size (D) and the variation in average dislocation density (ρ) of $Fe_{75}Si_{25}$ powders as a function of milling time. The average crystallite size decreases linearly up to 40 hours of milling and then attained a nearly constant value, while the average dislocation density increases with increasing milling time and ultimately shows a tendency to saturate at longer milling time. This systematic structural study shows the development of non-equilibrium solid solution α-Fe(Si) with nanocrystalline structure during the MA process.

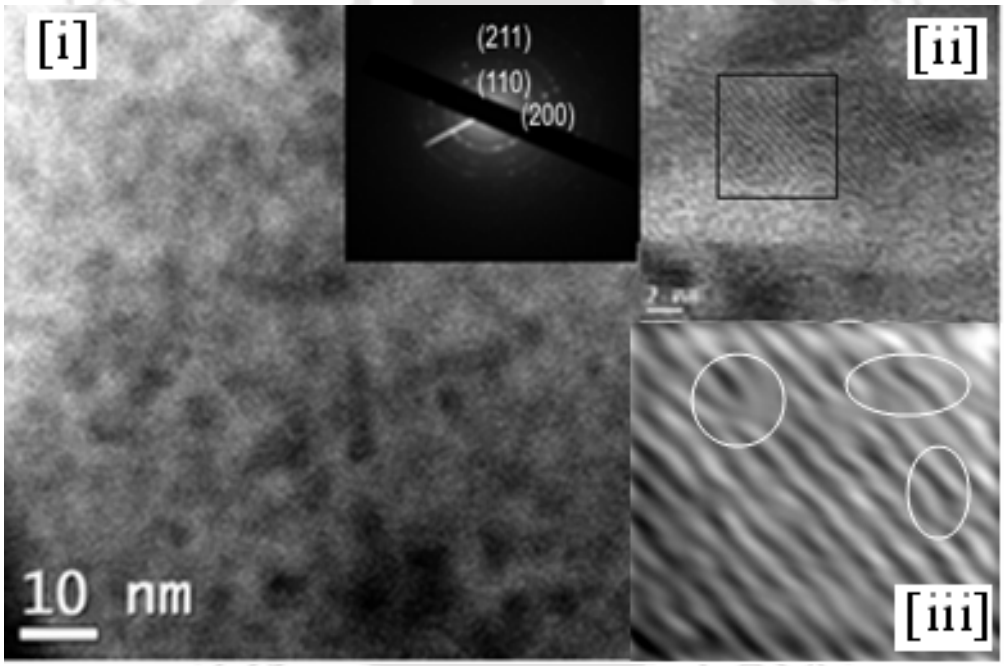

Figure 3.6: (i) BF-TEM images and SAED patterns, (ii) HRTEM images, and (iii) i-FFT images of selected area of HRTEM images [highlighted by square box in figure 3.6 (ii)] of $Fe_{75}Si_{25}$ powders milled for 80 hours.

In order to understand the development of nanocrystalline structure and to analyze the existence of defects in the nanostructure, TEM observations were carried out on the

80 hours milled $Fe_{75}Si_{25}$ powders. Figure 3.6 shows the bright field TEM (BF-TEM) images, selected area electron diffraction (SAED) patterns, high resolution TEM (HRTEM) images and inverse-Fast Fourier Transform (i-FFT) images of selected area of HR-TEM images of $Fe_{75}Si_{25}$ powders milled for 80 hours. Bright field image shows the fine-grain structure, which is a typical characteristic of mechanically alloyed powder particles. The non-uniform contrast inside each grain and along grain boundaries in bright field TEM images is indicative of the high degree of strain present in the as-milled powders. SAED patterns show the polycrystalline nature of the powders with the rings corresponding to reflections from (110), (200) and (211) planes of Fe. The *d*-spacing and lattice parameter were calculated from the diffraction pattern for the 80 hours milled samples.

These results agree well with the values obtained from XRD peak analysis. HRTEM images also support the presence of fine nanometer sized crystallites with high degree of strain. However, the existence of defects in the crystallites could not be directly observed from the HRTEM images. This is mainly due to the limitation of the TEM instrument used for observing such high resolution images. In order to analyze the existence of possible defects, the HRTEM images were resolved by i-FFT method using GATAN digital micrograph. The i-FFT images are shown in Figure 3.6 (iii) for $Fe_{75}Si_{25}$ powders. The i-FFT images of the selected area of the HRTEM images show the presence of dislocations, which are highlighted by circle(s). These results show that a highly strained and defective nanostructure has been formed after 80 hours of milling in the investigated sample.

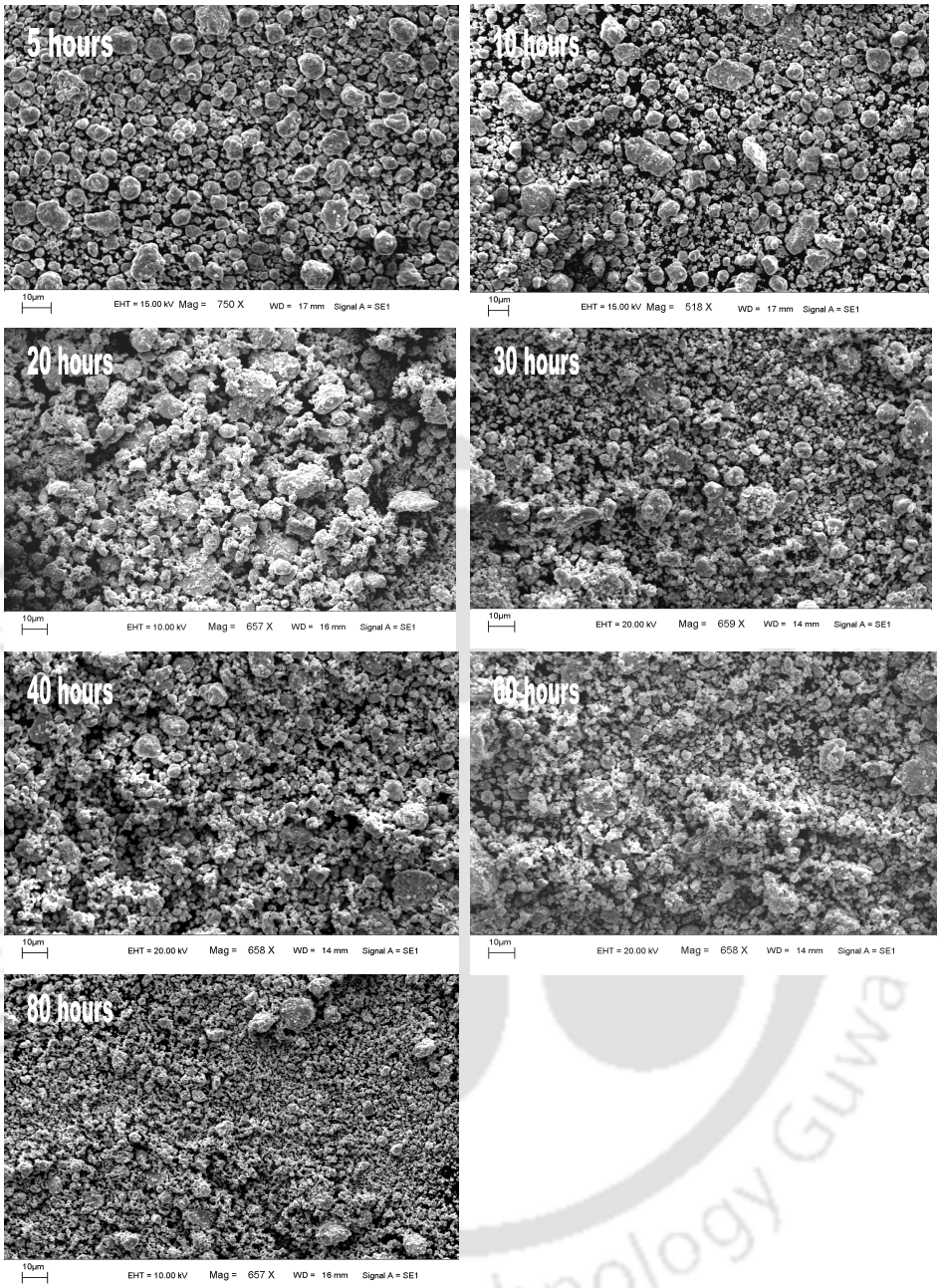

Figure 3.7: SEM micrographs of $Fe_{75}Si_{25}$ powders milled for various time periods.

Change of morphology of the powder particles with increasing milling time periods can be observed from the SEM micrographs of various hours milled powders presented in Figure 3.7. The average particle size, resulting from the aggregation of many

crystallites, has an irregular morphology up to 20 hours of milling. The particle size distribution is also found to be relatively inhomogeneous. Such aggregates are typical of mechanically alloyed powders and result from the repeated cold-welding and fracture of powders during ball milling [52]. For higher milling time periods, the particle size becomes smaller and the size distribution becomes narrower. The average crystallite size calculated from the XRD analysis is about 10 nm for 80 hours milled powders. These results show that the particles with sizes ranging from few hundred nanometers to few micrometers are agglomerations of nanosized (~10 nm) crystallites.

3.2.2. Evolution of magnetic properties during milling

To understand the effect of milling on the soft magnetic properties, room temperature magnetic hysteresis ($M - H$) loops with applied field extending up to ± 20 kOe were obtained. Figure 3.8 depicts the $M - H$ loops of the powders milled for various time periods. Inset in Figure 3.8 shows the expanded view of the $M - H$ curves close to the origin. The hysteresis loops shown in Figure 3.8 are typical of soft magnetic materials. The saturation magnetization of the powder measured at 20 kOe decreases gradually with increasing milling time periods. Figure 3.9 summarizes the variation of average magnetic moment (μ) per iron atom (measured at 20 kOe) and coercivity (H_C) of $Fe_{75}Si_{25}$ powders with increasing milling time. The average magnetic moment decreases with increasing milling time. Progressive Si substitution in Fe during the course of the milling process induces a partial filling of the Fe 3*d* bands with 3*p* electrons [53] which results in the observed reduction of average magnetic moment of Fe during the milling process [35]. Further, since considerable number of Fe atoms are expected to be present in the grain

boundaries and this can result in an increase in the inter-atomic distances spatially between Fe neighbors [54,55]. An increase in inter-atomic distances between Fe neighbors can contribute to the lowering of saturation magnetization of the powders.

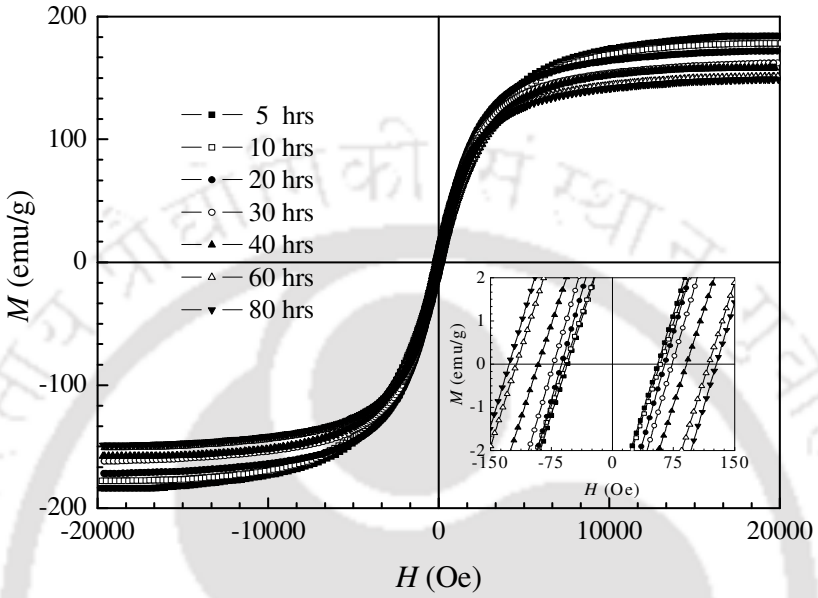

Figure 3.8: $M - H$ loops of $Fe_{75}Si_{25}$ powders milled for various milling time periods. Inset shows the expanded view of the $M - H$ loops near the origin.

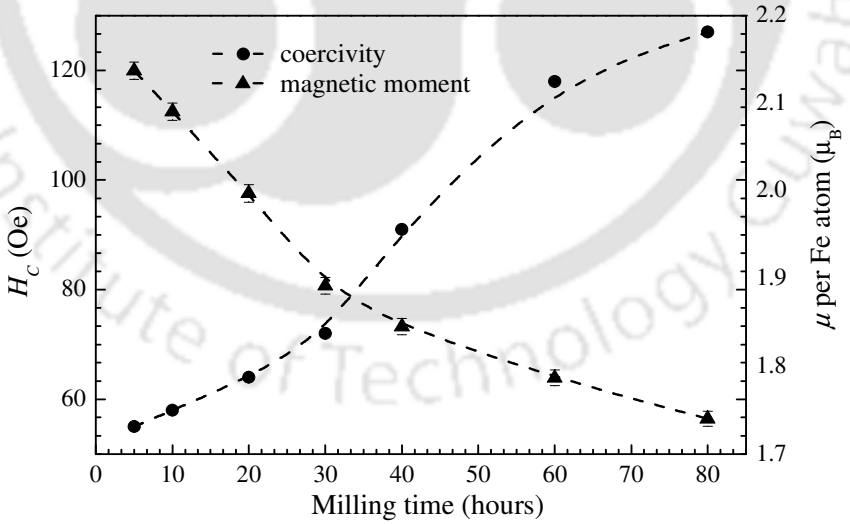

Figure 3.9: Variation of coercivity (H_C) and average magnetic moment (μ) per Fe atom of $Fe_{75}Si_{25}$ powders as a function of milling time.

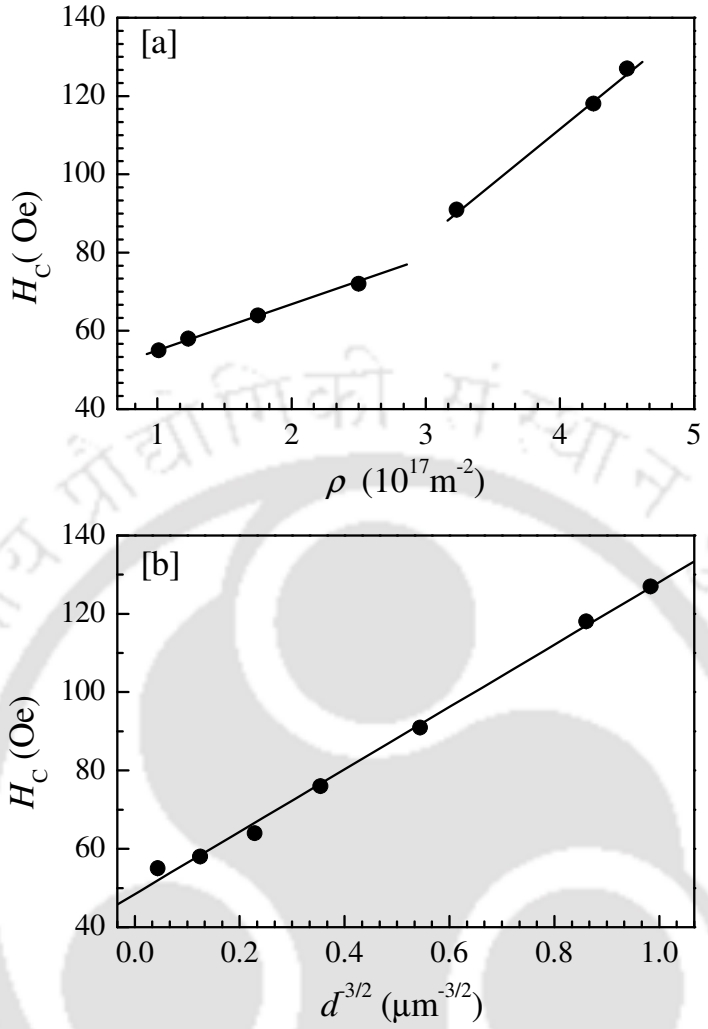

Figure 3.10: (a) Variation of coercivity (H_C) of $Fe_{75}Si_{25}$ powders as a function of dislocation density (ρ). The solid line in the figure is a guide to the eyes. (b) Plot of coercivity (H_C) of $Fe_{75}Si_{25}$ powders versus $d^{3/2}$. The solid lines represents the least squares fit of $d^{3/2}$ law [equation (3.8)] to the data.

The coercivity of the powders increases with increasing milling time. In order to understand the various contributions to the coercivity, coercivity has been plotted as a function of dislocation density in Figure 3.10(a). It could be clearly seen from the figure that the variation of coercivity with dislocation density shows two distinct regions of

nearly linear behavior. According to Neel's theory [56], randomly distributed internal stresses (σ) introduced during milling in the samples with local magnetostriction constant (λ) are expected to increase the coercivity. In addition, if the magneto-elastic energy ($\lambda\sigma$) is larger than the anisotropy energy, the coercivity is likely to be proportional to the dislocation density (ρ). Thus, a linear relationship between coercivity and dislocation density in samples milled up to 30 hours is in good agreement with Neel's theory. If dislocation defect is the only factor responsible for the increase of coercivity with milling time, then the linear relationship between dislocation density and coercivity is expected to hold for the entire range of milling time. However, the observed deviation in the initial linear behaviour of coercivity with milling time beyond 30 hours indicates that factors other than dislocation defects contribute to the coercivity of the powders milled beyond 30 hours. Since the particle size also decreases with milling time periods, it can be expected that the coercivity of the powders also depends on particle size. In a soft magnetic random anisotropy system with dislocation density (residual stress), the effective anisotropy constant is given by [4, 23, 24, 35]

$$K_{eff} = \frac{\sqrt{k_{\sigma,ma}^2 + < k_{\sigma,mi} >^2 + < k_1 >^2}}{\sqrt{N}} \tag{3.7}$$

where N is the maximum number of average crystallites oriented randomly but coupled ferromagnetically, k_1 is the magnetocrystalline anisotropy of the material, and $k_{\sigma,ma}$ and $k_{\sigma,mi}$ are averaged long-range and short-range magneto-elastic anisotropies, respectively. Ferromagnetic domains have been found [57] to extend over several hundred micrometers. Hernando *et al.* [58] have shown that in the case of mechanically alloyed

materials, when the volume of the sample (v) is smaller than that of the domain, the average anisotropy can be expressed as

$$K_{eff} \approx \frac{\sqrt{k_{\sigma,ma}^2 + < k_{\sigma,mi} >^2 + < k_1 >^2}}{\sqrt{v}} \approx \frac{\sqrt{k_{\sigma,ma}^2 + < k_{\sigma,mi} >^2 + < k_1 >^2}}{\sqrt{d^3}} \tag{3.8}$$

According to equation (3.8), the coercivity should show a linear dependence on $v^{-1/2}$ (or $d^{-3/2}$), where d is the average particle size. Interestingly, a reasonably good fit to equation (3.8) has been obtained [*cf.* Figure 3.10(b)] for the present. The average size of the powder particles (d) has been estimated from the SEM micrographs presented earlier using the computer software *Image J* [59]. This analysis indicates that the increase in the coercivity is not only due to the increase in average dislocation density, but also due to the increase in effective anisotropy due to the decrease of size of the powder particles during milling. This contribution to coercivity is especially prominent for powders milled for longer (greater than 30 hours in this case) time periods.

The effective magnetic anisotropy of the powders have been calculated from the initial magnetization curves using the law of approach to saturation, defined as [60]

$$M = M_S\left(1 - \frac{\alpha}{H} - \frac{\beta}{H^2} - \cdots\right) \tag{3.9}$$

where the α/H term arises because of non-magnetic inclusions and structural defects, and the β/H^2 term is attributed to the effective magnetocrystalline anisotropy The parameter β is related to effective anisotropy constant K_{eff} for ferromagnets of cubic crystal structure by the relation [60]

$$\beta = \frac{8\ K_{eff}^{\ 2}}{105\ \ M_S^{\ 2}} \tag{3.10}$$

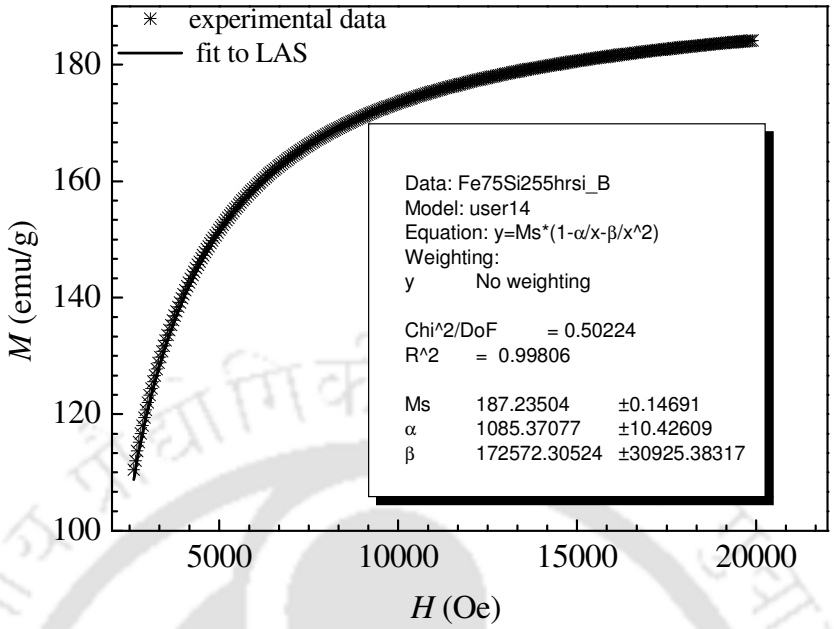

Figure 3.11: A typical fitting of LAS to 5 hours milled $Fe_{75}Si_{25}$ powders.

Table 3.1: Fitting parameters of $Fe_{75}Si_{25}$ powders milled for different time periods obtained by fitting the LAS to the initial magnetization curves.

$Fe_{75}Si_{25}$	***M_S* (emu /g)**	***α* (10^4Oe)**	***β* (10^4 Oe^2)**
5 hours	187.23 ± 0.11	0.1085 ± 0.0010	17.2572 ± 3.0925
10 hours	181.98 ± 0.13	0.0943 ± 0.0022	18.4372 ± 2.8134
20 hours	176.54 ± 0.09	0.0891 ± 0.0013	20.1359 ± 2.5752
30 hours	166.72 ± 0.10	0.0851 ± 0.0035	23.2474 ± 2.0931
40 hours	165.09 ± 0.09	0.0832 ± 0.0041	25.0292 ± 2.9572
60 hours	156.61 ± 0.08	0.0863 ± 0.0051	29.2683 ± 2.9661
80 hours	152.72 ± 0.08	0.0864 ± 0.003	32.0346 ± 2.9956

A least squares fitting procedure was applied to the experimental data to obtain the optimum values of the parameters in equation (3.9). A typical fitting of the LAS to the 5 hours milled powders is shown in Figure 3.11. The fitting parameters of $Fe_{75}Si_{25}$ powders milled for various time periods are listed in Table 3.1.

Figure 3.12 depicts the variation of effective anisotropy constant (K_{eff}) of $Fe_{75}Si_{25}$ powders with increasing milling time calculated using equation (3.10) and the values of M_S and β obtained using the LAS presented in Table 3.1. The values of K_{eff} are of the order of 10^5 Jm^{-3}, which are higher than that of bulk Fe (4.8×10^4 Jm^{-3}). The high values of K_{eff} can arise due to the large strain induced during the milling process [26, 61] and also due to the small size of the particles. A good correspondence between coercivity and effective anisotropy has been observed in the present studies.

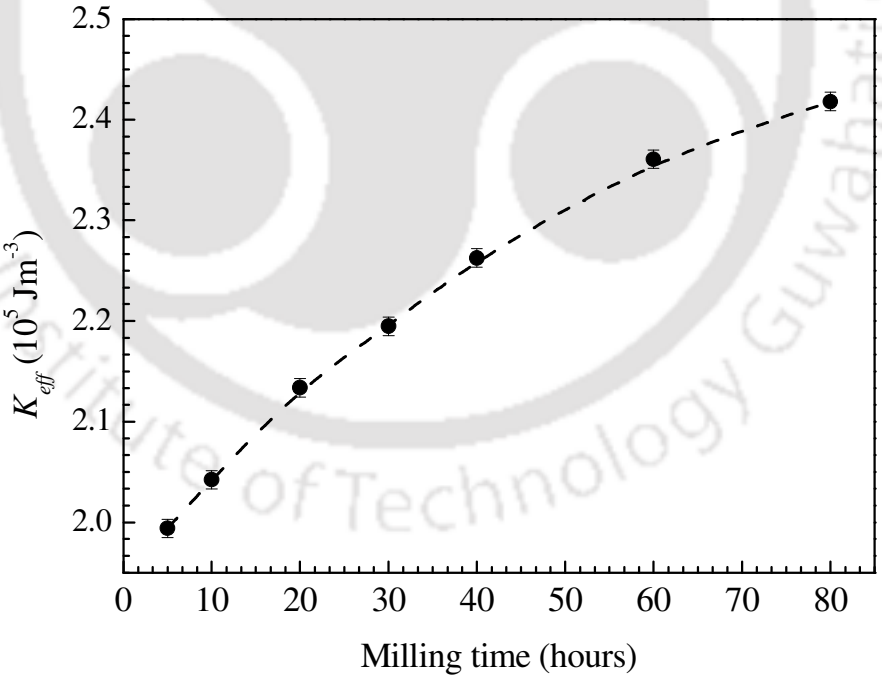

Figure 3.12: Variation of effective anisotropy constant (K_{eff}) of $Fe_{75}Si_{25}$ powders with increasing milling time periods.

Dislocations and grain boundaries increase the possibility of domain wall pinning, which in turn result in higher coercivity in the as-milled powders. The possibility of domain wall pinning at the grain boundaries and dislocations was investigated by analyzing the coercivities of different minor $M - H$ loops of thermally demagnetized 80 hours milled $Fe_{75}Si_{25}$ powders. Figure 3.13 shows the variation of coercivity obtained from various minor $M - H$ loops, measured with different maximum magnetic fields. Coercivity increases slowly [inset of Figure 3.13] for lower applied fields and then abruptly attains saturation value at higher applied fields. The low-field behavior is an indication of domain wall pinning due to dislocations and grain boundaries [62,63]. This argument is supported by the XRD and TEM results discussed earlier.

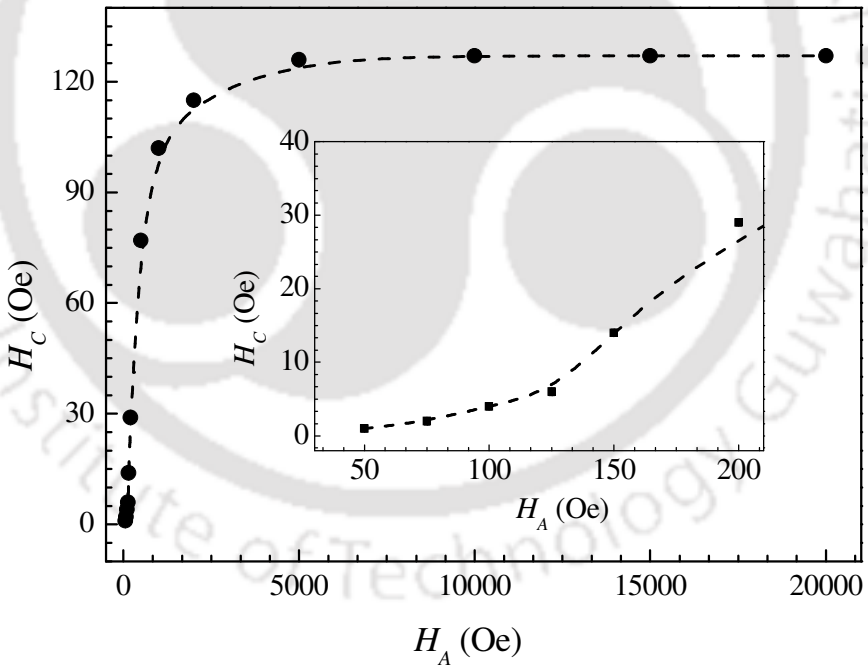

Figure 3.13: Dependence of minor hysteresis loop coercivity (H_C) on applied magnetic field (H_A) of 80 hours milled $Fe_{75}Si_{25}$ powders. Inset: The data close to the origin is shown in expanded scale.

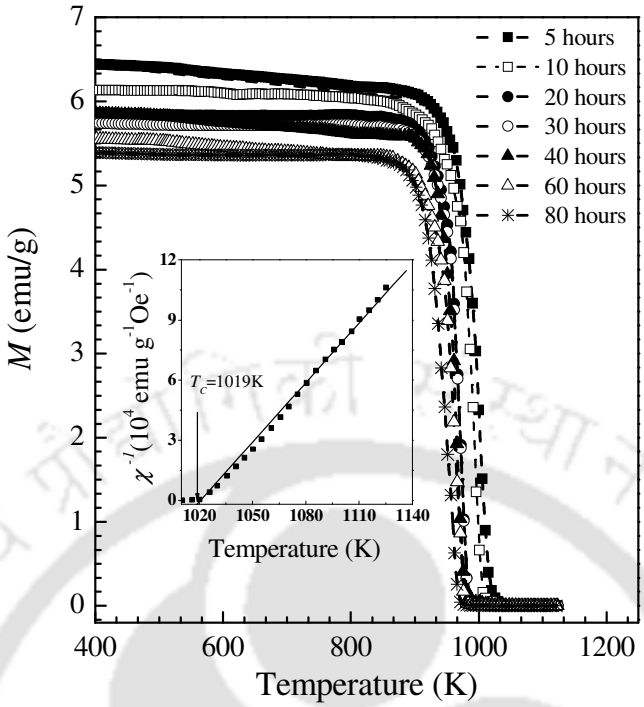

Figure 3.14: $M - T$ plots of $Fe_{75}Si_{25}$ powders milled for various time periods. Inset shows the fit to Curie-Weiss law for 5 hours milled $Fe_{75}Si_{25}$ powders. All $M - T$ plots were recorded under an applied field of 100 Oe.

In order to study the effect of milling on the Curie Temperature of $Fe_{75}Si_{25}$ powders, magnetization (M) versus temperature (T) at a constant applied dc magnetic field of 100 Oe has been obtained for powders milled for different time periods. Figure 3.14 shows the *M vesus T* plots for the $Fe_{75}Si_{25}$ powders milled for different time periods. The $M - T$ plots show a single phase transition from ferromagnetic to paramagnetic phase. The Curie temperature of the different hours milled powders was obtained using the Curie Weiss law [20]

$$\chi^{-1} = \frac{T - T_C}{C} \tag{3.11}$$

where $\chi = \frac{M}{H}$, H is the applied magnetic field which is taken 100 Oe for present studies, T_C is the Curie temperature and C is a constant known as Curie constant. The intercept of the linear plot between χ^{-1} and T obtained from the equation (3.11) gives the Curie temperature T_C. The plot between χ^{-1} and T of the 5 hours milled $Fe_{75}Si_{25}$ powder has been shown in the inset of Figure 3.14.

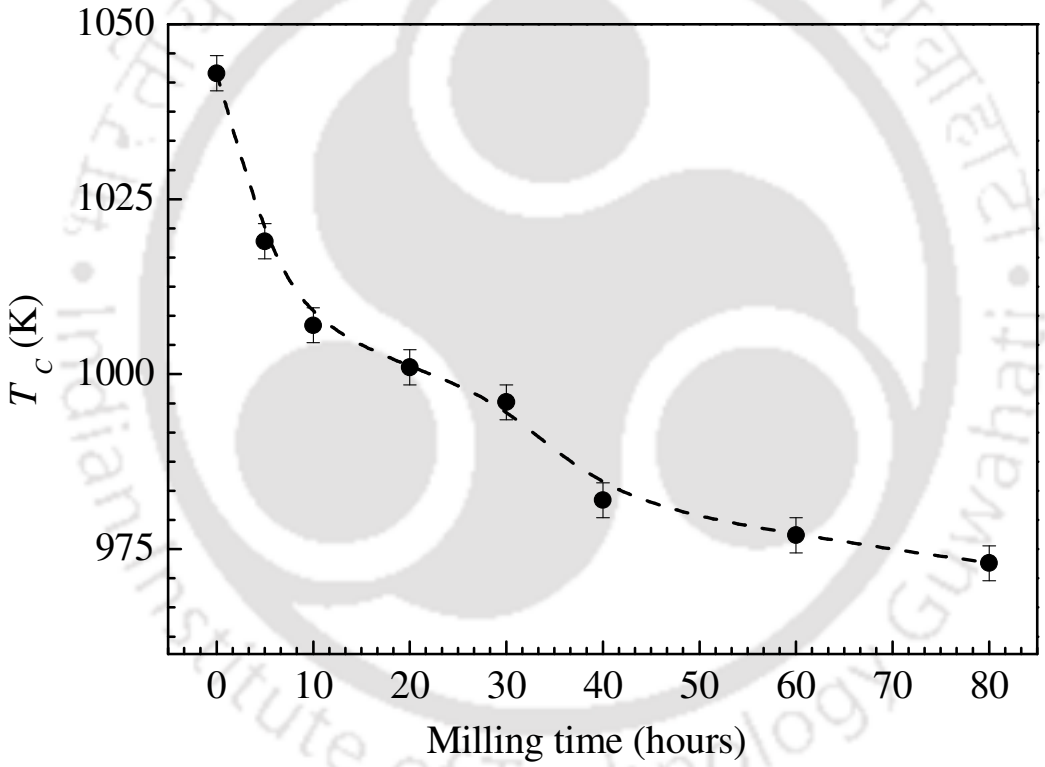

Figure 3.15: Variation of Curie Temperature (T_C) of $Fe_{75}Si_{25}$ powders with increasing milling time periods.

The variation of T_C of the $Fe_{75}Si_{25}$ powders with increasing milling time has been presented in Figure 3.15. T_C decreases rapidly from 1043 K of pure Fe to 1019 K after 5 hours of milling indicating the alloying of Fe and Si starts at lower milling time periods. A gradual decrease of T_C with increasing milling time periods indicates more number of Si atoms inducing into Fe matrix and thereby changing the value T_C of the materials. A similar trend of lattice parameter variation with increasing milling time periods (*cf.* Figure 3.2) indicates that the alloying process can be followed from both variation of lattice parameter and T_C. The value of T_C is 973 K for the powders milled for 80 hours, which is higher than that reported for melt-spun ribbons of composition $Fe_{75}Si_{25}$ which is 890 K [64]. The higher value of T_C can be related to the high strains induced during the milling process [65].

3.3. Mechanical alloying of Fe-Si-M (M=Al, B, Cr) powders and evaluation of their properties

3.3.1. Structural evolution during milling

XRD patterns of $Fe_{75}Si_{20}M_5$ (M = Al, B, Cr) and $Fe_{75}Si_{15}M_{10}$ (M = Al, B, Cr) powders milled for various time periods are presented in Figures 3.16 (a) – (c) and Figures 3.17 (a) – (c), respectively. Structural changes occurring in the powders as a function of milling time could be clearly seen from the figures. As-mixed powders show the characteristic Bragg reflections of the individual constituent elements Fe, Si and Al. The presence of Cr and B could not be observed in the XRD patterns of powders because the reflections from body centered cubic (bcc) Cr overlaps with that of α-Fe, and because of the inherent limitation of detecting B using XRD due to its low scattering factor, respectively. After 5

hours of milling, the reflections from Si and Al disappear leaving behind only the Fe reflections. This shows that Si and Al dissolved in the Fe matrix, forming a non-equilibrium solid solution α–Fe(Si,Al). Composition analysis was performed on 80 hours milled powders using EDS. The results of the analysis showed the overall composition to be $Fe_{75.1}Si_{19.2}Al_{4.7}$ and $Fe_{74.7}Si_{20.1}Cr_{5.2}$ ($Fe_{74.6}Si_{15.6}Al_{9.8}$ and $Fe_{74.2}Si_{16.1}Cr_{8.7}$) for $Fe_{75}Si_{20}M_5$ ($Fe_{75}Si_{15}M_{10}$) with M = Al or Cr, respectively. This indicates the presence of Si, Al and Cr in the form of solid solution in α-Fe. Compositional homogeneity in the powder supports our claim on the formation of α–Fe[Si(Al,Cr)] solid solution. Presence/dissolution of B in Fe matrix could not be detected by EDS due to its inherent limitation in detecting the light elements. However, the variation of the lattice parameter with increasing milling time periods discussed later confirms the presence of B in Fe matrix and the formation of non-equilibrium solid solution α–Fe(Si,B). In addition, the widths of the α–Fe[Si,(Al, B, Cr)] reflections increased with increasing milling time periods, indicating the formation of highly refined and strained alloy powders. It is important to note that no detectable reaction or compound formation was observed during the milling process since no new and/or additional reflections appeared in the as-milled XRD patterns. A measurable shift in the peak position of $Fe_{75}Si_{20}M_5$ (M = Al, B, Cr) powders with milling time enabled us to calculate the lattice parameter changes occurring during the milling process.

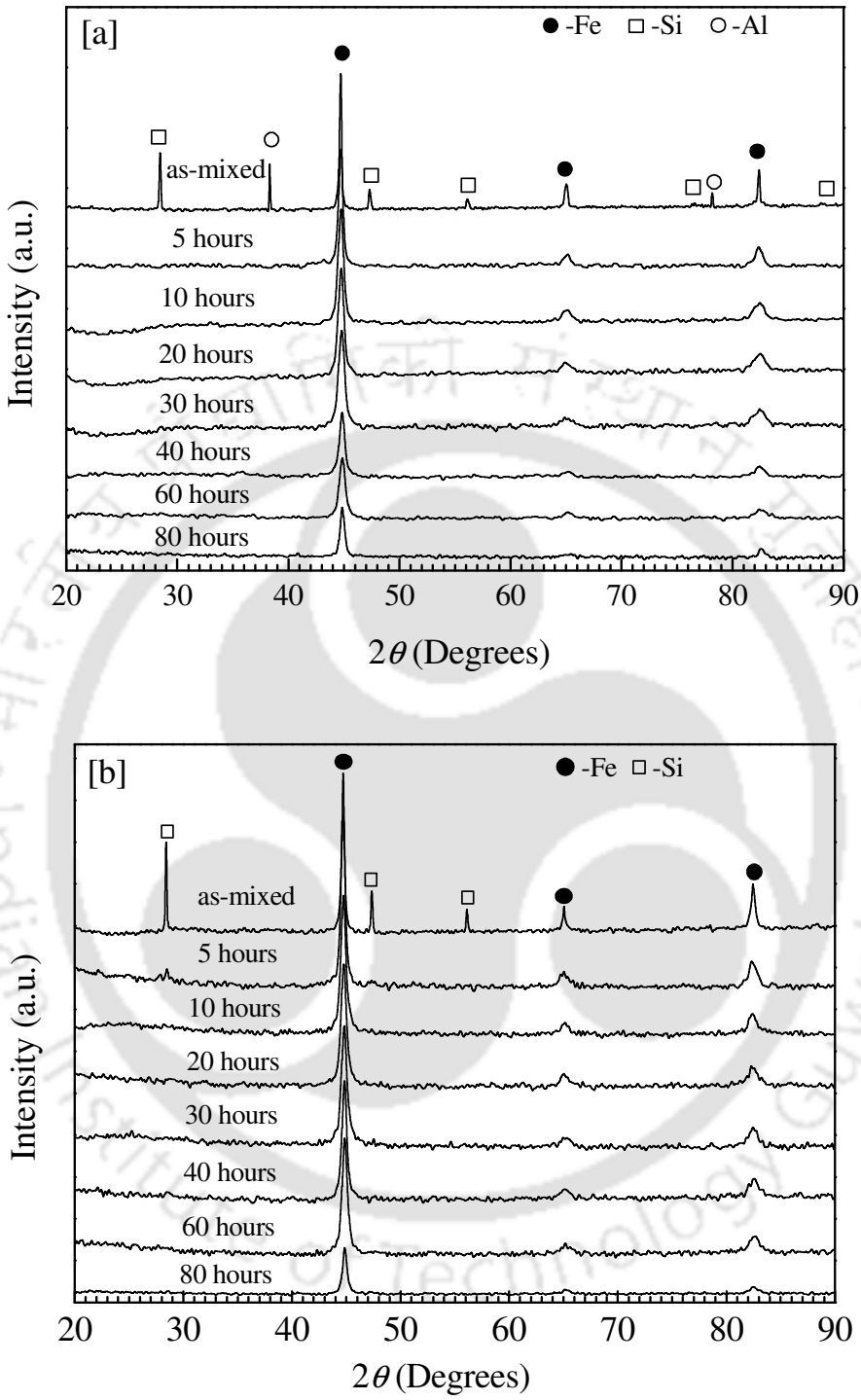

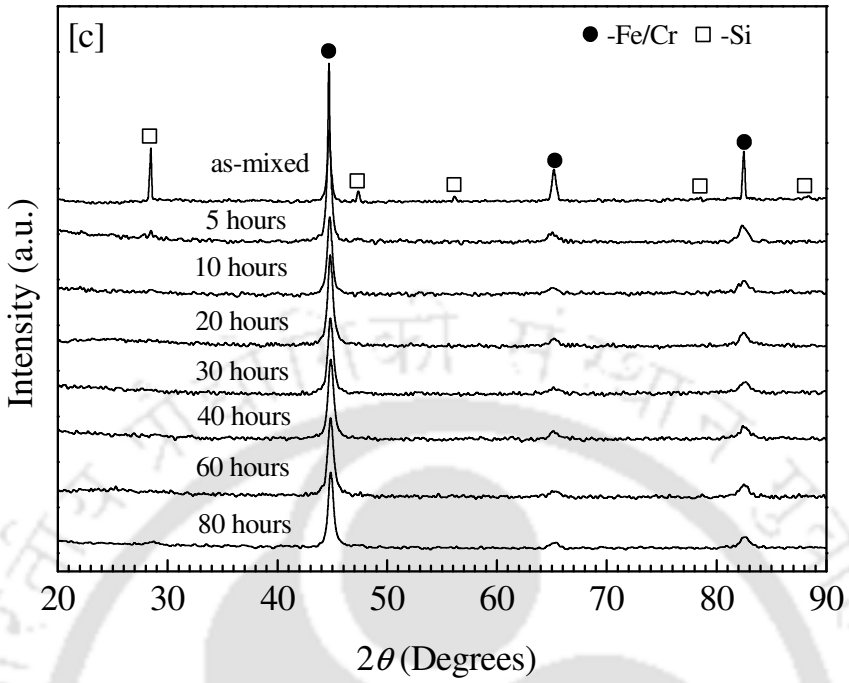

Figure 3.16: XRD patterns of $Fe_{75}Si_{20}M_5$ [M = Al (a), B (b) and Cr (c)] powders milled for different time periods.

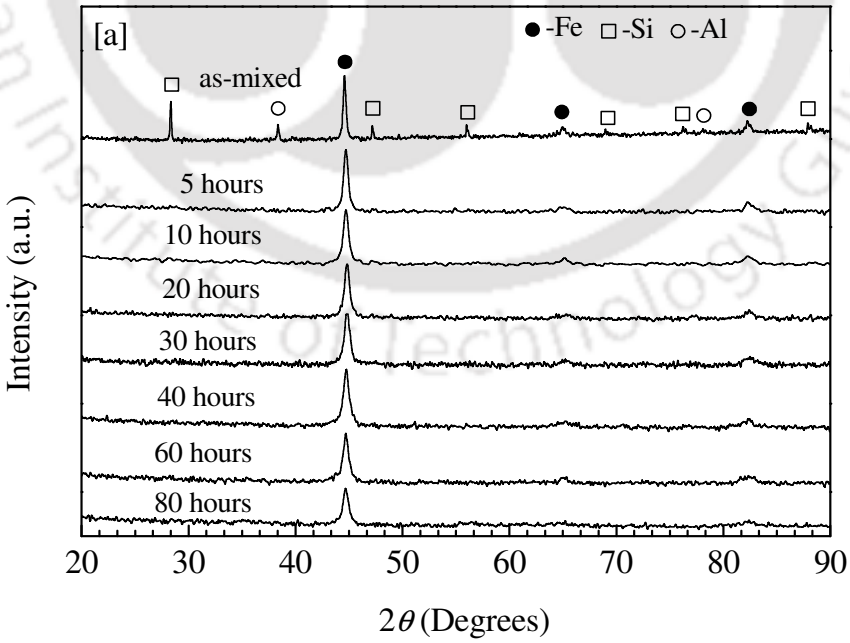

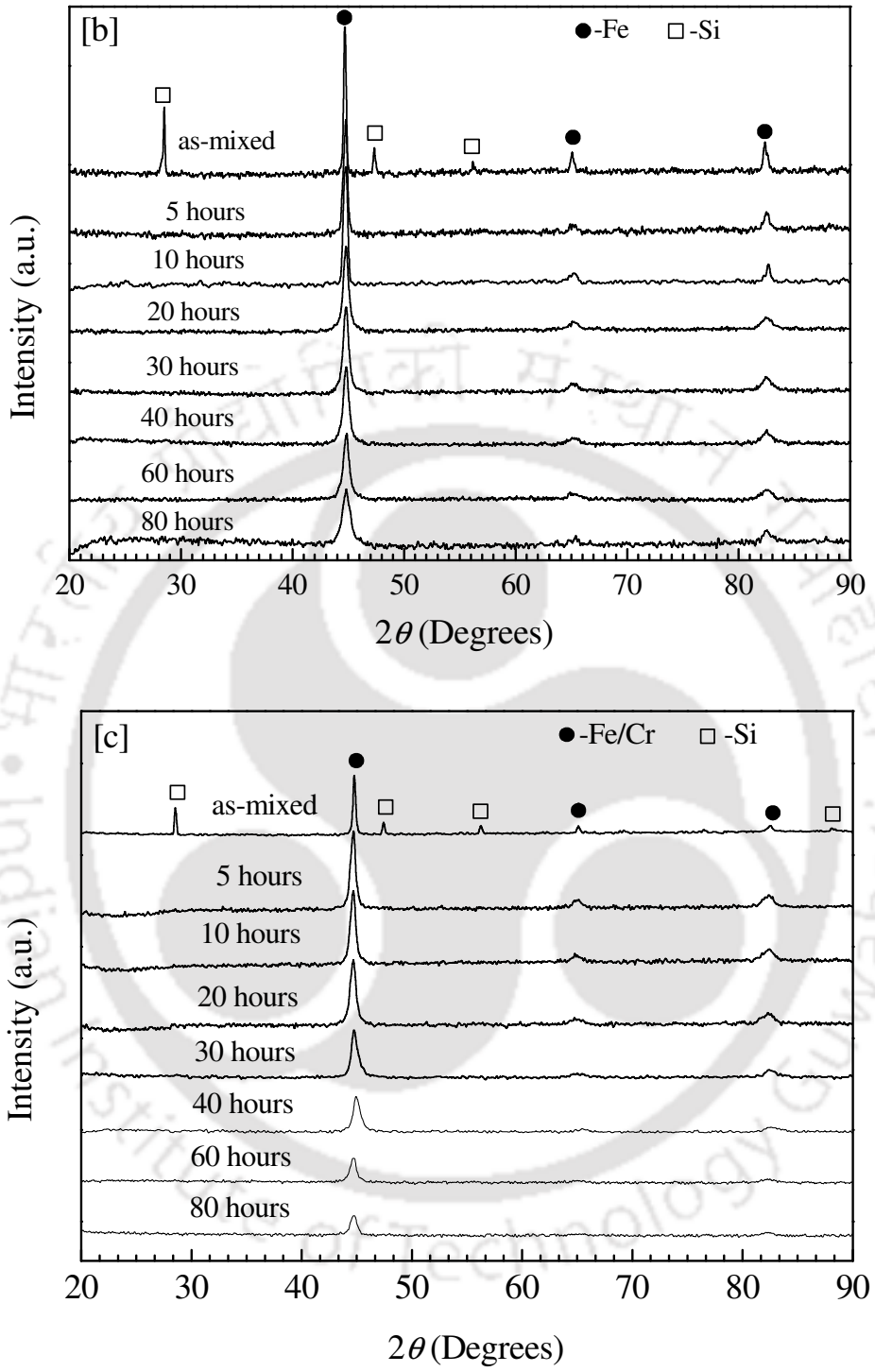

Figure 3.17: XRD patterns of $Fe_{75}Si_{15}M_{10}$ [M = Al (a), B (b) and Cr (c)] powders milled for different time periods.

Figure 3.18 and Figure 3.19 summarize the variation of lattice parameter of α–Fe[Si,(Al, B, Cr)] for $Fe_{75}Si_{20}M_5$ and $Fe_{75}Si_{15}M_{10}$ powders, respectively, as a function of milling time period. In order to enable comparison of the lattice parameter variation in the ternary system with the parent (Fe-Si) system, the variation of $Fe_{75}Si_{25}$ lattice parameter is also shown in the figure. The ratio between the lattice parameter of the as-milled and as-mixed powders is shown in the right hand axis of the figure. The lattice parameter of $Fe_{75}Si_{20}Al_5$, $Fe_{75}Si_{20}B_5$, and $Fe_{75}Si_{20}Cr_5$ decreased from 0.2866 nm to nearly stable values of 0.2857 nm, 0.2857 nm and 0.2856 nm, respectively, after 80 hours of milling. Substitution of Al and B in Fe-Si resulted in a gradual decrease in the value of lattice parameter which ultimately attained the above mentioned value which is 0.3% lower than the initial value. But, Cr substituted samples showed a drastic reduction in the lattice parameter up to 20 hours, quite similar to the parent ($Fe_{75}Si_{25}$) system, followed by a gradual change for higher milling time, and ultimately registered a maximum change of 0.35 % after 80 hours of milling. This indicates the occurrence of atomic disorder during the milling process. Since the atomic radius of Si (0.118 nm) is smaller than Fe (0.123 nm), substitutional dissolution of Si in Fe matrix results in a decrease in lattice parameter. However, the atomic radius of Al (0.142 nm) and Cr (0.128 nm) are higher than that of Fe and therefore substitutional dissolution of Al or Cr should compensate the decrease in lattice parameter due to Si dissolution in Fe matrix by increasing the lattice parameter. Further, higher atomic radius of Al as compared to Cr can result in more compensation due to dissolution of Al as compared to Cr. This may be the reason for the minimal change in the lattice parameter of Al substituted samples as compared to Cr substituted samples. It is also interesting to observe large compensation of lattice parameter in B

substituted samples. This might be due to the different dissolution behavior of Si and B in Fe matrix. Earlier studies [40] on $Fe_{80}Si_7B_{13}$ system suggest that only 75% of Si and 35% of B can dissolve into Fe. The degree of dissolution of Si and B was quantitatively calculated from the decrease of lattice parameters due to the substitution of elements [40] and by comparing the lattice parameter decrement with the lattice parameter of binary alloys. Following the procedures of Perez *et al.* [40], a quantitative analysis of our results suggests that only 70 % (72%) of Si and 32 % (35%) B of for $Fe_{75}Si_{20}B_5$ ($Fe_{75}Si_{15}B_{10}$) might have dissolved into Fe in the currently investigated sample, which is in good agreement with the previous report.

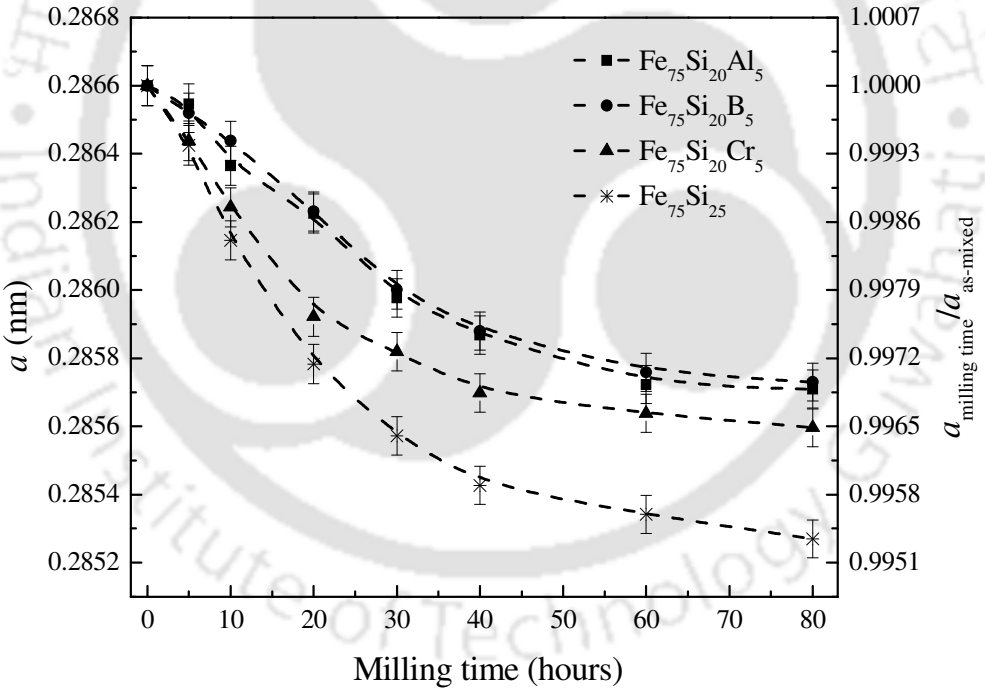

Figure 3.18: Variation of lattice parameter (*a*) of $Fe_{75}Si_{20}M_5$ [M = Al, B and Cr] powders as a function of milling time. Ratio of the lattice parameter of the as-milled and as-mixed powder samples is shown in the right hand axis.

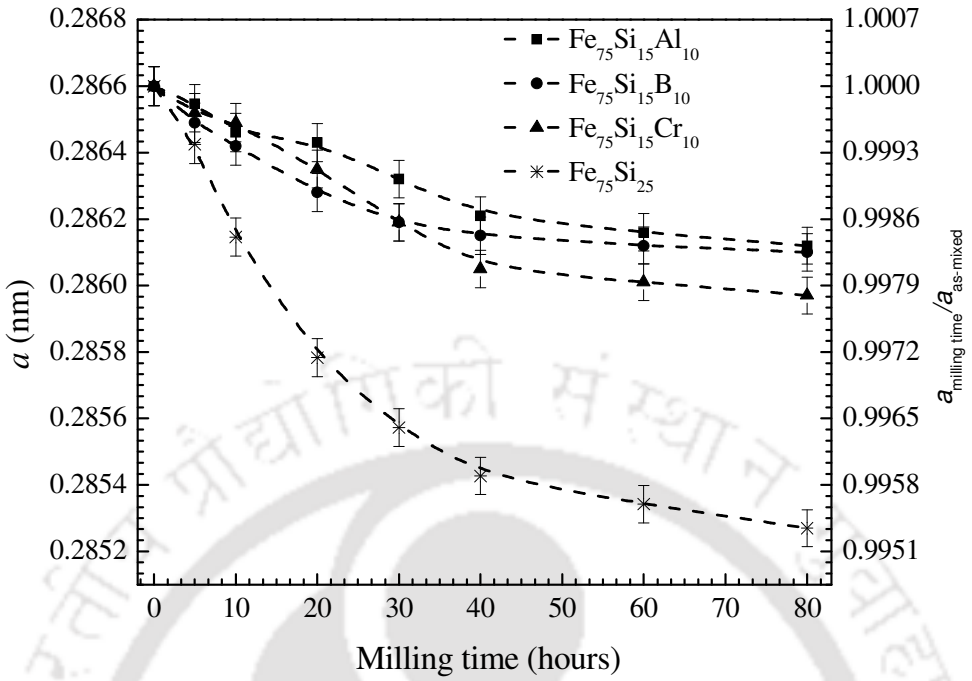

Figure 3.19: Variation of lattice parameter (*a*) of $Fe_{75}Si_{15}M_{10}$ [M = Al, B, Cr] powders as a function of milling time. Ratio of the lattice parameter of the as-milled and as-mixed powder samples is shown in the right hand axis.

The average crystallite size and the dislocation density of Fe-Si-M (M=Al, B ,Cr) powders were calculated as a function of milling time using modified Williamson-Hall method as discussed earlier in case of $Fe_{75}Si_{25}$ powders. Figure 3.20 and Figure 3.21 show the variation of average crystallite size and average dislocation density of $Fe_{75}Si_{20}M_5$ and $Fe_{75}Si_{15}M_{10}$ powders, respectively. The average crystallite size decreased linearly up to 40 hours of milling and then attained a nearly constant value, while the average dislocation density increased with increasing milling time and ultimately showed a tendency to saturate at higher milling time periods. This analysis reveals that 80 hours milled samples contain the dislocation density of about 10^{18} m^{-2}, i.e., at least one or two dislocations per square nm area.

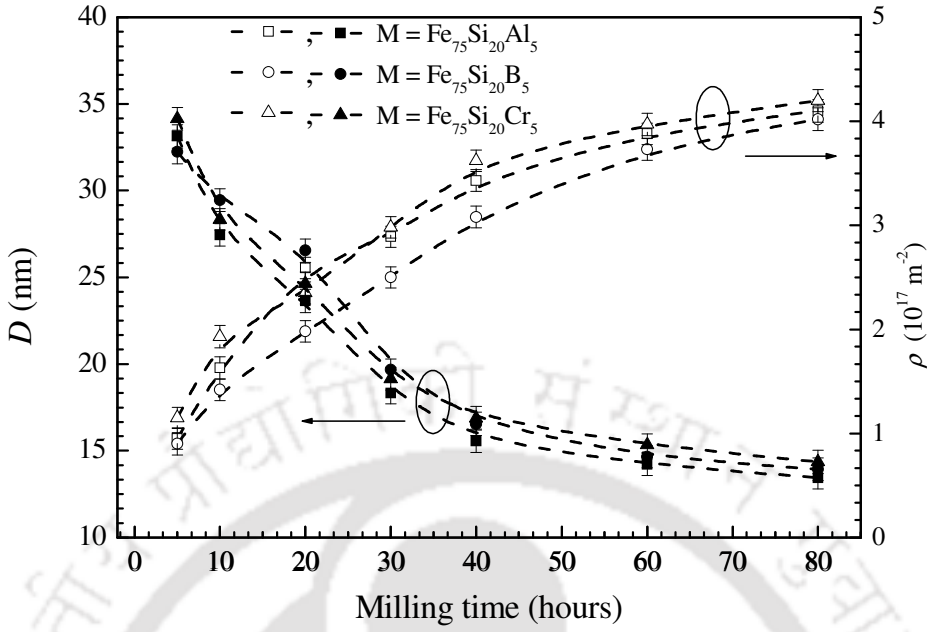

Figure 3.20: Variation of average crystallite size and average dislocation density of $Fe_{75}Si_{20}M_5$ [M = Al, B, Cr] powders with increasing milling time periods.

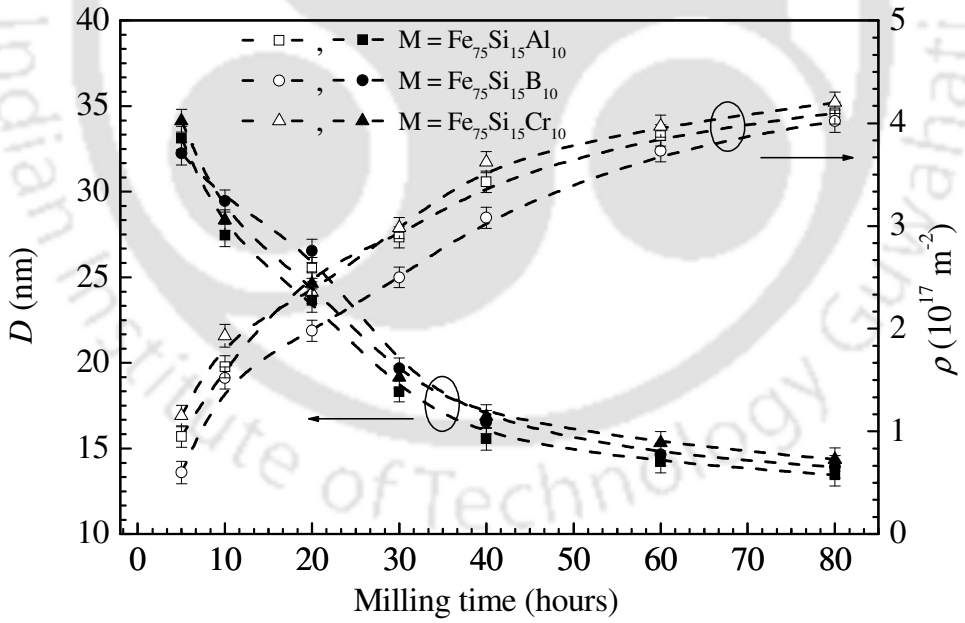

Figure 3.21: Variation of average crystallite size (D) and average dislocation density (ρ) of $Fe_{75}Si_{15}M_{10}$ [M = Al, B, Cr] powders with increasing milling time periods.

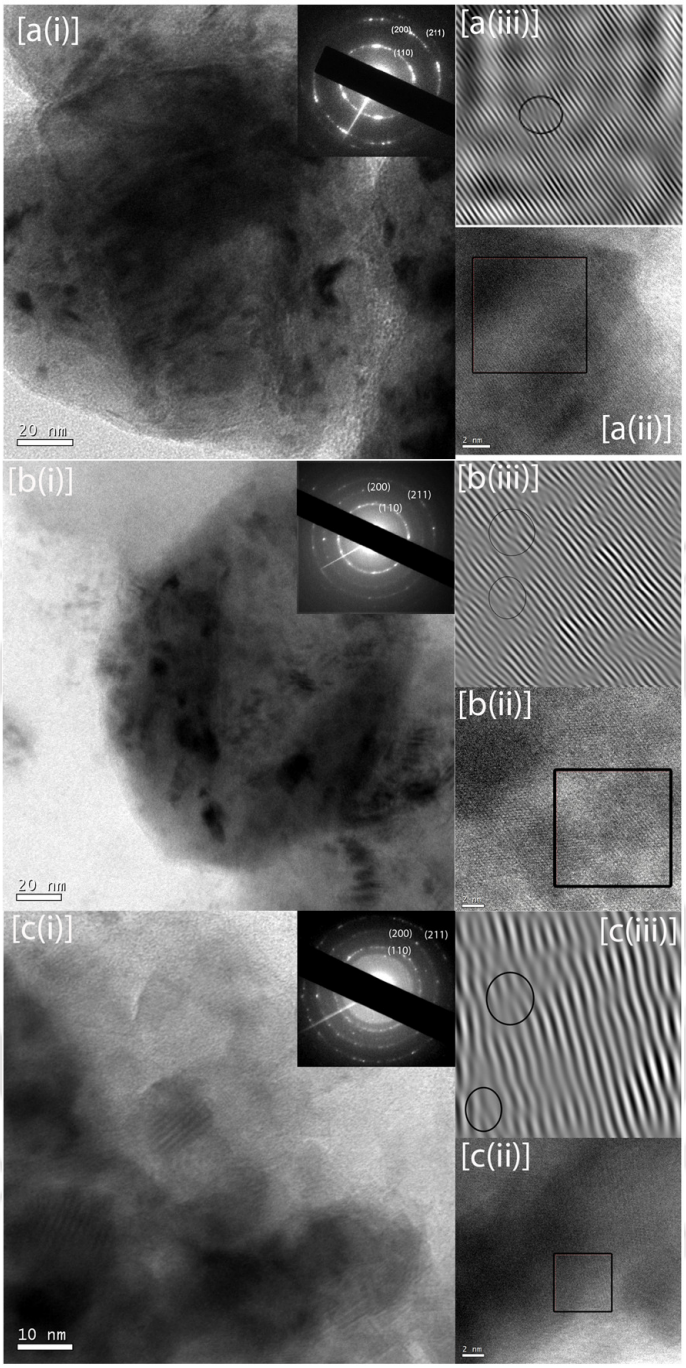

Figure 3.22: (i) BF-TEM images and SAED patterns, (ii) HRTEM images, and (iii) i-FFT images of selected area of HRTEM images (highlighted by square box) of $Fe_{75}Si_{20}M_5$ [M = Al (a), B (b), Cr (c)] powders milled for 80 hours.

In order to understand the development of nanocrystalline structure and to analyze the existence of defects in the nanostructure, we carried out TEM observations on the 80 hours milled powders. Figure 3.22 shows the bright field TEM (BF-TEM) images, selected area electron diffraction (SAED) patterns, high resolution TEM (HRTEM) images and inverse-Fast Fourier Transform (i-FFT) images of selected area of HRTEM images of $Fe_{75}Si_{20}M_5$ (M = Al, B, Cr) powders milled for 80 hours. SAED patterns show the polycrystalline nature of the powders with the rings corresponding to reflections from (110), (200) and (211) planes of Fe. The *d*-spacing and lattice parameter were calculated from the diffraction pattern for the 80 hours milled samples. These results agree well with the values obtained from XRD peak analysis. HRTEM images also support the presence of fine nanometer sized crystallites with high degree of strain. The i-FFT images of the selected area of the HRTEM images show the presence of dislocations, which are highlighted by circle(s) in each image. These results indicate that a highly strained and defective nanostructure has been formed after 80 hours of milling in the investigated samples.

3.3.2. Evolution of magnetic properties of during milling

Figures 3.23 (a) – (c) and 3.24 (a) – (c) show the room temperature $M - H$ loops of $Fe_{75}Si_{20}M_5$ and $Fe_{75}Si_{15}M_{10}$ powders milled for various time periods. Figure 3.25 and 3.26 shows the variation of coercivity and average magnetic moment (μ) per iron atom of $Fe_{75}Si_{20}M_5$ and $Fe_{75}Si_{15}M_{10}$ powders, respectively, as a function of milling time periods. In case of $Fe_{75}Si_{20}M_5$ powders, the average magnetic moment decreases from $2.0\mu_B$ to about $1.6\mu_B$ for both Al and B substituted samples, while the Cr substituted samples show

larger decrease ($1.74\mu_B$ to $1.1\mu_B$) for powders milled for 5 hours and 80 hours, respectively. This variation in magnetization follows the similar trend exhibited by the lattice parameter variation as a function of milling time, as shown in Figure 3.18 and Figure 3.19. The decrease in the average magnetic moment with increasing milling time can be attributed partial filling of the Fe 3*d* bands with 3*p* electrons of Fe as a result of the substitution of Si, Al, Cr and B in Fe-Si-M (M = Al, B, Cr) powders, respectively [35,53]. In addition, considerable amount of Fe atoms is expected to be present in the grain boundaries. So, the inter-atomic distance between Fe neighbors varies spatially [54, 55], which can contribute to the lowering of saturation magnetization of the powders. On the other hand, the coercivity of the powder increases with increasing milling time periods.

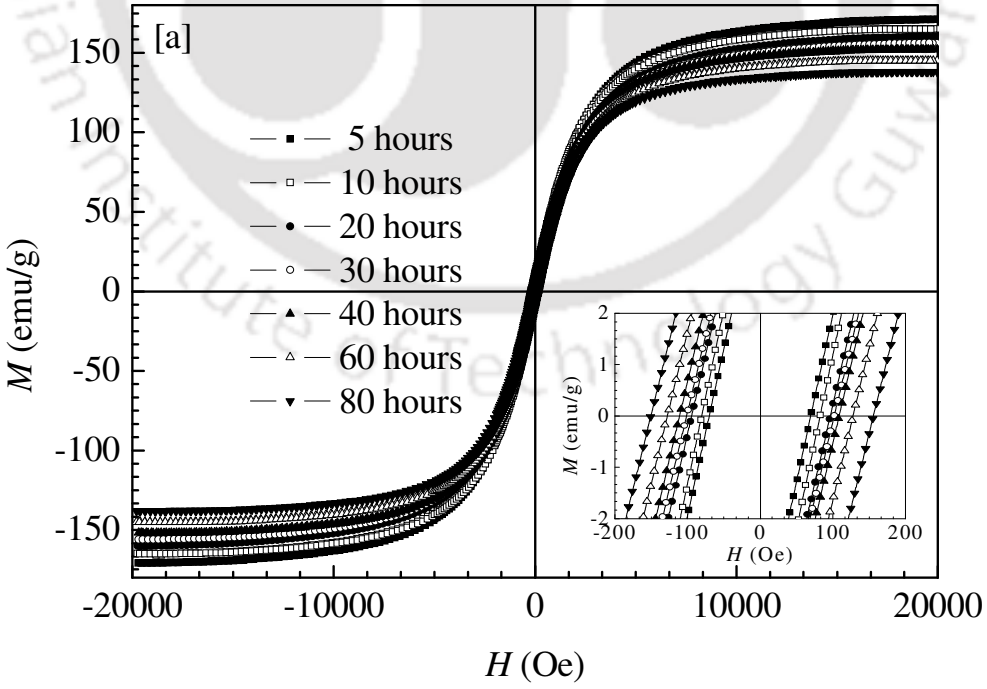

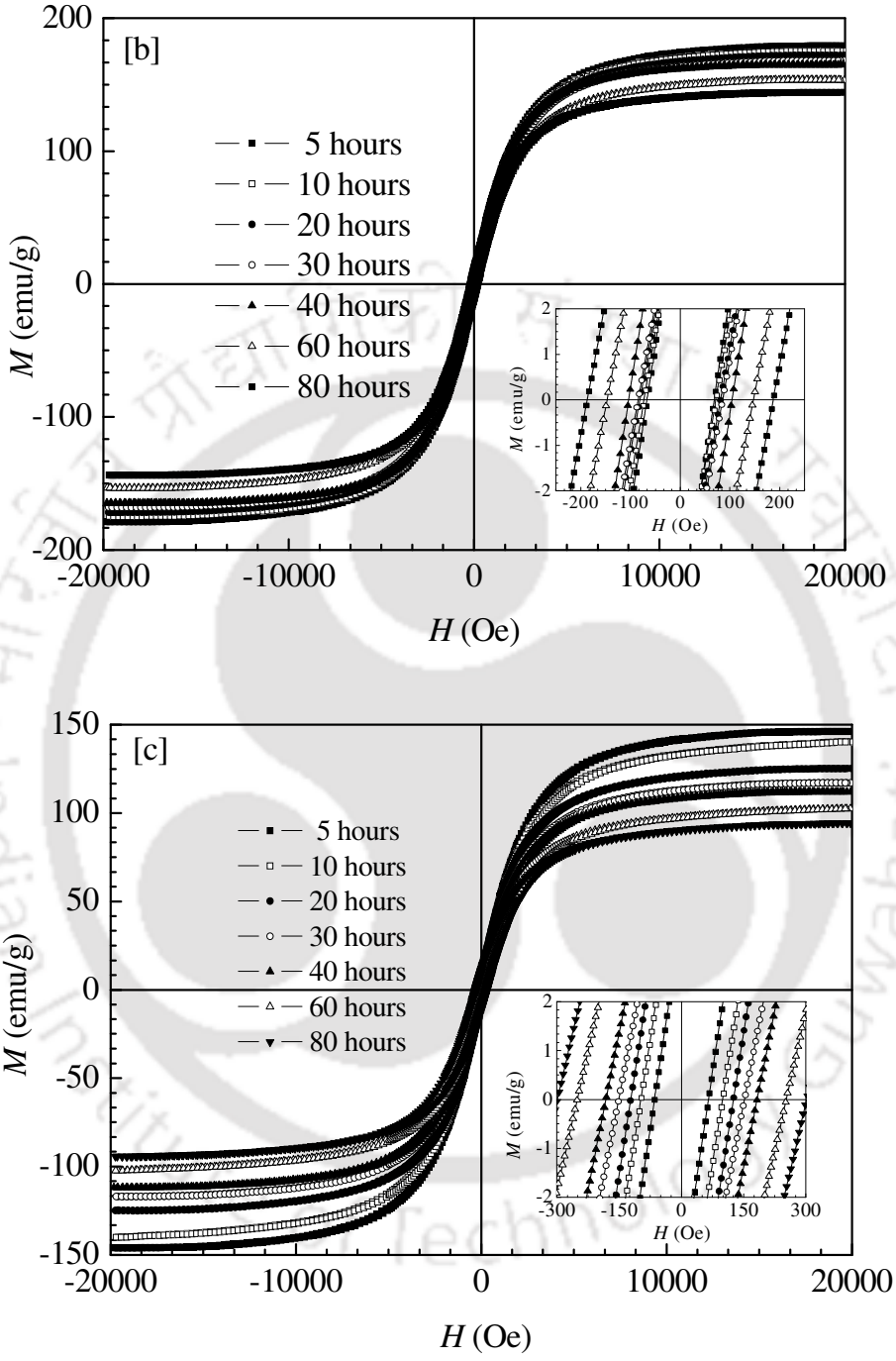

Figure 3.23: Room temperature $M - H$ loops of $Fe_{75}Si_{20}M_5$ [M = Al (a), B (b), Cr (c)] powders milled for various time periods. Inset shows the expanded view of the $M - H$ loops near the origin.

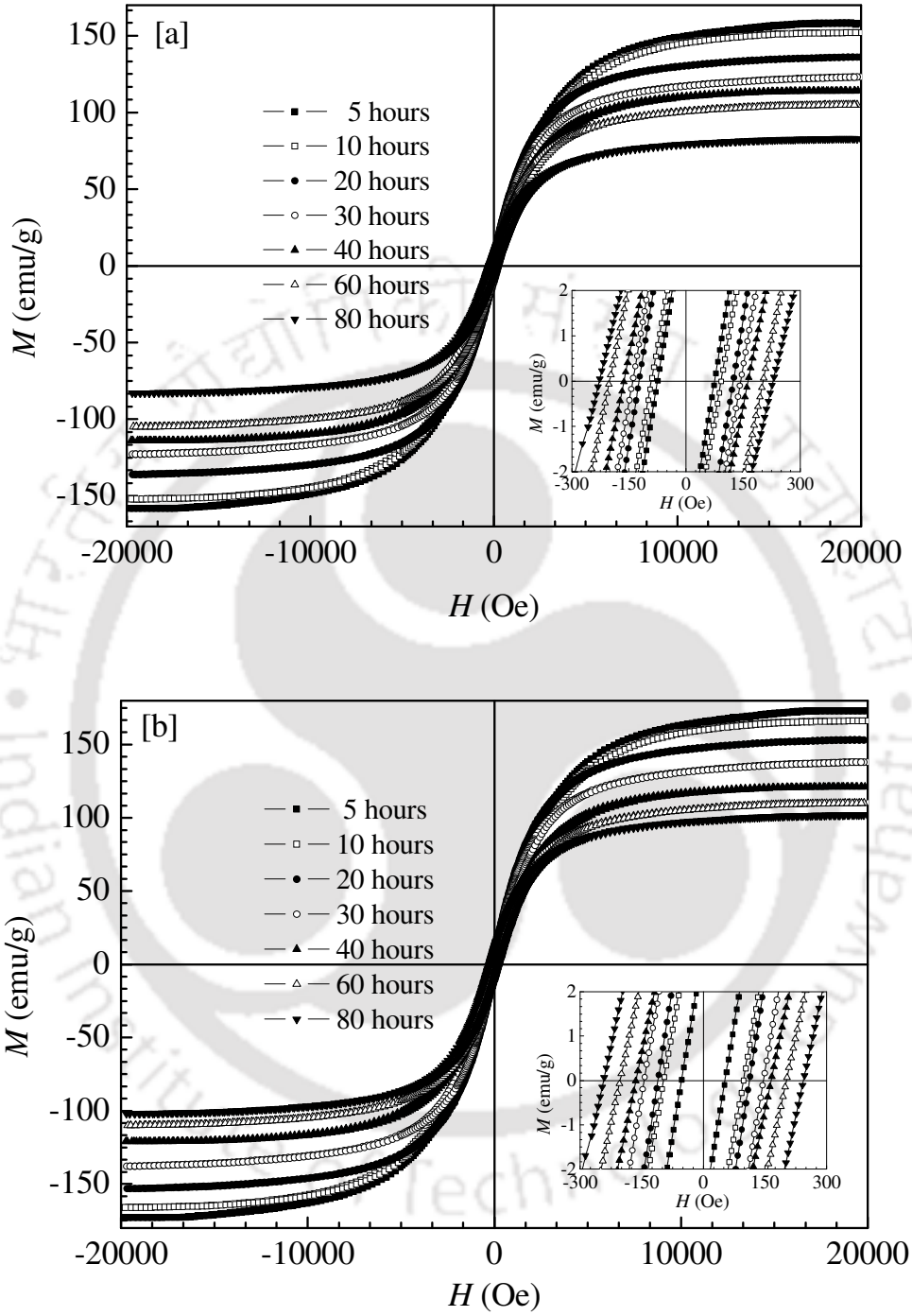

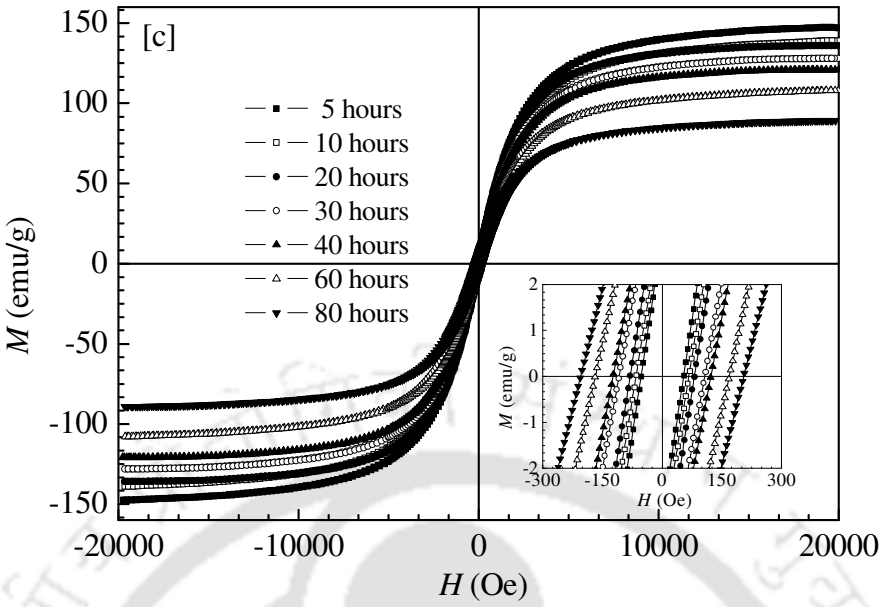

Figure 3.24: Room temperature $M - H$ loops of $Fe_{75}Si_{15}M_{10}$ [M = Al (a), B (b), Cr (c)] powders milled for various time periods. Inset shows the expanded view of the $M - H$ loops near the origin.

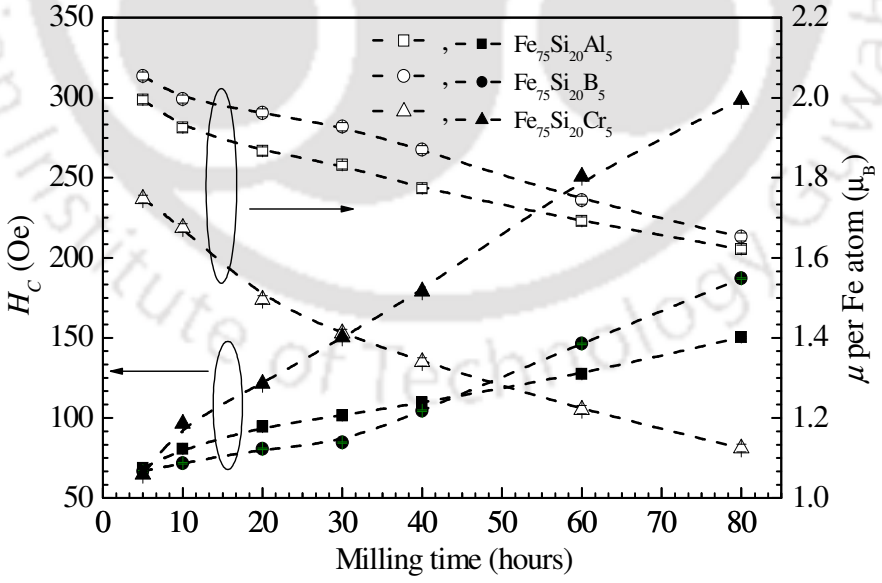

Figure 3.25: Variation of coercivity (H_C) and average magnetic moment (μ) per Fe atom of $Fe_{75}Si_{20}M_5$ [M = Al, B, Cr] powders as a function of milling time periods.

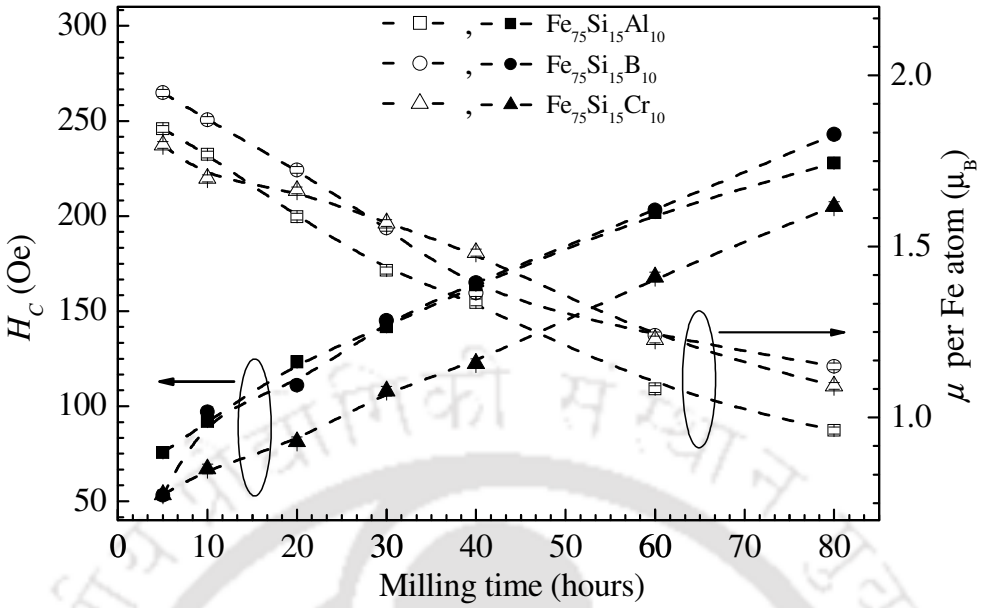

Figure 3.26: Variation of coercivity (H_C) and average magnetic moment (μ) per Fe atom of $Fe_{75}Si_{15}M_{10}$ [M = Al, B, Cr] powders as a function of milling time periods.

In order to understand the various contributions qualitatively, coercivity (H_C) has been plotted as a function of dislocation density in Figure 3.27 (a) and Figure 3.28 (a) for $Fe_{75}Si_{20}M_5$ and $Fe_{75}Si_{15}M_{10}$ powders, respectively. It could be seen from figure 3.27 (a) and 3.28 (a) that the variation of coercivity with dislocation density shows a nearly linear behavior initially, followed by a rapid deviation from the linear behavior for higher dislocation densities. A linear behavior as observed in Figure 3.27 (a) and Figure 3.28 (a) as expected from Neel's theory has been observed for powders milled for lower milling time periods. However, for longer milling times (i.e. beyond 40 hours), coercivity deviates from the linear behavior. In order to study the possible effect of particle size on coercivity, coercivity has been ploted against $d^{-3/2}$ as shown in Figure 3.27 (b) and 3.28 (b) for $Fe_{75}Si_{20}M_5$ and $Fe_{75}Si_{15}M_{10}$ powders respectively. A nearly linear behavior indicates that particle size may also affect coercivity of the powders. This contribution to

coercivity is especially prominent in powders milled for longer (greater than 40 hours in these cases) time periods.

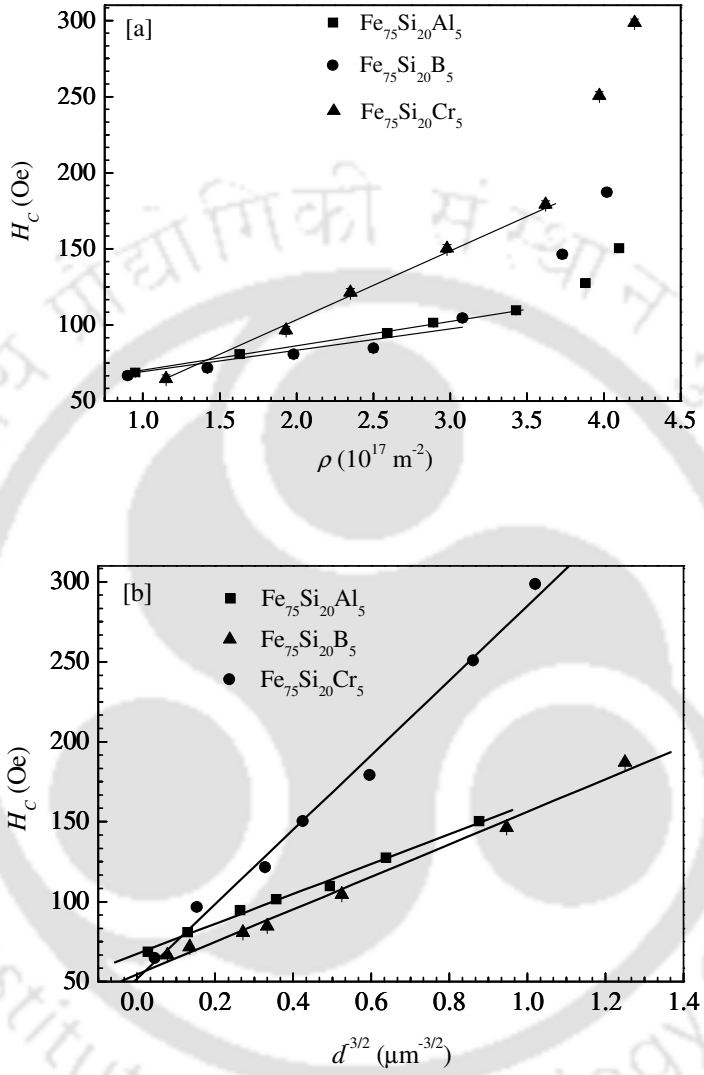

Figure 3.27: [a] Variation of coercivity of $Fe_{75}Si_{20}M_5$ [M = Al, B and Cr] powders as a function of dislocation density. The solid lines in the figure merely highlight the linearity of the data. [b] Plot of coercivity of $Fe_{75}Si_{20}M_5$ [M = Al, B, Cr] powders versus $d^{-3/2}$. The solid lines represent the least squares fit to the data.

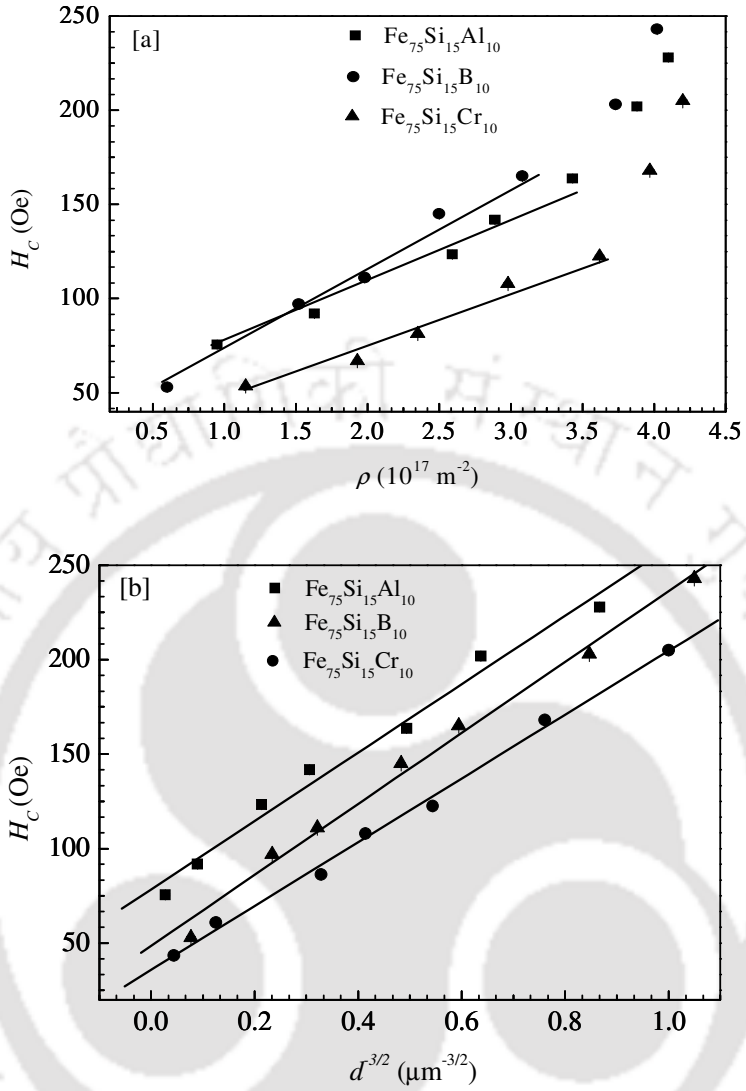

Figure 3.28: [a] Variation of coercivity of $Fe_{75}Si_{15}M_{10}$ [M = Al, B, Cr] powders as a function of dislocation density. The solid lines in the figure merely highlight the linearity of the data. [b] Plot of coercivity of $Fe_{75}Si_{15}M_{10}$ [M = Al, B, Cr] powders versus $d^{-3/2}$. The solid lines represent the least squares fit to the data.

The effective magnetic anisotropy of the powders has been calculated from the initial magnetization curves using the law of approach to saturation as discussed earlier in case of $Fe_{75}Si_{25}$ powders. Figure 3.29 and Figure 3.30 depict the variation of effective

anisotropy constant of $Fe_{75}Si_{20}M_5$ and $Fe_{75}Si_{15}M_{10}$ powders, respectively, with milling time periods. The values of K_{eff} are of the order of 10^5 Jm^{-3}, which are higher than that of bulk Fe (4.8×10^4 Jm^{-3}). The high values of K_{eff} can be due to the large strain induced during the milling process [26, 61] and also due to the small size of the particles. A good correspondence between coercivity and effective anisotropy has been observed in the present studies (*cf.* Figure 3.25 and Figure 3.26).

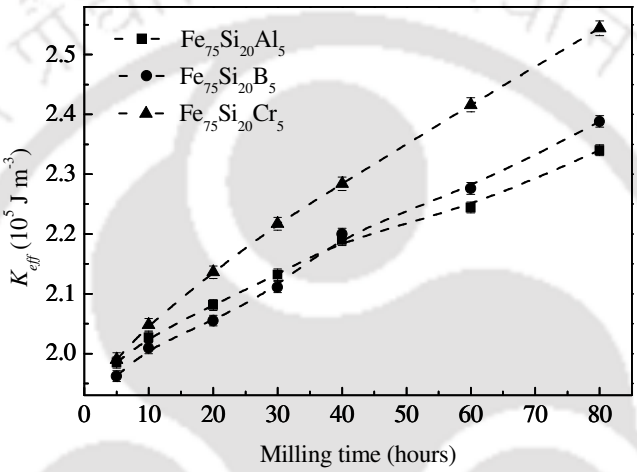

Figure 3.29: Variation of effective magnetic anisotropy of $Fe_{75}Si_{20}M_5$ [M = Al, B, Cr] powders with milling time period.

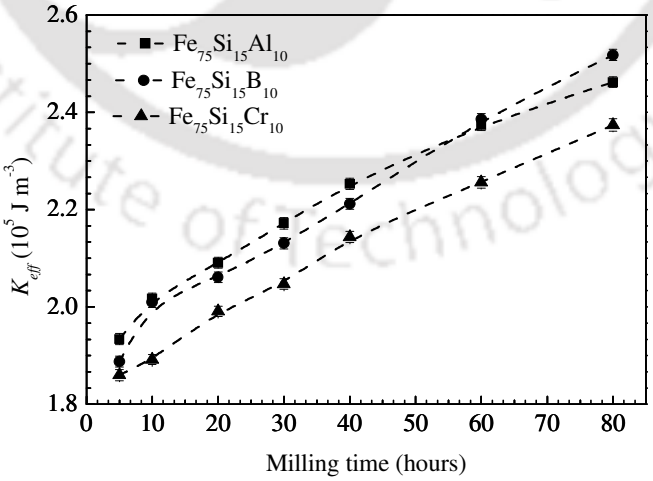

Figure 3.30: Variation of K_{eff} of $Fe_{75}Si_{15}M_{10}$ (M=Al, B, Cr) powders with milling time period.

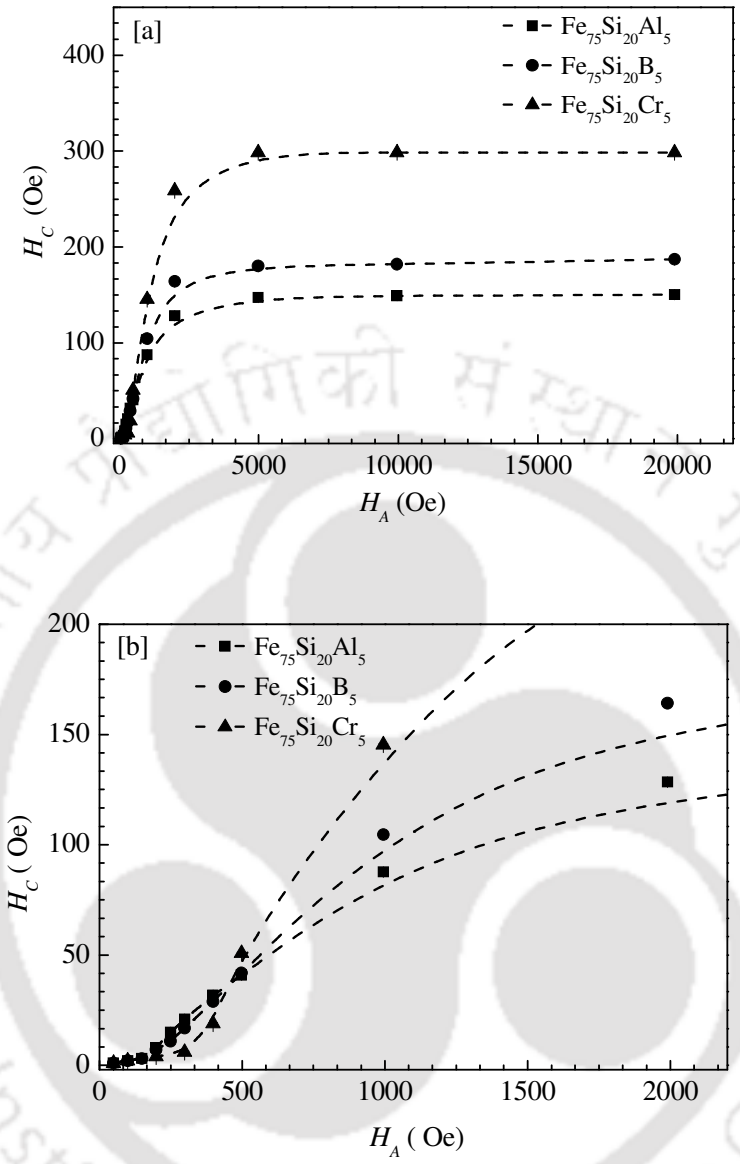

Figure 3.31: [a] Dependence of minor hysteresis loop coercivities on applied field of $Fe_{75}Si_{20}M_5$ [M = Al, B, Cr] powders. [b]The data close to the origin is shown in expanded scale.

The possibility of domain wall pinning at the grain boundaries and dislocations was investigated by analyzing the coercivities of different minor $M - H$ loops of thermally demagnetized 80 hours milled powders of all three different compositions.

Figure 3.31 (a) and Figure 3.32 (a) show the variation of coercivity obtained from various minor $M - H$ loops, measured with different maximum magnetic fields of $Fe_{75}Si_{20}M_5$ and $Fe_{75}Si_{15}M_{10}$ powders, respectively. Coercivity increases slowly [Figure 3.31 (b) and Figure 3.32 (b)] for lower applied fields and then abruptly attains saturation value at higher applied fields. The low-field behavior is an indication of domain wall pinning due to dislocations and grain boundaries [62,63]. This argument is supported by the XRD and TEM results discussed earlier.

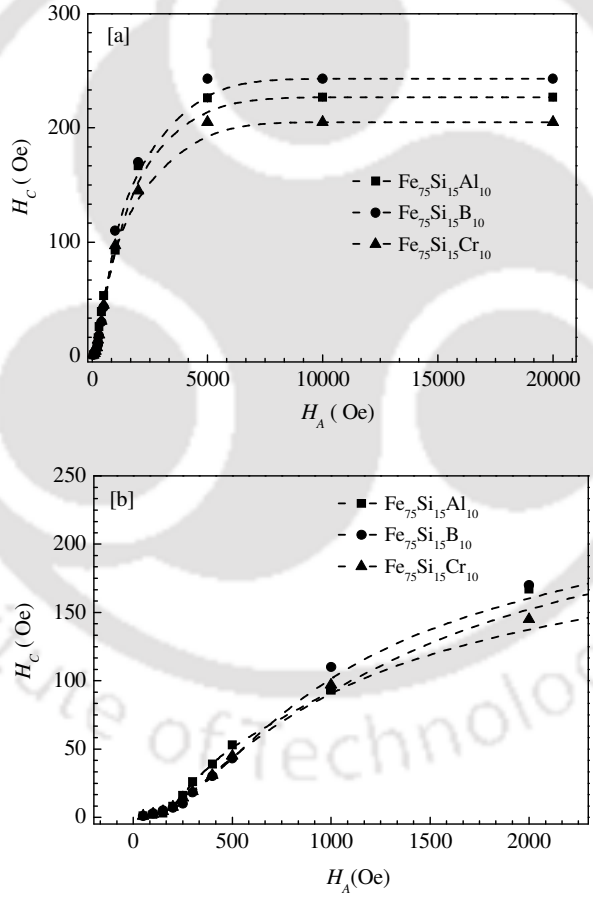

Figure 3.32: [a] Dependence of minor hysteresis loop coercivities on applied field of $Fe_{75}Si_{15}M_{10}$ (M=Al, B, Cr)powders. [b] The data close to the origin is shown in expanded scale.

Figure 3.33 and Figure 3.34 show the $M - T$ plots of 80 hours milled $Fe_{75}Si_{20}M_5$ and $Fe_{75}Si_{15}M_{10}$ powders, respectively, recorded at an applied magnetic field of 100 Oe. The Curie temperatures (T_C) were obtained by Curie-Weiss law. T_C values of 979 K, 983 K and 1021 K have been obtained for $Fe_{75}Si_{20}Al_5$, $Fe_{75}Si_{20}B_5$ and $Fe_{75}Si_{20}Cr_5$ powders, respectively. For $Fe_{75}Si_{20}Al_{10}$, $Fe_{75}Si_{20}B_{10}$ and $Fe_{75}Si_{20}Cr_{10}$ powders T_C values of 983 K, 1012 K and 1022 K have been obtained, respectively. These values are lower than that of pure Fe which is 1043 K. The lower values of T_C of the powders may be related to the dissolution of Si and Al, B or Cr in Fe matrix during milling. However, the high strains induced during milling can also influence T_C of the powders as already pointed out in case of $Fe_{75}Si_{25}$ powders.

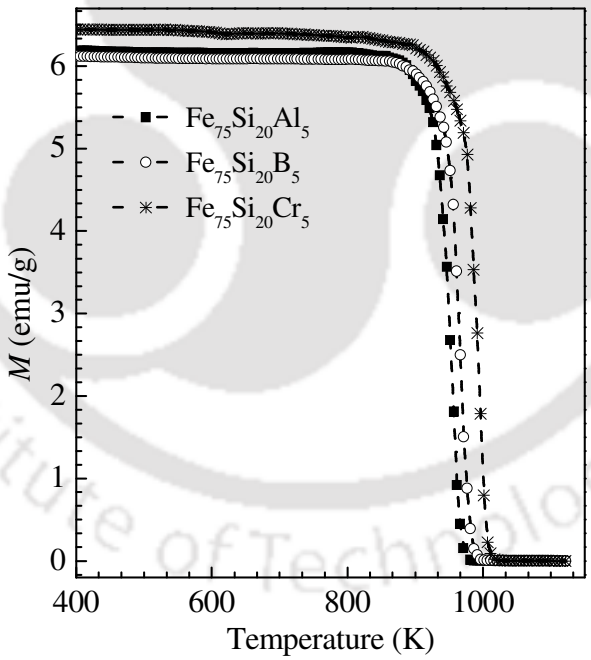

Figure 3.33: $M - T$ plots of 80 hours milled $Fe_{75}Si_{20}M_5$ [M = Al, B, Cr] powders. All M-T plots were recorded under an applied field of 100 Oe.

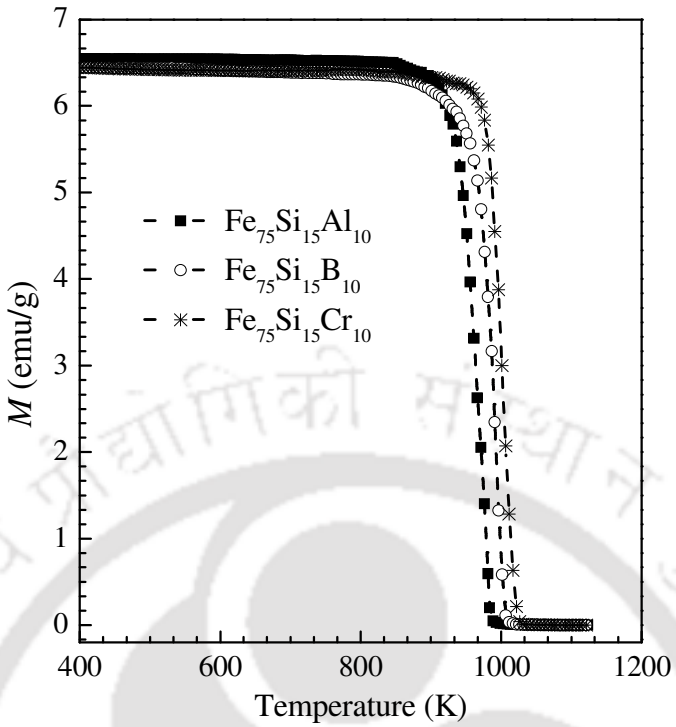

Figure 3.34: $M - T$ plots of 80 hours milled $Fe_{75}Si_{15}M_{10}$ [M = Al, B, Cr] powders. All M-T plots were recorded under an applied field of 100 Oe.

3.4. Comparison of the properties of Fe-Si and Fe-Si-M powders

The manners in which the nanocrystalline structure evolves and alloying occurs in Fe-Si and Fe-Si-M powders have been found to be almost similar. MA produced non-equilibrium solid solutions α-Fe (Si) for Fe-Si and α-Fe(Si,M) for Fe-Si-M powders. The lattice parameters attain nearly stable values after 40 hours of milling indicating the completion of the alloying process at this stage of milling. However, the variation of lattice parameter with increasing milling times has been found to be different for different alloy compositions. Strong dependencies on the size and amount of different elements present in the alloys are observed. The average crystallite size decreased below 15 nm after 40 hours of milling. Large amounts of dislocation defects are induced during the

milling process which shows a tendency to saturate at higher milling times. The magnetic moments of various powders have been found to depend on the alloy compositions with $Fe_{75}Si_{25}$ ($Fe_{75}Si_{15}Cr_{10}$) showing the highest (lowest) value. The variation of coercivity with increasing milling time periods have been found to be similar. Coercivity increases with increasing milling time periods in all the alloy compositions. Although, the correlation of structure and magnetic properties are similar, the structural and magnetic parameters strongly depend on the specific alloy composition. The values of coercivity and saturation magnetization of the 80 hours milled powders of the Fe-Si and Fe-Si-M powders are listed in Table 3.2.

Table 3.2: Coercivity and saturation magnetization of 80 hours milled Fe-Si and Fe-Si-M powders.

Alloy Composition	**Coercivity** H_C **(Oe)**	**Saturation Magnetization** M_S **(emu/g)**
$Fe_{75}Si_{25}$	128	149
$Fe_{75}Si_{20}Al_5$	150	138
$Fe_{75}Si_{15}Al_{10}$	227	82
$Fe_{75}Si_{20}B_5$	187	144
$Fe_{75}Si_{15}B_{10}$	243	102
$Fe_{75}Si_{20}Cr_5$	298	94
$Fe_{75}Si_{15}Cr_{10}$	205	89

3.5. Summary

A systematic study on the evolution of structure and magnetic properties of Fe-Si and Fe-Si-M (M = Al, B, Cr) powders during the course of milling has been carried out. Evolution of nanostructure during milling and the corresponding changes in the magnetic properties of the powders have been studied. Mechanical alloying produced non-equilibrium solid solutions α–Fe(Si) in case of $Fe_{75}Si_{25}$ and α–Fe[Si,(Al, B, Cr)] in case of $Fe_{75}Si_{20}M_5$ and $Fe_{75}Si_{15}M_{10}$ powders with crystallites of nanometer size and dislocation density of the order of about 10^{18} m^{-2}. Occurrence of atomic disorder during the milling process was evident from the changes in the lattice parameter and saturation magnetization values. The observed increase in coercivity with increasing milling time periods could be attributed to the introduction of high dislocation densities and reduction of powder particle size during milling. Presence of dislocations introduced during the MA process and the grain boundaries increases the possibility of domain wall pinning. Strains induced during milling may also have affected the Curie temperature of the powders. Though similar co-relation between structure and magnetic properties has been observed in powders of all the alloy compositions, the structural and magnetic parameters have been found to be strongly dependent on the alloy compositions.

Chapter 4

Effect of heat treatment on the properties of milled powders

It is well known [45] that appropriate heat treatment at elevated temperatures can reduce the high coercivity and dislocation density of the as-milled samples. Moreover, high temperature heat treatment can also induce structural changes in the powders. Hence, heat treatment of the as-milled powders at different temperatures and time periods provides a means to improve the soft magnetic properties of these powders as well as to understand the equilibrium structure of these powders at these elevated temperatures. In this chapter the effect of heat treatment at elevated temperatures (annealing) on the structure and properties of the as-milled powders of Fe-Si and Fe-Si-M is presented.

4.1. Experimental details

The systematic studies performed on the milling characteristics of $Fe_{75}Si_{25}$, $Fe_{75}Si_{20}M_5$ and $Fe_{75}Si_{15}M_{10}$ (M = Al, B, Cr) reported in the previous chapter show that alloying of Fe, Si and M is nearly complete after 40 hours of milling as indicated by nearly stable

values of lattice parameter. Further, in all the alloy compositions, crystallite size below 15 nm could be obtained after 40 hours of milling. Therefore, for the study of effect of annealing on milled powders, various powder mixtures in the desired composition were milled under the same conditions for 40 hours. Hardened steel vial together with 7 mm diameter hardened steel balls with powder to ball weight ratio 1:10 were taken. The planetary ball mill (Insmart, India) was operated at 300 rpm. In order to avoid excessive heating, the mill was programmed to halt for 30 minutes after every 30 minutes of operation. The powders milled for 40 hours were flame sealed in fused silica ampoules at a pressure of 10^{-4} Pa. The sealed ampoules were annealed individually in the temperature range of 573 K to 1273 K for 4 hours each. The structural characterizations of Fe-Si powders annealed at different temperatures were characterized using X-Ray diffractometer [a rotating anode based XRD (Rigaku RINT 2000) for Fe-Si powders annealed at different temperatures and a sealed X-ray tube based XRD (Bruker D8) for Fe-Si-M powders annealed at different temperatures], scanning electron microscope (SEM, Leo 1430 VP) and transmission electron microscope (TEM, JEOL 2100). Fe-Si powders were also annealed at 873 K for different time periods (1 to 24 hours) and the XRD measurements were carried out using the Bruker D8 machine. Room temperature and high temperature magnetic properties of the powders were characterized using a vibrating sample magnetometer (VSM, Lakeshore 7410).

4.2. Effect of heat treatment on the structure and magnetic properties of Fe-Si powders

4.2.1. Effect of heat treatment on structure

XRD patterns of as-milled and annealed powders of $Fe_{75}Si_{25}$ are shown in Figure 4.1(a). XRD data corresponding to the nine annealing runs are presented in the figures. In Figure 4.1(b), the XRD patterns in the 2θ range of 42° to 48° are shown. Absence of Si reflections in the as-milled powders indicates the formation of non-equilibrium solid solution α-Fe(Si) as discussed in chapter 3.

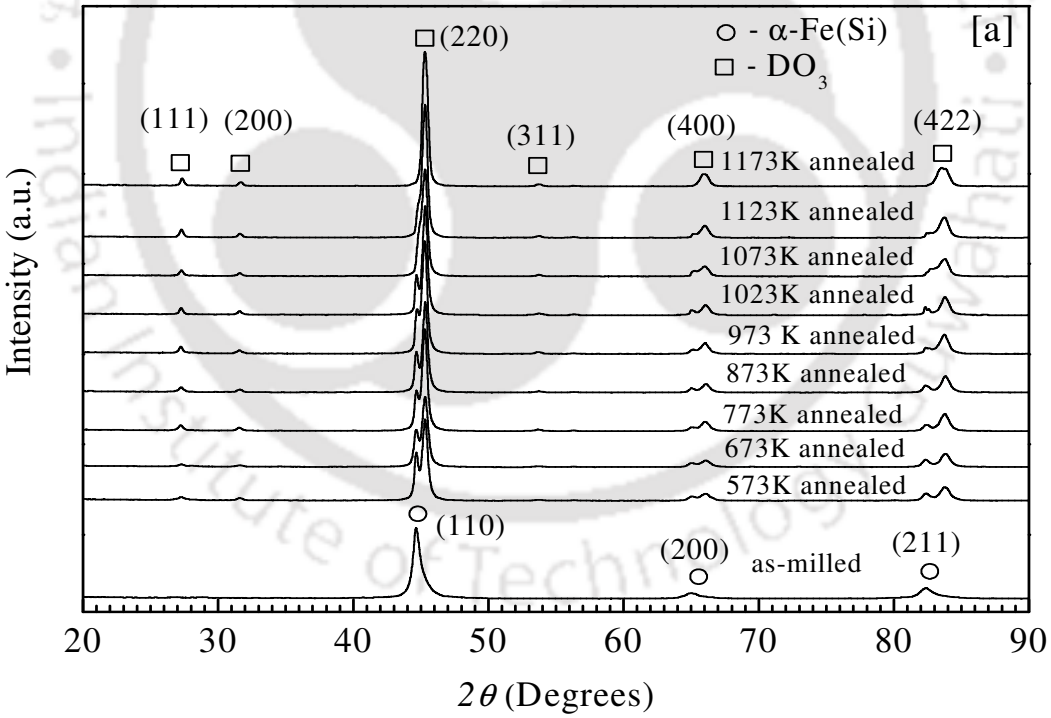

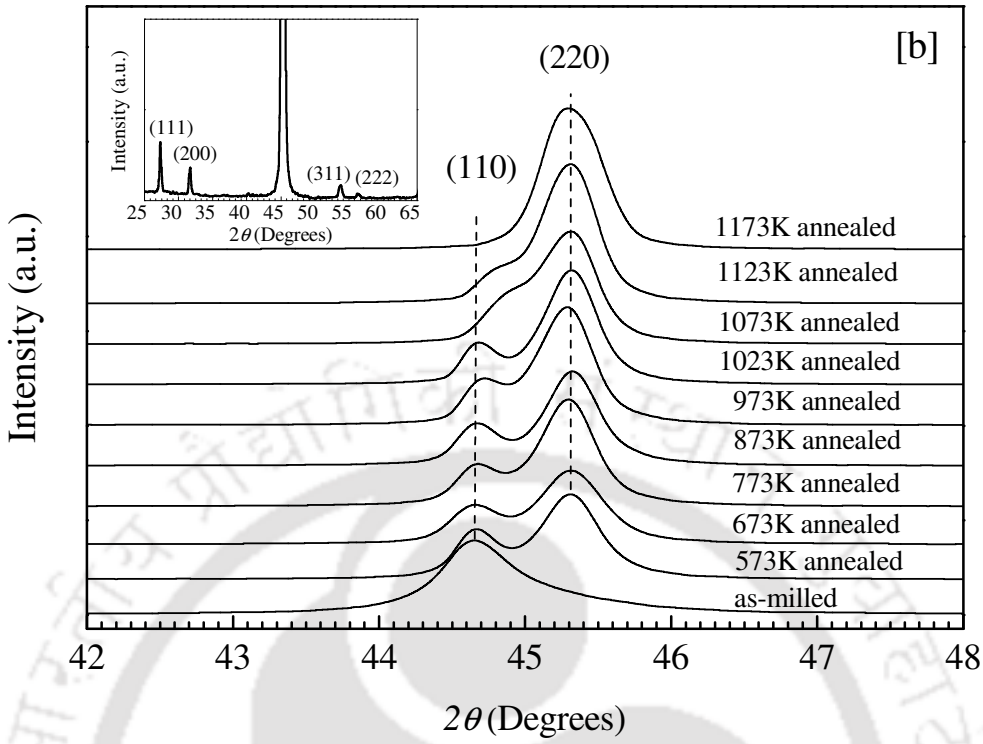

Figure 4.1: (a) XRD patterns (a) of as-milled and annealed $Fe_{75}Si_{25}$ powders. (b) Data in 2θ range of 42^{o} to 48^{o} is shown in expanded scale. Inset in Figure 4.1(b) shows the superlattice reflections of the powders annealed at 1173 K in expanded scale.

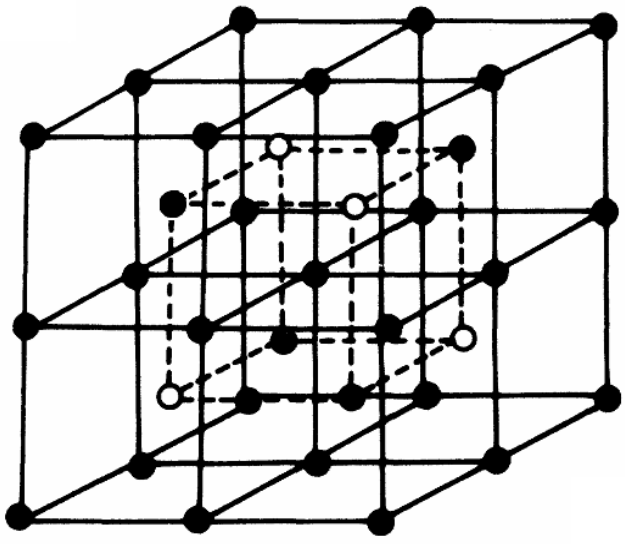

Figure 4.2: DO_3 unit cell. The solid circles are Fe sites while the open circles are Si sites of DO_3 structured Fe_3Si.

However, a gradual transition of the disordered α-Fe(Si) phase of the as-milled powders to a ordered DO_3 phase can been observed from the XRD patterns with increasing annealing temperatures. In the inset of Figure 4.1(b), the superlattice reflections of the powders annealed at 1173 K have been shown in expanded scale. In disordered α-Fe(Si), Fe-sites of the body centered cubic unit cell of α-Fe is randomly occupied by Si atoms and the symmetry of α-Fe persists. So, the Bragg reflections of α-Fe(Si) are observed close to those of α-Fe. In the case of ordered DO_3 phase, Si atoms occupy preferred sites of α-Fe and the symmetry changes to face centered cubic structure [66] (*cf.* Figure 4.2). The present study reveals that both ordered and disordered phases can co-exist in Fe-Si alloys and atomic ordering takes place gradually in these alloys. Earlier reports [41, 67] on Fe-Si powders have shown the transformation of the disordered phase of as-milled powders to superlattice DO_3 phase after annealing. However, in our concern, the gradual transition of the disordered α-Fe(Si) to the ordered DO_3 phase has been experimentally observed for the first time.

The degree of ordering achieved during the heat treatment has been quantified by evaluating the long range order (*LRO*) parameter from the intensities of a superlattice reflection and a fundamental reflection of the ordered DO_3 phase. The *LRO* parameter is defined as [68]

$$LRO = \left[\frac{I_s / I_s^o}{I_f / I_f^o} \right]^{1/2} \tag{5.1}$$

where I_s and I_f are the intensities of the fundamental and superlattice reflections, respectively, while I_o^s and I_o^f correspond to the intensities of the same reflections for a fully ordered alloy. The *LRO* parameter has been calculated for the powders annealed at

different annealing temperatures using the prominent superlattice (111) and fundamental (220) reflections. The variation of *LRO* parameter with increasing annealing temperatures is depicted in Figure 4.3.

LRO parameter increases with increasing annealing temperatures and shows a tendency to saturate for higher annealing temperatures. The *LRO* parameter for the powders annealed at 1173 K has been estimated to be 0.96 which shows that a highly ordered DO_3 phase has been formed after annealing at this temperature. Here, it should be noted that for a fully ordered phase, value of *LRO* parameter is 1.

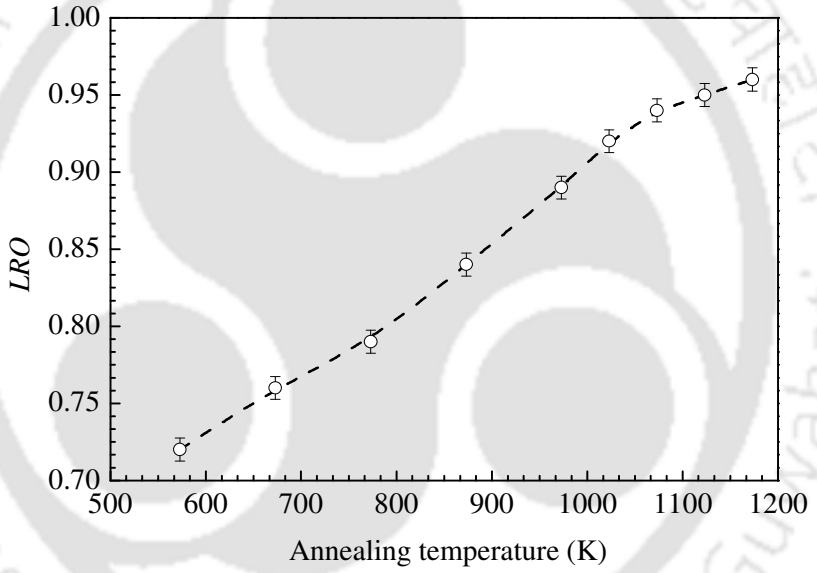

Figure 4.3: Variation of *LRO* parameter of annealed powders with annealing temperature.

The average crystallite size and average dislocation density of the disordered α-Fe(Si) and ordered DO_3 phases have been estimated from the FWHM of the XRD peaks using the modified Williamson-Hall method as discussed in Chapter 3. Figures 4.4(a), 4.4(b) and 4.4(c) illustrate the variation of average crystallite size and average dislocation density of disordered α-Fe(Si), ordered DO_3 phase and the average (averaged over

disordered and ordered phases) with increasing annealing temperatures, respectively. The average crystallite size and average dislocation density of the as-milled powders are 12 nm and 2.3×10^{17} m^{-2}, respectively. Thus, it can be inferred that mechanical alloying has produced highly refined alloy powders with large amounts of dislocation defects. A gradual increase of average crystallite size with increasing annealing temperatures is accompanied by decrease of average dislocation density. Annealing at elevated temperatures thereby induced growth of crystallite size and reduction of defects introduced in the course of the milling process.

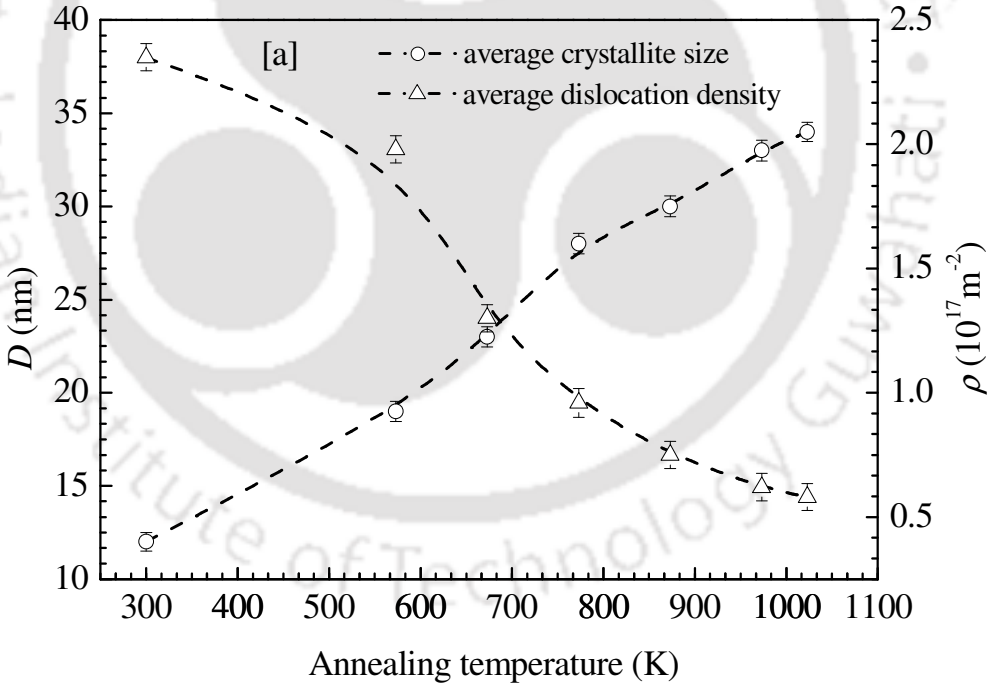

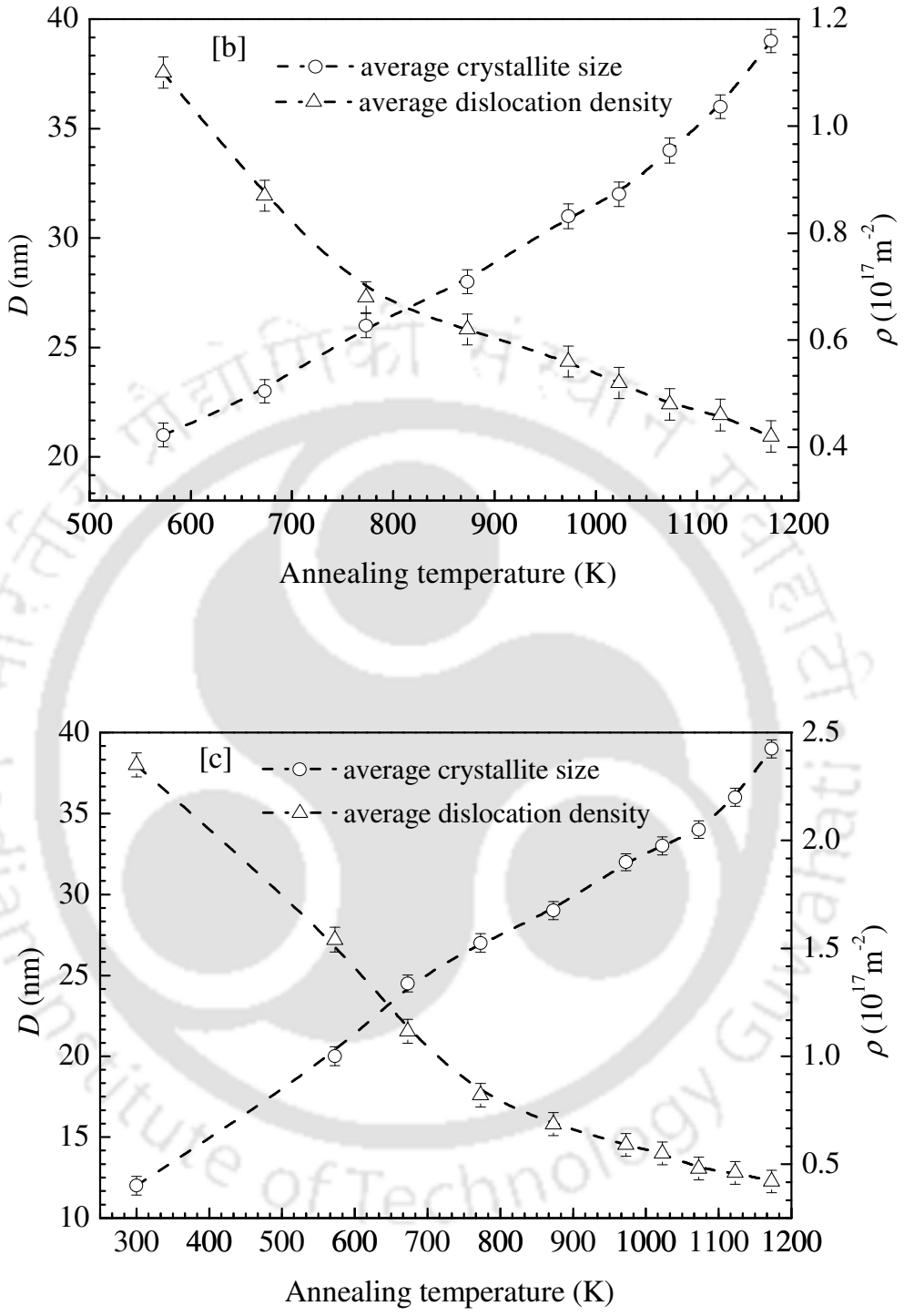

Figure 4.4: Variation of average crystallite size and average dislocation density of (a) α-Fe(Si), (b) DO_3 phase and (c) averaged values (over the disordered and ordered phases) of $Fe_{75}Si_{25}$ powders with increasing annealing temperatures.

In order to study the effect of annealing time on the structure and magnetic properties of the powders, as-milled powders sealed in fused silica ampoules were individually annealed at temperature 873 K for various time periods (*i.e.* from 1hour to 24 hours). The XRD patterns of the as-milled and powders annealed for different time periods are presented in Figure 4.5(a). In Figure 4.5(b), the XRD patterns in the 2θ range of 40^{o} to 50^{o} are shown. A transition from disordered α-Fe(Si) to ordered DO_3 phase occurs in these powders with increasing annealing time periods as evident from the Figure 4.5 (b). The superlattice reflections (111) and (200) of the powders annealed at 973 K for 18 hours are highlighted in the inset of Figure 4.5(b). A very slow scan rate of 0.005^{o} was employed in the 2θ range of 25^{o} to 35^{o} to observe the superlattice reflections.

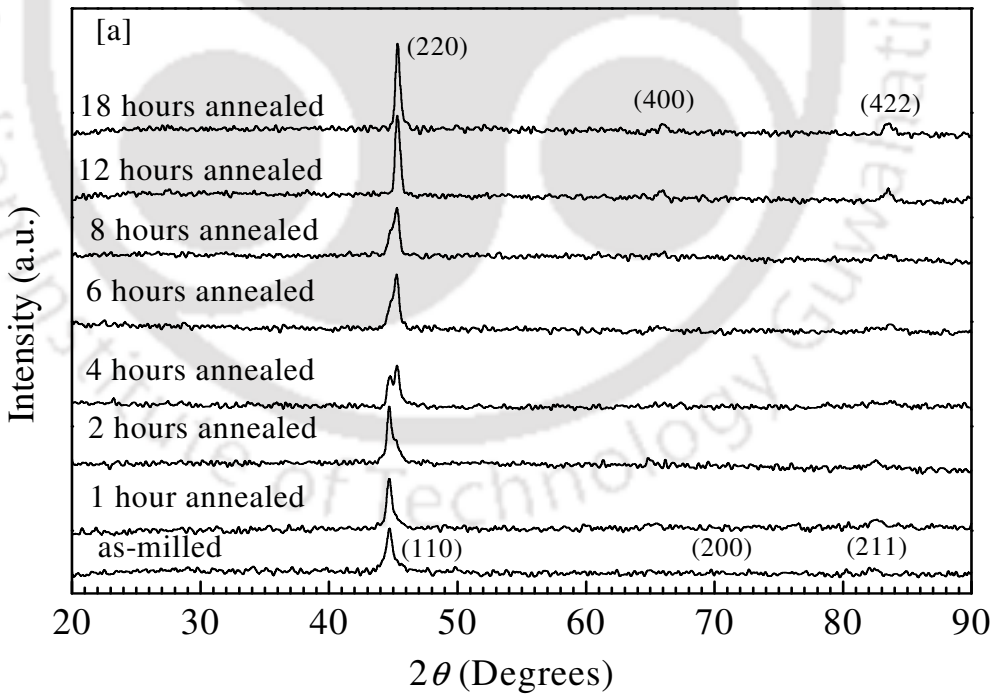

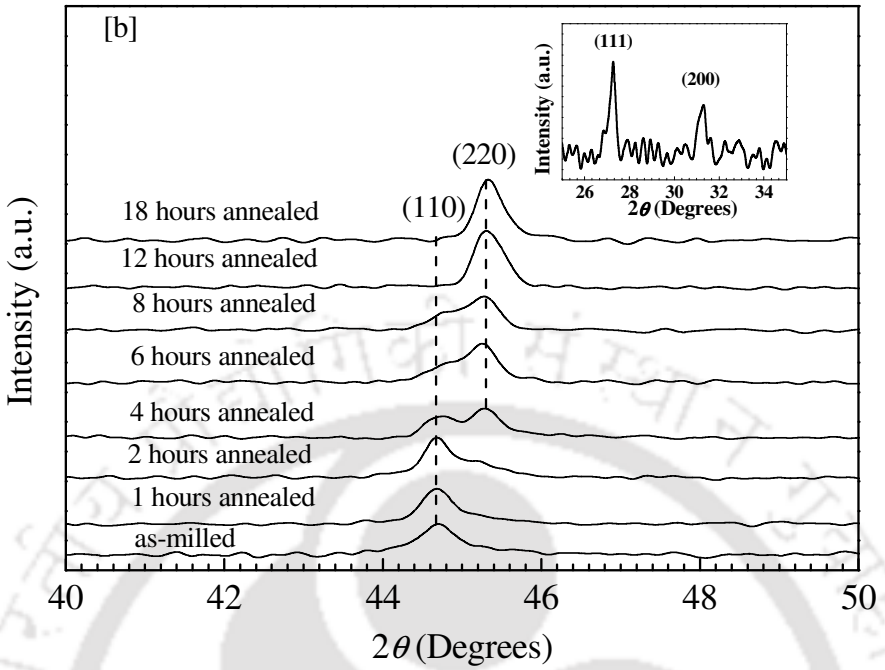

Figure 4.5: (a) XRD patterns of $Fe_{75}Si_{25}$ powders annealed for various times at 873K. (b) XRD patterns in the 2θ range of 40^{o} to 50^{o} in expanded scale. Inset of figure shows the superlattice peaks of the powders annealed at 873 K for 18 hours.

The crystallite size of the disordered and ordered phases has been calculated using Scherrer's formula [47]. Variation of crystallite size (D) averaged over those obtained for the disordered and ordered phases with increasing annealing time periods is shown in Figure 4.6. The crystallite size of the as-milled powder was estimated to be 13 nm. An increase of crystallite size has been observed with increasing annealing time. The strain contribution could not be calculated in these samples because of the low intensity of the higher angle reflections.

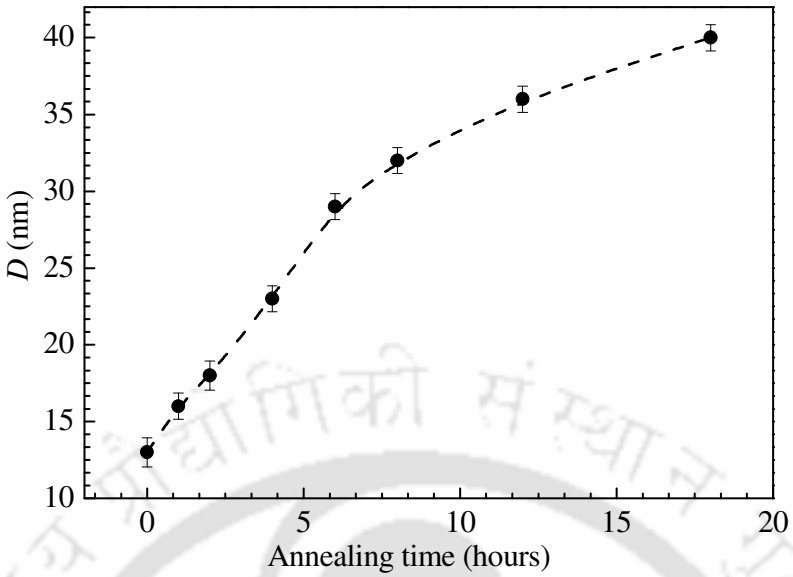

Figure 4.6: Variation of crystallite size (D) of $Fe_{75}Si_{25}$ powders annealed at 873 K for various time periods.

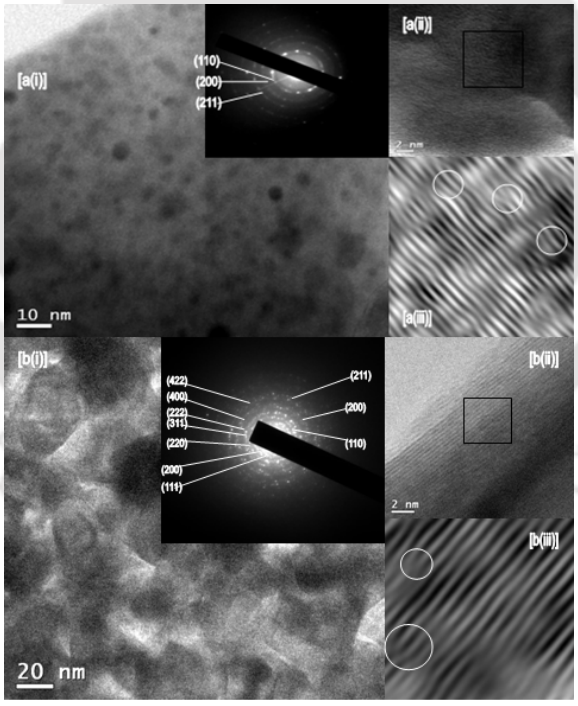

Figure 4.7: (i) BF-TEM images and SAED patterns, (ii) HRTEM images and (iii) i-FFT images of selected area of HRTEM images (highlighted by square boxes) of (a) as-milled $Fe_{75}Si_{25}$ powders and (b) $Fe_{75}Si_{25}$ powders annealed at 1073 K for 4 hours.

In order to further investigate the nanocrystalline structure and analyze the presence of defects in the powders, TEM observations were carried out in the as-milled powders and powders annealed at 1073 K. Figure 4.7 shows the bright field TEM (BF-TEM) images, selected area diffraction (SAED) patterns, high resolution TEM (HRTEM) images and inverse-fast Fourier transform (i-FFT) images of selected areas of HRTEM images of the as-milled and annealed powders. The BF-TEM image of the as-milled powders shows fine crystallites of sizes ~ 10 nm with wide grain boundaries which agrees well with the estimated value of crystallite size of 12 nm from analysis of XRD patterns. The SAED pattern show the polycrystalline nature of the as-milled powders with the ring patterns corresponding to the reflections from (110), (200) and (211) planes of α-Fe(Si). The BF-TEM image of the powders annealed at 1073 K shows crystallites sizes ~ 35 nm with reduced grain boundary regions which agrees well with the value of crystallite size of 34 nm estimated from XRD patterns. The SAED pattern of the annealed powders shows the existence of both disordered α-Fe(Si) and ordered DO_3 phases which also complements the XRD observations. The presence of defects could not be directly detected from the TEM observations. In order to analyze the existence of defects in the powders, we have carefully resolved the HRTEM images by using a GATAN digital micrograph. The i-FFT images are shown in Figure 4.7 (iii) for the as-milled and annealed powders. The i-FFT image of the selected area of HRTEM image of the as-milled powders shows the presence of large amounts of dislocations (some of the them are highlighted by circles). The i-FFT image of the selected area of HRTEM image of the annealed powder also shows the presence of some dislocations. Thus, the analysis of both

TEM and XRD observations reveal the presence of dislocations in both the as-milled and annealed powders.

4.2.2. Effect of heat treatment on magnetic properties

In order to understand the effects of annealing on the magnetic properties, room temperature magnetic hysteresis ($M - H$) loops with fields upto ± 20 kOe were obtained for the powders. Figure 4.8 shows the $M - H$ loops of the as-milled and powders annealed at different temperatures for 4 hours. Figure 4.9 shows the $M - H$ loops of $Fe_{75}Si_{25}$ powders annealed at temperature 873K for different time periods. The $M - H$ loops are typical of soft magnetic materials. The variation of coercivity (H_C) and average magnetic moment (μ) per Fe atom of $Fe_{75}Si_{25}$ powders (measured at 20 kOe) with annealing temperatures are shown in Figure 4.10. The average magnetic moment of the as-milled powders has been observed to be $1.84\mu_B$ which is lower than that that of pure α-Fe. which is about $2.1\mu_B$. The decrease of average magnetic moments can be attributed to the partial filling of 3*d* electrons of α-Fe by 3*p* electrons as a result of substitution of Fe-sites by Si atoms during the milling process [35,53]. In addition, considerable amounts of Fe atoms are expected to be present in the grain boundaries. Hence, interatomic distances of Fe atoms is expected to vary spatially [54,55] which can also contribute to the lowering of average magnetic moments of the as-milled powders. A slight decrease of average magnetic moments with increasing annealing temperatures can be related to the occurrence of atomic order [69,70].

Coercivity of the as-milled powders has been observed to be 95 Oe. The observed high coercivity of the as-milled powders is mainly attributed mainly to the high amounts

of dislocations induced during the milling process as discussed in chapter 3. A significant decrease of coercivity has been observed in the powders annealed upto 773 K. However, annealing resulted in an increase of coercivtiy in the temperature range 773 K to 1073 K followed by a decrease for the powders annealed at higher temperatures. A similar variation of change of coercivity and magnetic moments with increasing annealing time periods have been observed (*cf.* Figure 4.11) as observed with increasing annealing temperatures (*cf.* Figure 4.10).

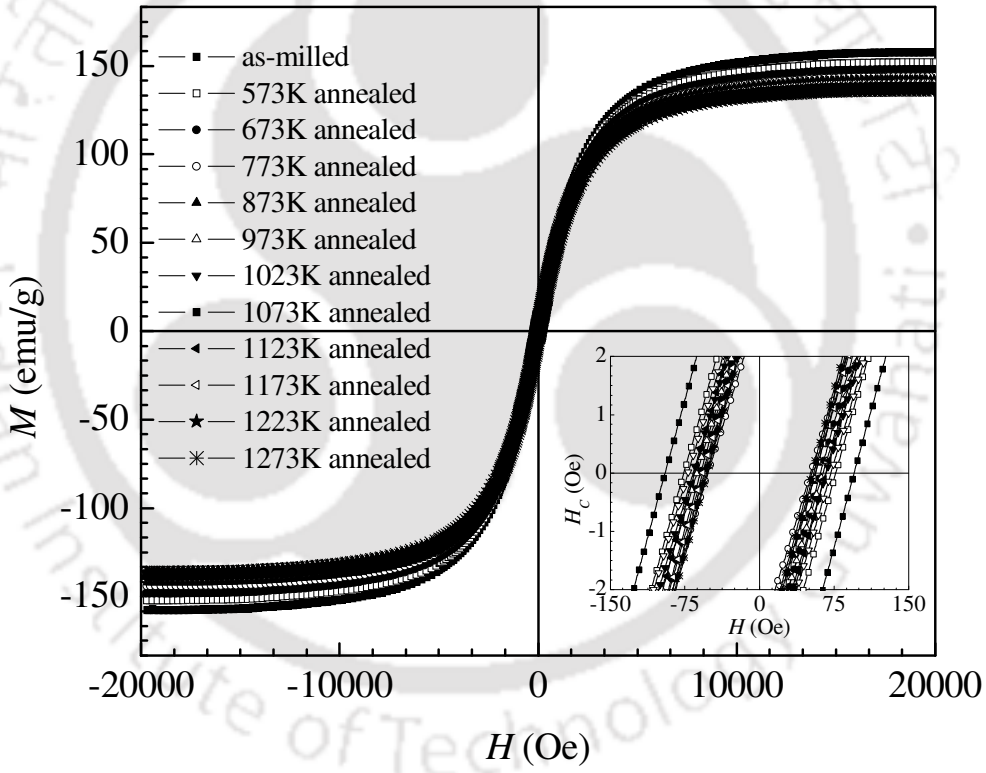

Figure 4.8: $M - H$ loops of as-milled and annealed powders of $Fe_{75}Si_{25}$. Inset: the $M - H$ curves close to the origin are shown in expanded scale.

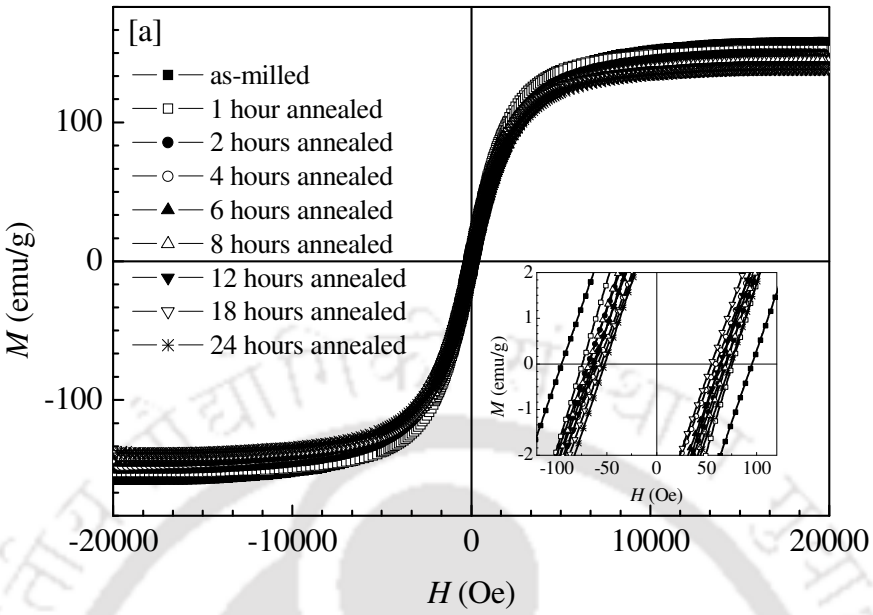

Figure 4.9: Room temperature $M - H$ loops of $Fe_{75}Si_{25}$ powders annealed at 873 K for various time periods. Inset: the $M - H$ curves close to the origin are shown in expanded scale.

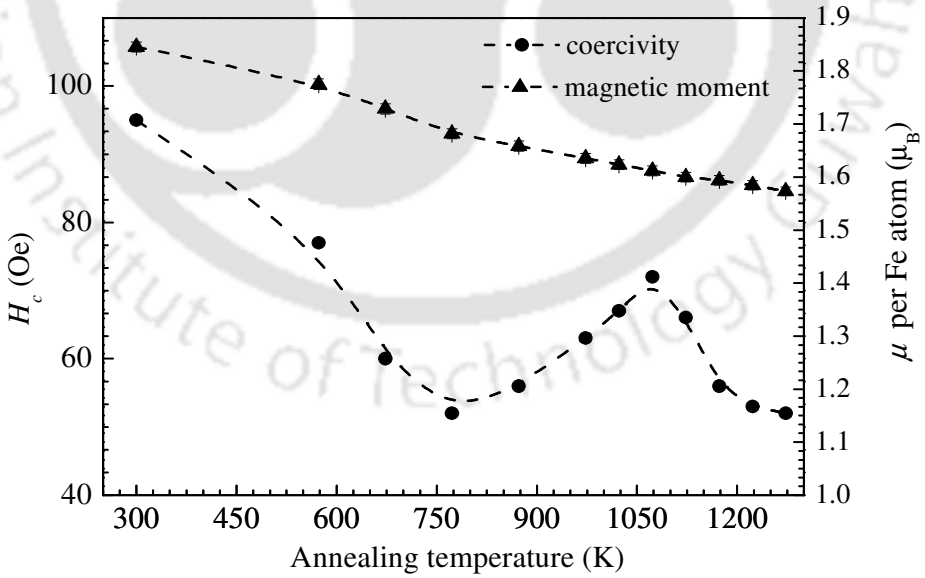

Figure 4.10: Variation of coercivity (H_c) and average magnetic moment (μ) per Fe atom of as-milled and of $Fe_{75}Si_{25}$ powders annealed at various temperatures for 4 hours.

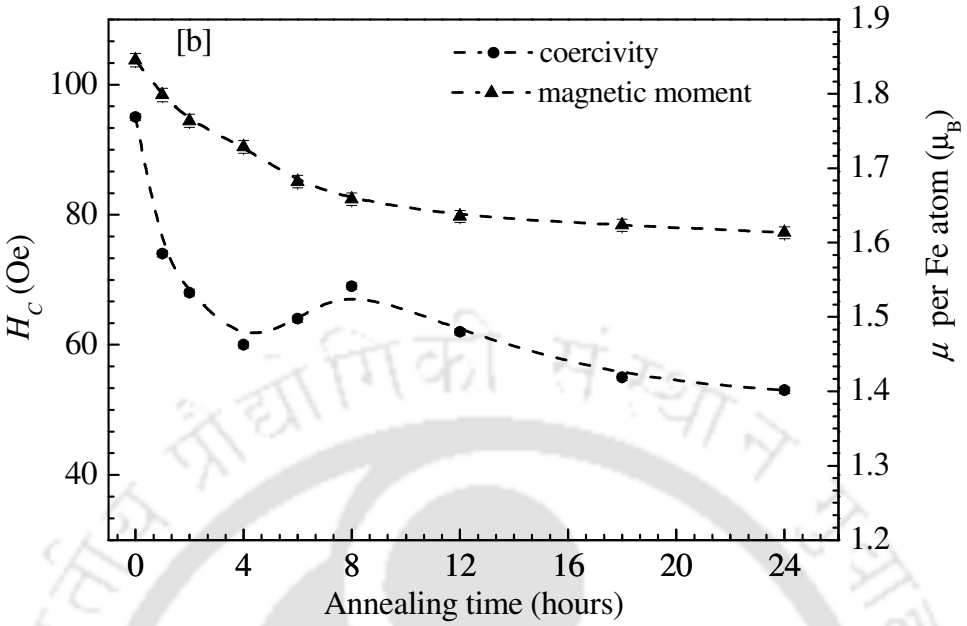

Figure 4.11: Variation of coercivity (H_c) and average magnetic moment (μ) per Fe atom of as-milled and of $Fe_{75}Si_{25}$ powders annealed at 873K for various times.

In order to understand the observed variation of coercivity with annealing temperatures, coercivity (H_C) has been plotted as a function of average dislocation density (ρ) in Figure 4.12. According to Neel's theory [56], coercivity is expected to be proportional to dislocation density when the magnetoelastic energy is higher than anisotropy energy. A nearly linear dependence of coercivity on average dislocation density for the powders annealed up to 773 K indicates that magnetoelastic energy is higher than the anisotropy energy in this annealing temperature range and coercvity is solely governed by dislocation density. However, powders annealed above 773 K, variation of coercivity deviates from the initial linear behavior indicating the effect of dislocation defects is not dominant in determining the coercivity of the powders in that annealing temperature range.

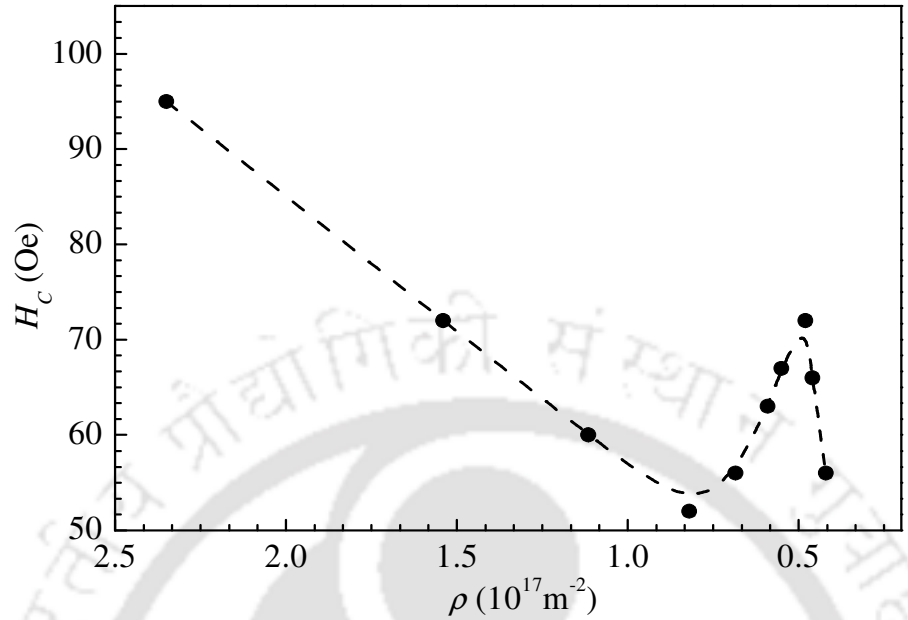

Figure 4.12: Variation of average dislocation density (ρ) with coercivity (H_C) of the as-milled and annealed powders of $Fe_{75}Si_{25}$.

Figure 4.13 (a) shows the variation of coercivity (H_C) with average crystallite size (D) for the powders annealed in the temperature range 773 K to 1173 K. Coercivity shows a maximum value of 72 Oe corresponding to the crystallite size of 34 nm as estimated from analysis of XRD results which has been confirmed by TEM observations. The increase of coercivity with increasing crystallite sizes in the annealing temperature range 773 K to 1073 K can be well explained based on the random anisotropy model (RAM) [23]. According to RAM, coercivity varies as the sixth power of crystallite size when the crystallite size is less than the ferromagnetic exchange length. The plot between coercivity and sixth power of crystallite size for the powders annealed in the temperature

range 773 K and 1073 K presented in Figure 4.13 (b) shows a linear behavior which confirms the dependency of coercivity on crystallite as predicted by RAM.

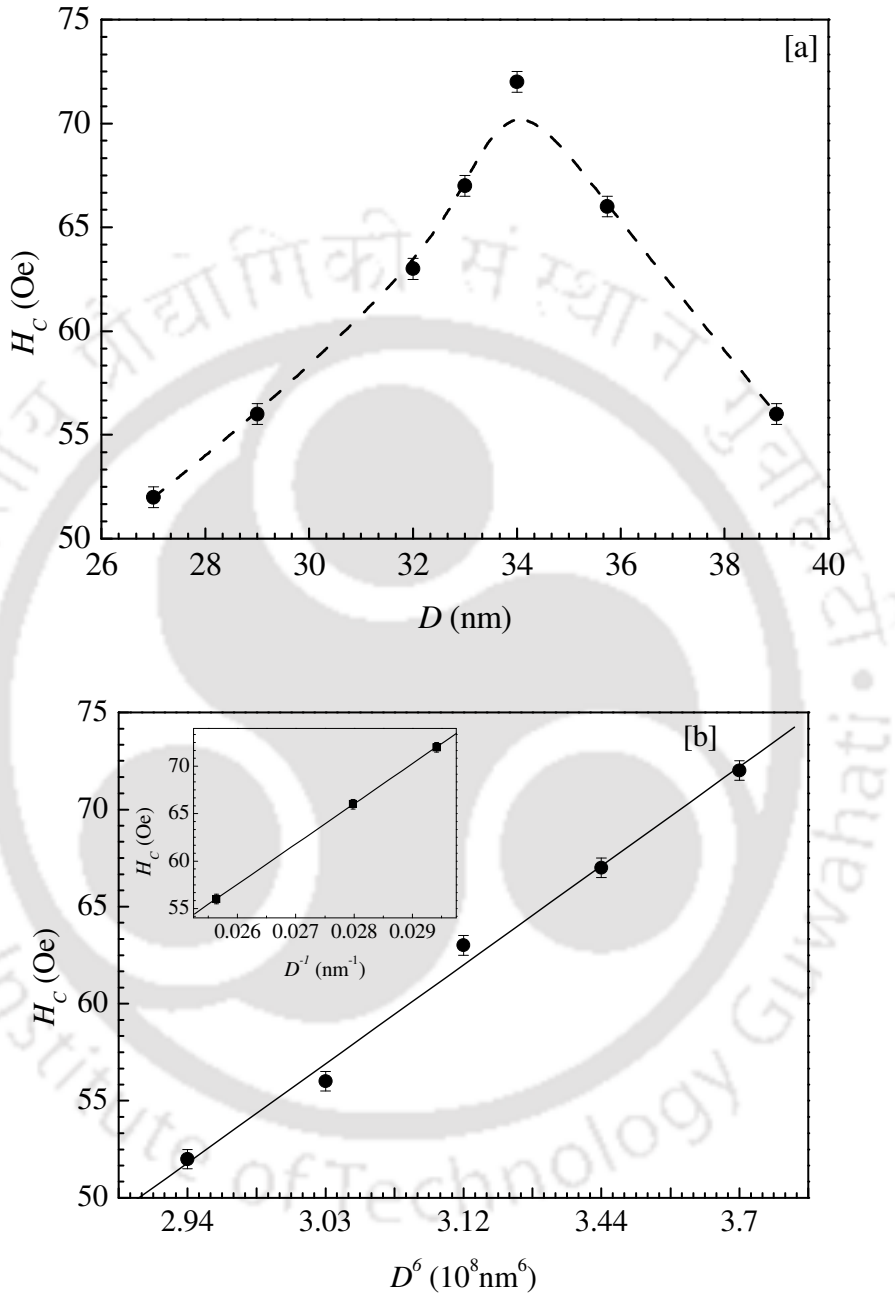

Figure 4.13: (a) Variation of (H_C) with crystallite size (D) of $Fe_{75}Si_{25}$ powders annealed in between 773 K and 1173 K. (b) Plot of H_C *versus* D^6 for annealed powders. Inset of

Figure 4.13 (b) shows the plot between H_C and D^{-1} for the powders annealed in the temperature range 1073 K to 1173 K.

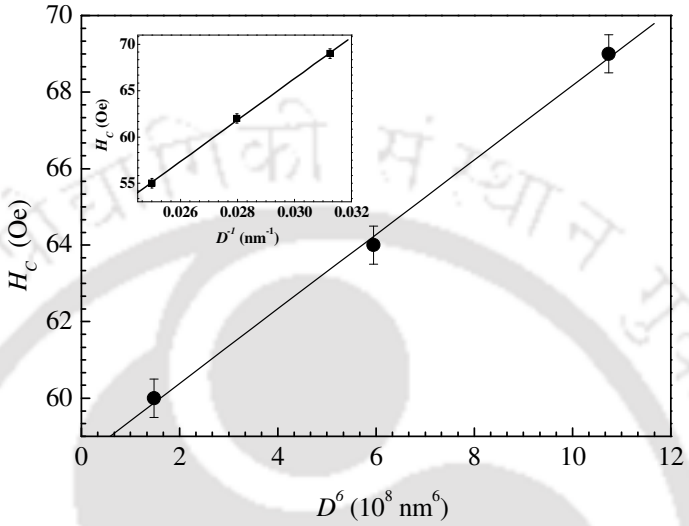

Figure 4.14: Coercivity (H_C) *versus* sixth power of crystallite size (D) of $Fe_{75}Si_{25}$ powders annealed at 873K for 4 to 8 hours where H_C increases with D. Inset: D^{-1} law for larger crystallite sizes.

For the powders annealed in the temperature range 1073 K to 1173 K, coercivity depends mainly on crystallite size according to the well known D^{-1} law for coarser grained alloys. In inset of Figure 4.13 (b), linear relationship between coercivity and D^{-1} has been shown. A change in the nature of the dependency of coervicity on crystallite size, *viz*. from D^6 to D^{-1} has been observed to occur in the powders annealed at 1073 K. The value of crystallite size for the powders annealed above 1073 K is 34 nm which is close to the ferromagnetic exchange length of Fe-Si alloys [23]. Thereby, for the powders annealed at higher temperature ranges, in which the dislocation density has been reduced

considerably, the features observed in melt-spun nannocrystalline ribbons are present. However, the value of coercivity of the powders (~52 Oe to 100 Oe) has been found to be high as compared to that of melt-spun ribbons (~ 10^{-3} Oe) [23]. XRD and TEM observations show that the dislocation defects could not be removed completely by the annealing procedure adopted in the present work. The residual defects present in the annealed powders may be mainly contributing to the high coercivity of the powders.

The effective anisotropy (K_{eff}) of the $Fe_{75}Si_{25}$ powders annealed at various temperatures for 4 hours and annealed at 873 K for various time periods was estimated using the law of approach to saturation as discussed in chapter 3. Figure 4.15 shows the variation of K_{eff} *of* the powders with increasing annealing temperatures while Figure 4.16 shows the variation of K_{eff} of powders annealed for various time periods at 873 K. Annealing has been observed to have a significant effect on the K_{eff} values which followed similar trends as has been observed for the variation of coerivity with annealing temperatures (*cf.* Figure 4.10) and annealing time (*cf.* Figure 4.11).

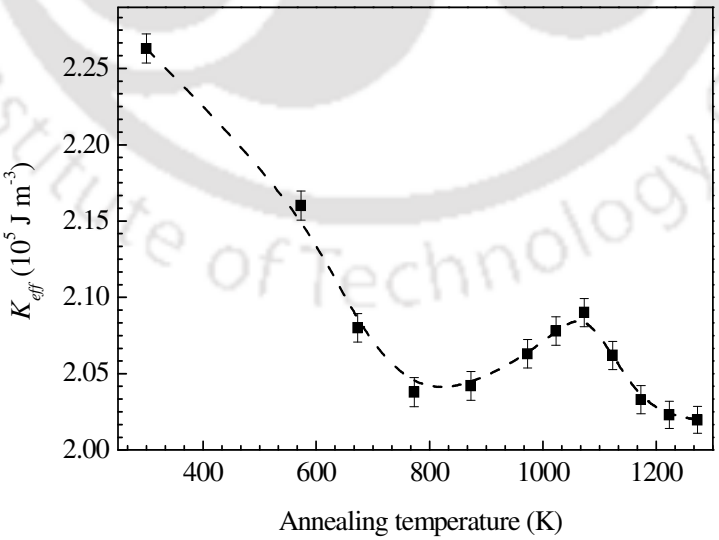

Figure 4.15: Variation of effective anisotropy constant (K_{eff}) of $Fe_{75}Si_{25}$ powders annealed at different temperatures for 4 hours.

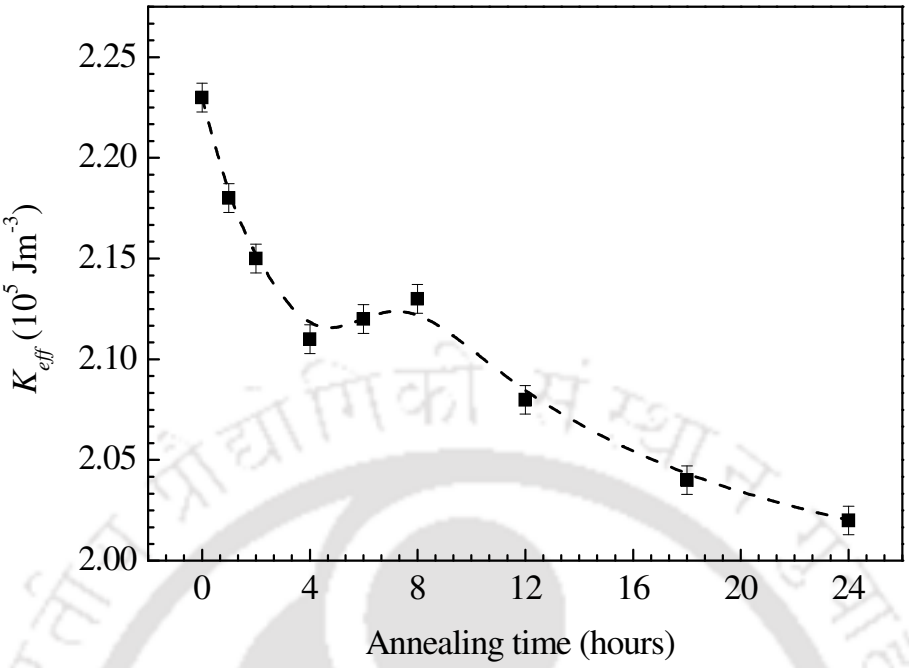

Figure 4.16: Variation of effective anisotropy constant (K_{eff}) of $Fe_{75}Si_{25}$ powders annealed at 873 K for various time periods.

In order to study the effect of annealing on the Curie temperature (T_C), $M - T$ measurements were carried out for some selected powders (as-milled, annealed at 773 K and annealed at 1173 K). Figure 4.17 shows the $M - T$ plots of these powders recorded at a constant applied dc magnetic field of 100 Oe. T_C values of 987 K, 975 K and 965 K were obtained for the as-milled powders, powders annealed at 773 K and 1173 K, respectively. The higher T_C of as-milled powders may be due to the large strain present in the powders as discussed in chapter 3. With annealing, a slight decrease in T_C is observed, which indicates that strain may have effects on T_C of the powders.

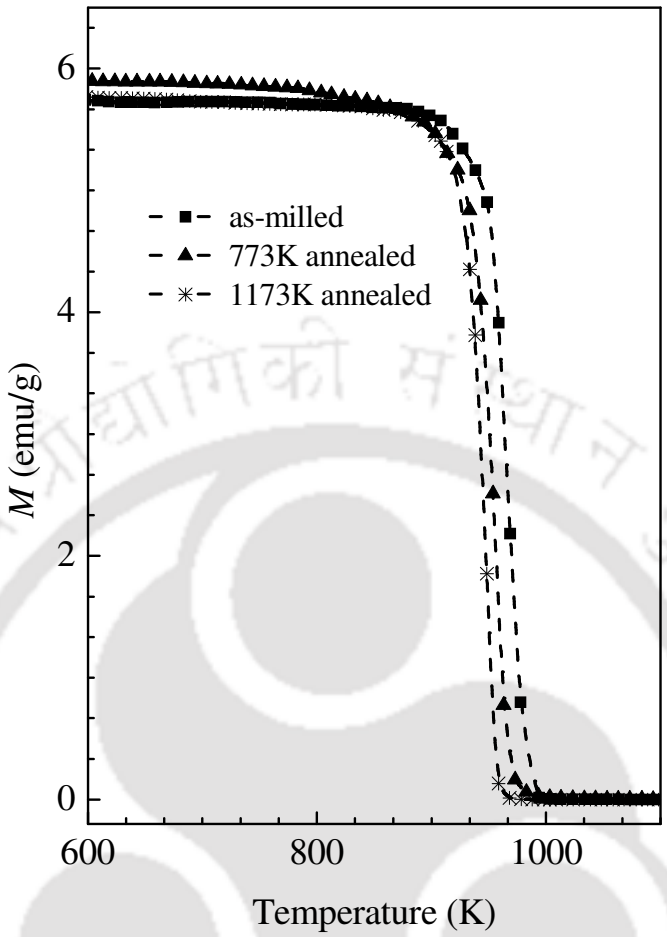

Figure 4.17: $M - T$ plots of as-milled powders, powders annealed at 773K and 1173K for 4 hours, of $Fe_{75}Si_{25}$.

4.3. Effect of heat treatment on the structure and magnetic properties of Fe-Si-M powders

4.3.1. Effect of heat treatment on structure

XRD patterns of as-milled and annealed powders of Fe-Si-M (M = Al, B, Cr) are depicted in Figures 4.18 (a) to 4.23 (a). Figure 4.18 (b) to 4.23 (b) show the XRD patterns of Fe-Si-M powders in the 2θ range of 40^o to 50^o in expanded scale. Absence of Si and M reflections in the XRD patterns of as-milled powders indicates the formation of

non-equilibrium solid solution α-Fe(Si,M) during the milling process as discussed earlier. The XRD patterns of the annealed powders show a transformation of the disordered α-Fe(Si,M) to the ordered superlattice DO_3 phase with increasing annealing temperature as evident from the Figure 4.18 (b) to Figure 4.23 (b). In order to observe the very weak superlattice reflections, the XRD data of Fe-Si-M powders annealed at 1173 K were recorded at a very slow scan of 0.005^o per second. The average crystallite sizes of the disordered α-Fe(Si,M) and ordered DO_3 phases of Fe-Si-M powders were estimated using the Scherrer's method from the FWHM of the (110) reflection of the XRD patterns [47]. The average crystallite sizes of ~10 nm were estimated for the as-milled powders of Fe-Si-M. Presence of strain in the mechanically alloyed powders can also contribute to the broadening of the FWHM of the XRD reflections. However, the strain contribution to the FWHM could not be calculated because of the low intensity of higher angle reflections. Figure 4.25 illustrate the average crystallite size (D) of as-milled and annealed powders of $Fe_{75}Si_{20}M_5$ and $Fe_{75}Si_{15}M_{10}$, respectively. A gradual increase of average crystallite size has been observed with increasing annealing temperatures. Thus, annealing resulted in atomic ordering with simultaneous growth of crystallite size in the Fe-Si-M powders.

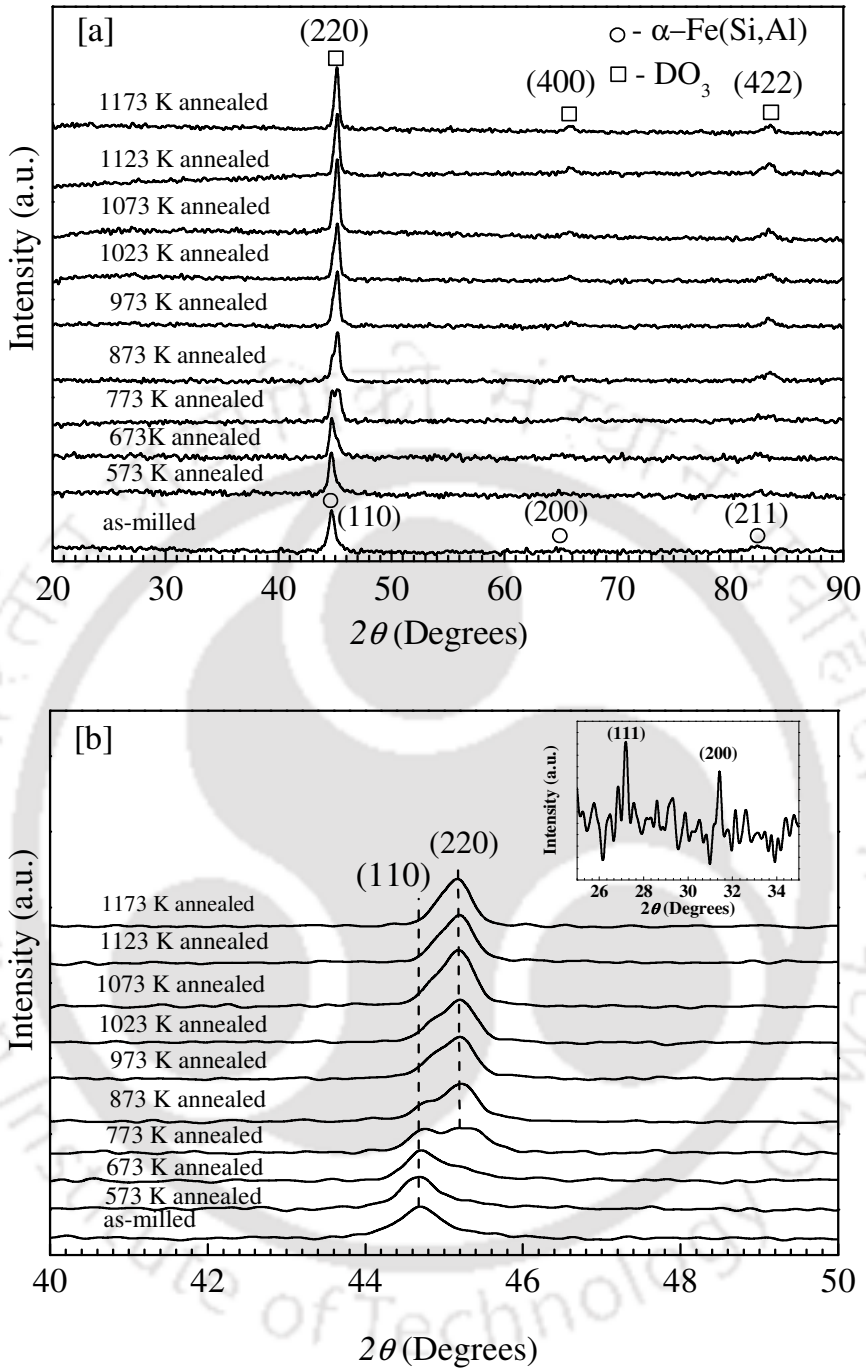

Figure 4.18: (a) XRD patterns of $Fe_{75}Si_{20}Al_5$ powders as a function of annealing temperature. (b) XRD patterns in 2θ range of 40^o to 50^o in expanded scale. Inset of Figure 4.18 (b) shows the superlattice reflections of the $Fe_{75}Si_{20}Al_5$ powders annealed at 1173 K.

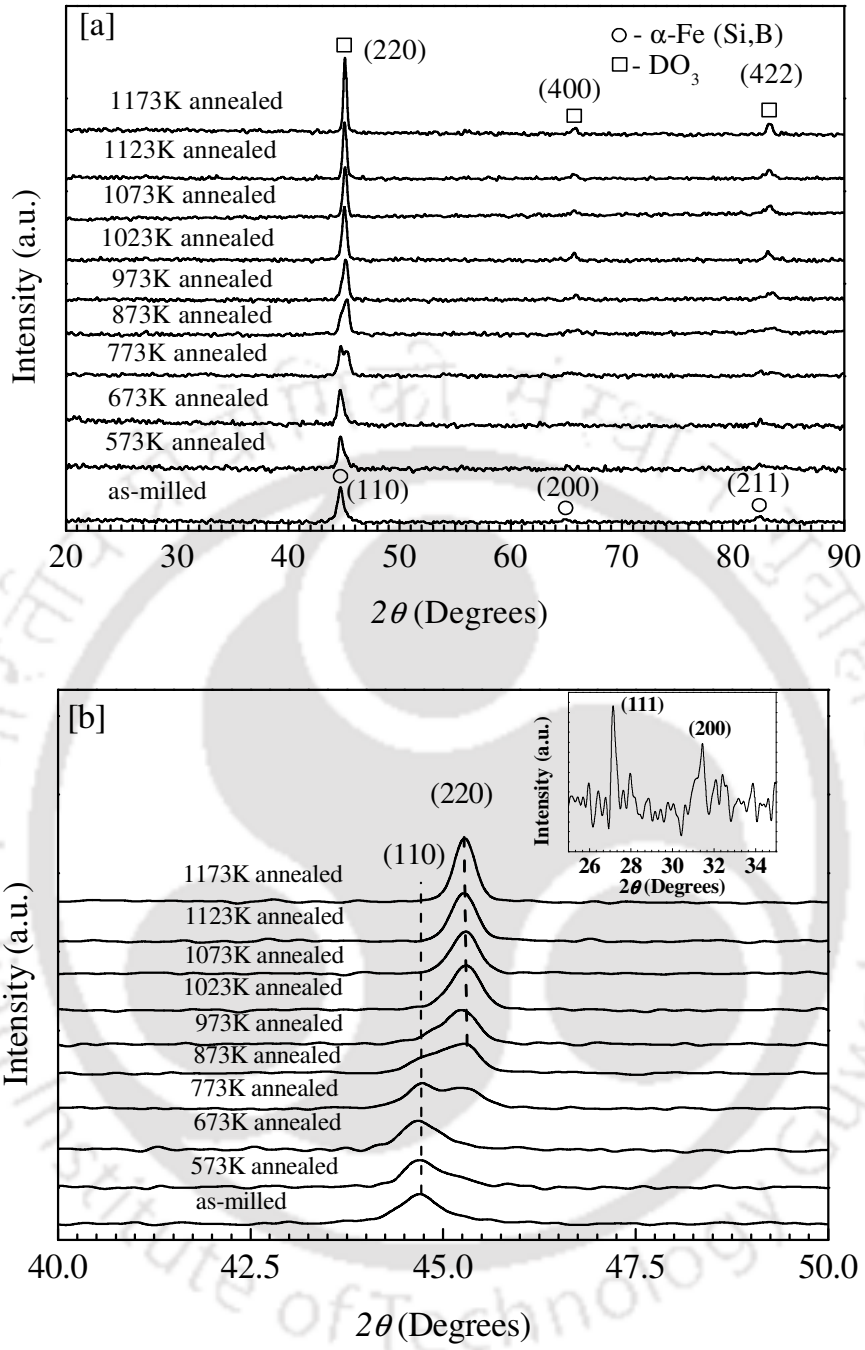

Figure 4.19: (a) XRD patterns of $Fe_{75}Si_{20}B_5$ powders as a function of annealing temperature (b) XRD patterns in 2θ range of 40^o to 50^o in expanded scale. Inset of Figure 4.19(b) shows the superlattice reflections of the $Fe_{75}Si_{20}B_5$ powders annealed at 1173 K.

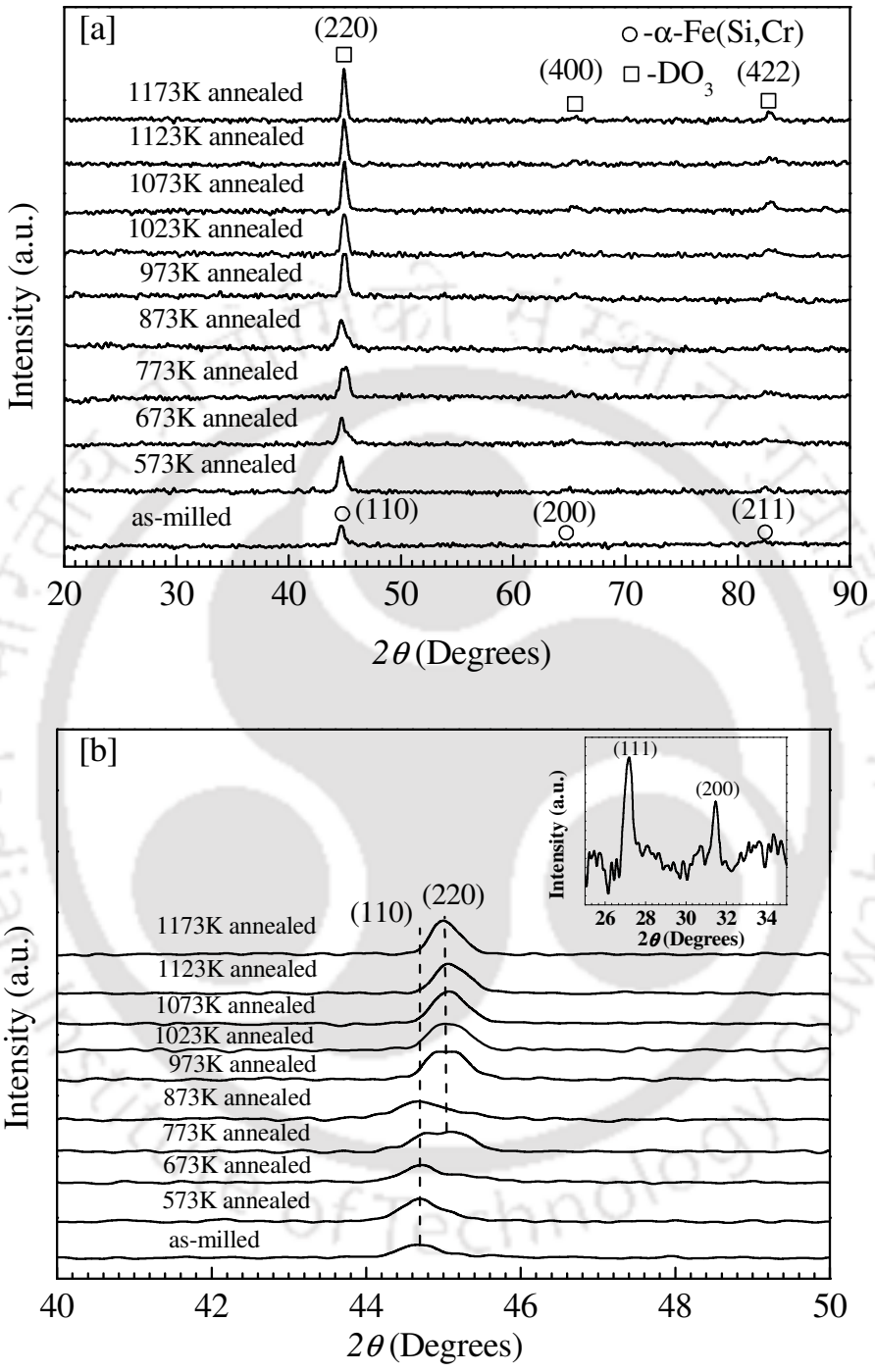

Figure 4.20: (a) XRD patterns of $Fe_{75}Si_{20}Cr_5$ powders as a function of annealing temperature (b) XRD patterns in 2θ range of 40^o to 50^o in expanded scale. Inset of Figure 4.20(b) shows the superlattice reflections of the $Fe_{75}Si_{20}Cr_5$ powders annealed at 1173 K.

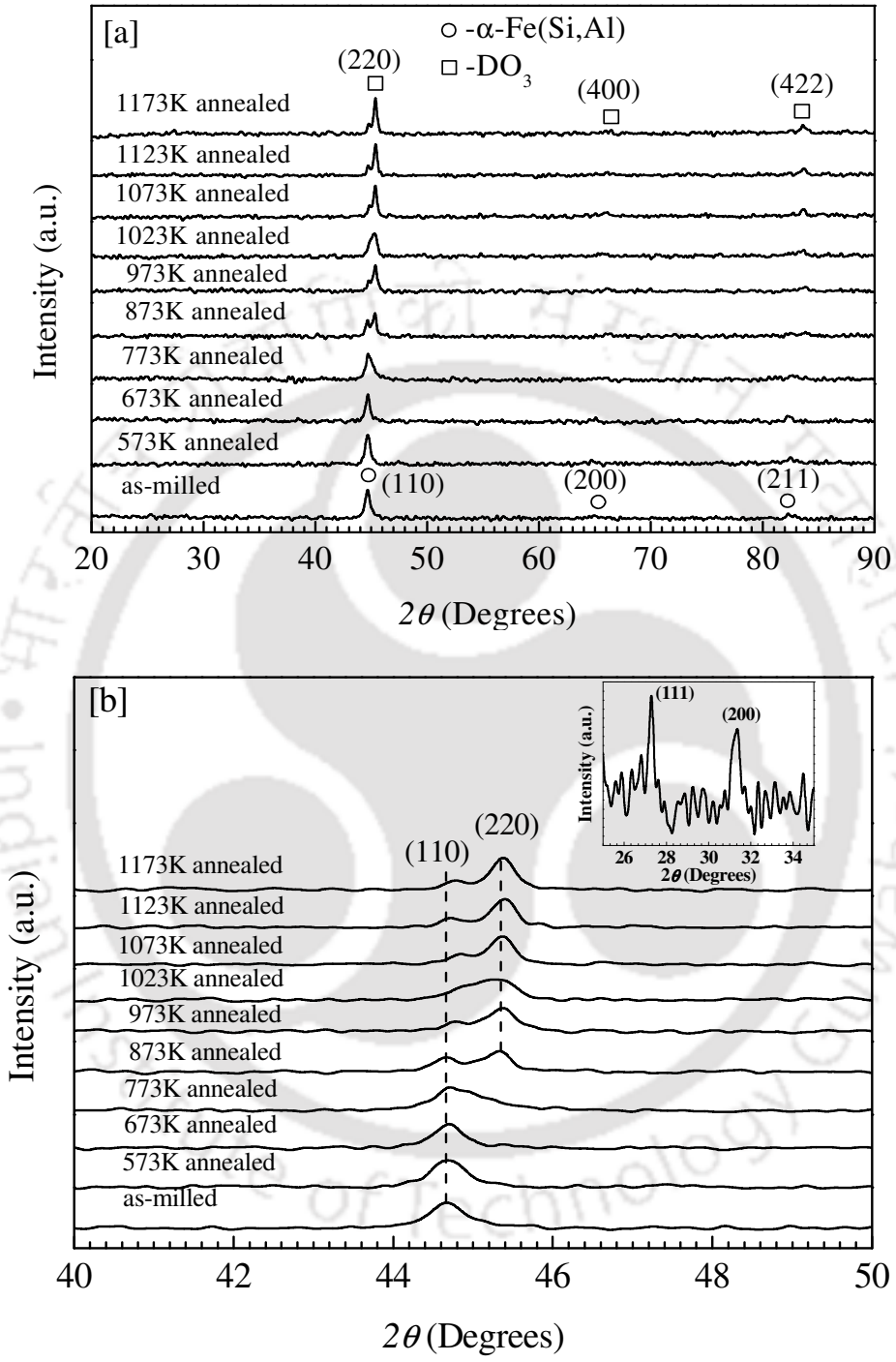

Figure 4.21: (a) XRD patterns of $Fe_{75}Si_{15}Al_{10}$ powders as a function of annealing temperature (b) XRD patterns in 2θ range of 40^{o} to 50^{o} in expanded scale. Inset of Figure 4.21 (b) shows the superlattice reflections of $Fe_{75}Si_{15}Al_{10}$ powders annealed at 1173 K.

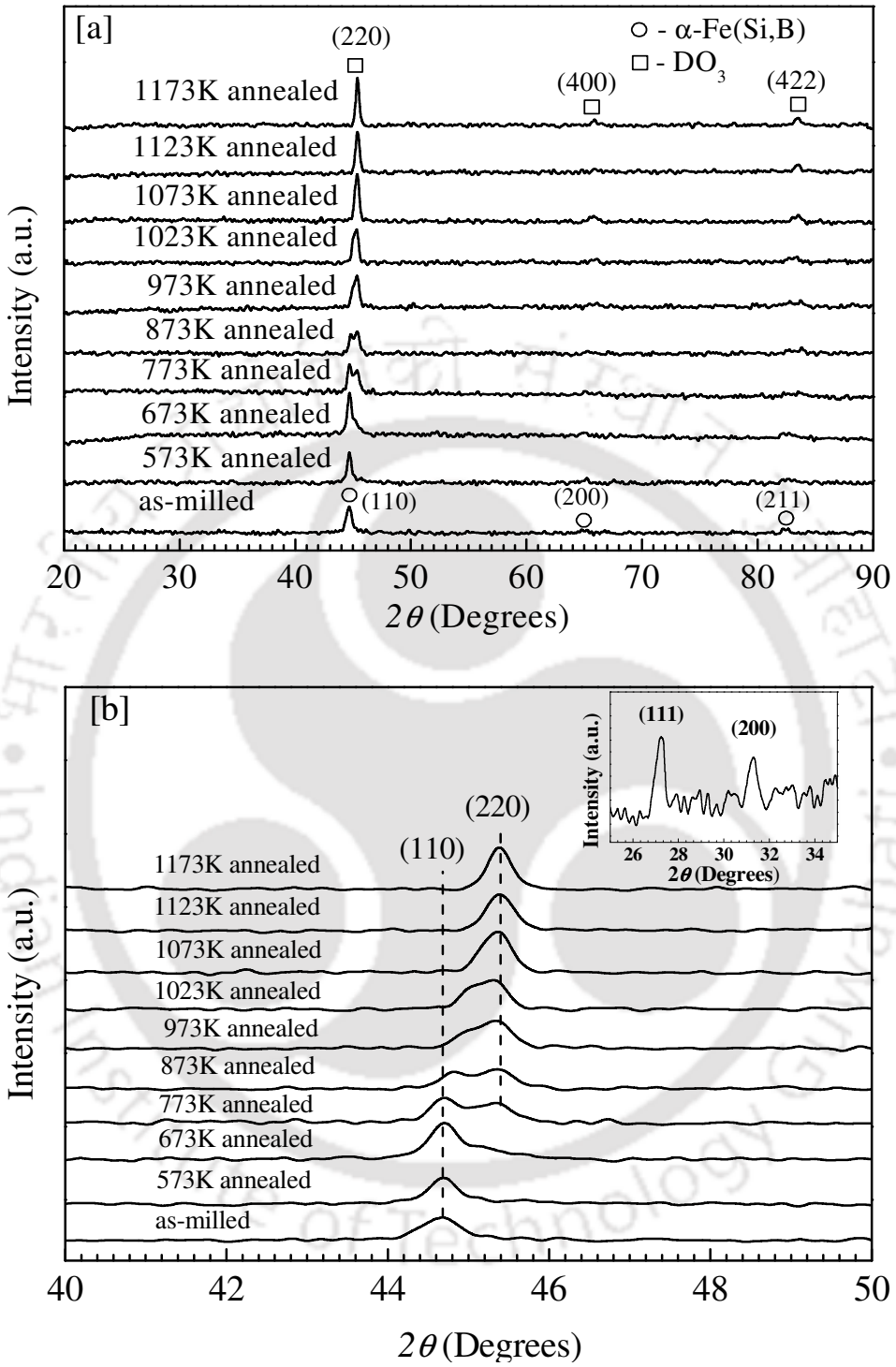

Figure 4.22: (a) XRD patterns of $Fe_{75}Si_{20}B_{10}$ powders as a function of annealing temperature (b) XRD patterns in 2θ range of 40^{o} to 50^{o} in expanded scale. Inset of Figure 4.22 (b) shows the superlattice reflections of the $Fe_{75}Si_{20}B_{10}$ powders annealed at 1173 K.

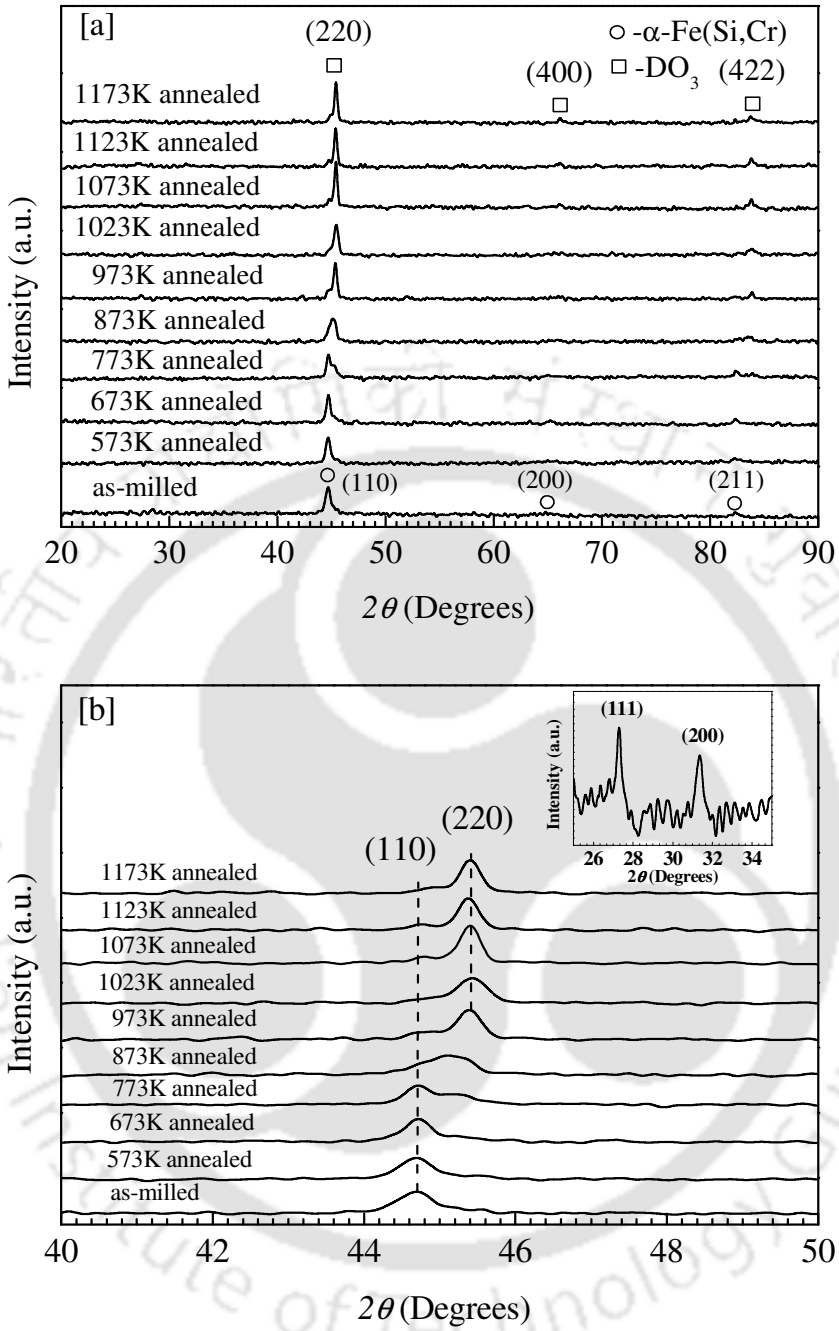

Figure 4.23: (a) XRD patterns of $Fe_{75}Si_{15}Cr_{10}$ powders as a function of annealing temperature (b) XRD patterns in 2θ range of 40^{o} to 50^{o} in expanded scale. Inset of Figure 4.23 (b) shows the superlattice reflections of $Fe_{75}Si_{15}Cr_{10}$ powders annealed at 1173 K.

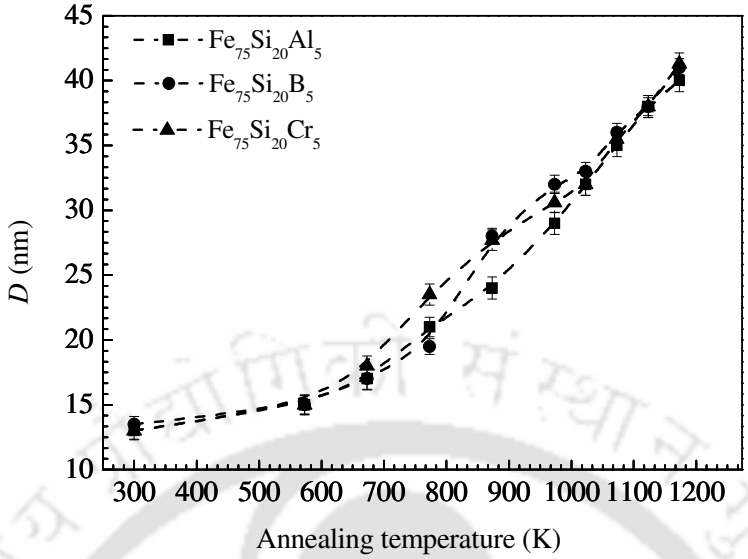

Figure 4.24: Variation of crystallite size (D) of $Fe_{75}Si_{20}M_5$ (M=Al, B, Cr) powders with increasing annealing temperatures.

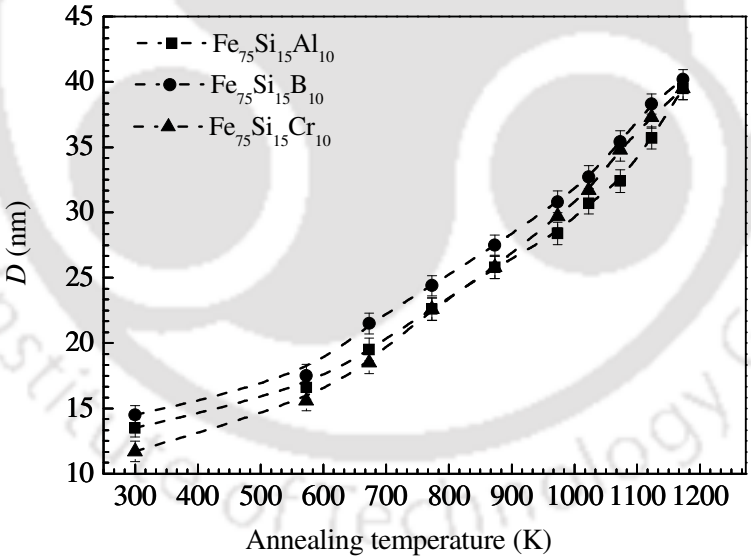

Figure 4.25: Variation of crystallite size (D) of $Fe_{75}Si_{15}M_{10}$ (M=Al, B, Cr) powders with increasing annealing temperatures.

4.3.2. Effect of heat treatment on magnetic properties

In order to investigate the effects of annealing on the coercivity and magnetic moments of mechanically alloyed Fe-Si-M powders, room temperature hystersis (M – H) loops were obtained. Figure 4.26 and Figure 4.27 show the M – H loops of $Fe_{75}Si_{20}M_5$ and $Fe_{75}Si_{15}M_{10}$ powders respectively. Insets of the figures show the M – H loops near the origin in expanded scale.

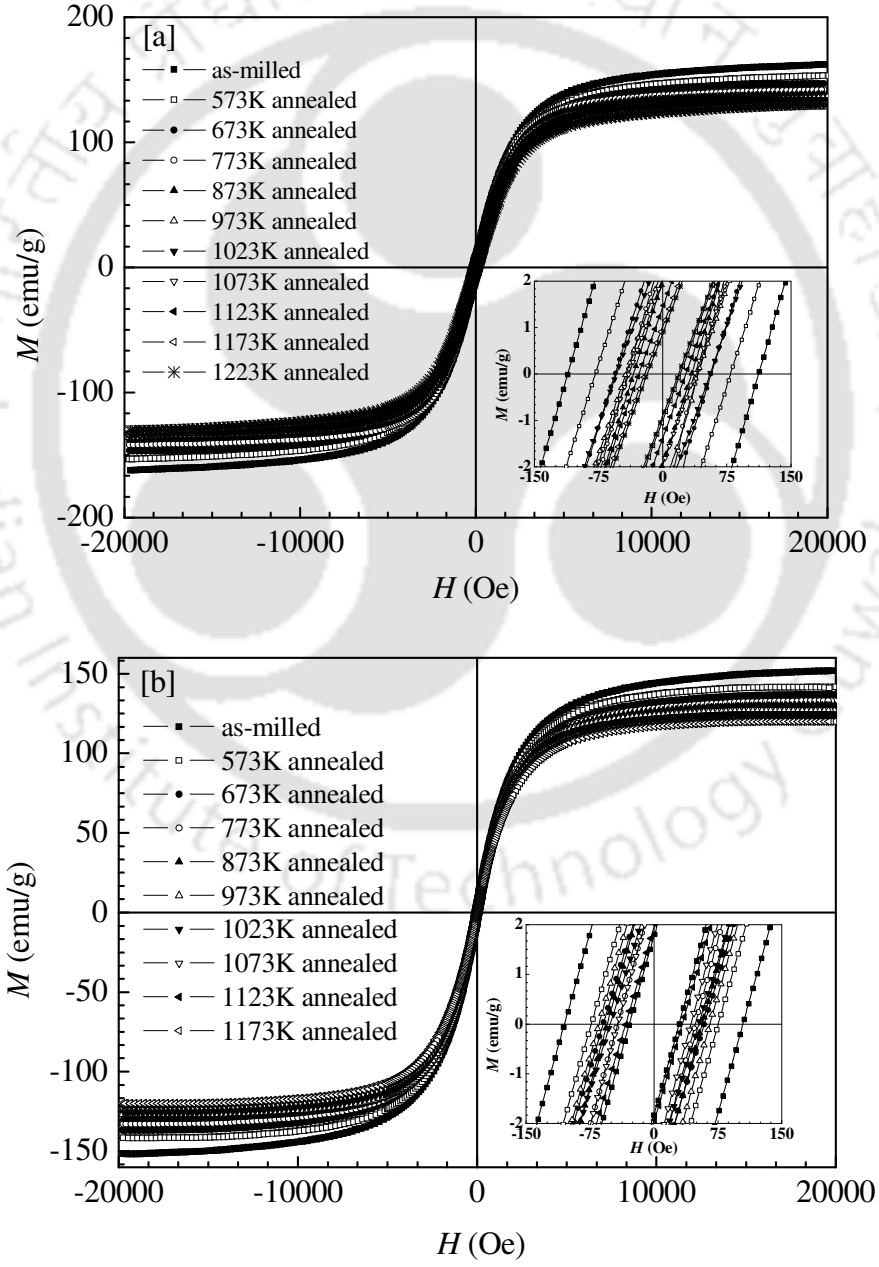

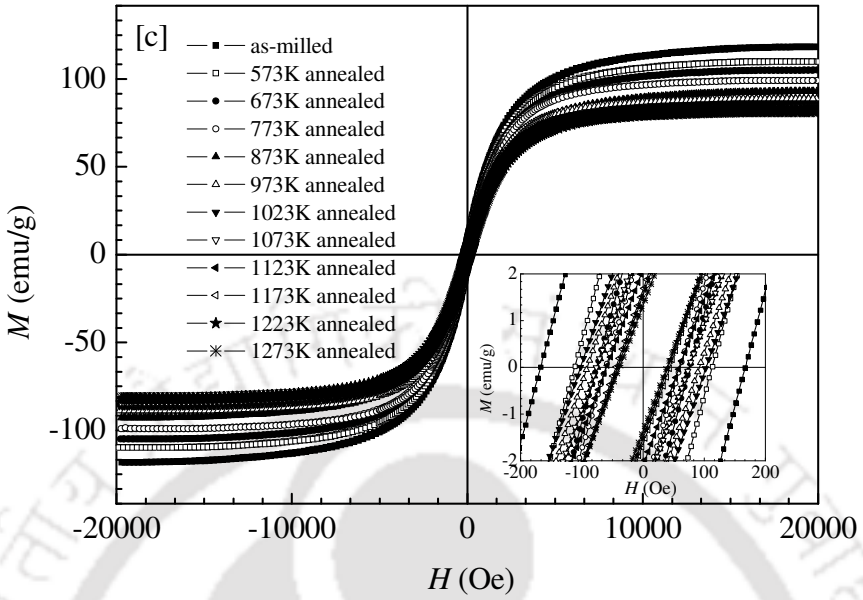

Figure 4.26: $M - H$ loops of as-milled and annealed powders of $Fe_{75}Si_{20}M_5$ [M=Al (a), B (b), Cr (c)] powders. Insets: the $M - H$ curves close to the origin are shown in expanded scale.

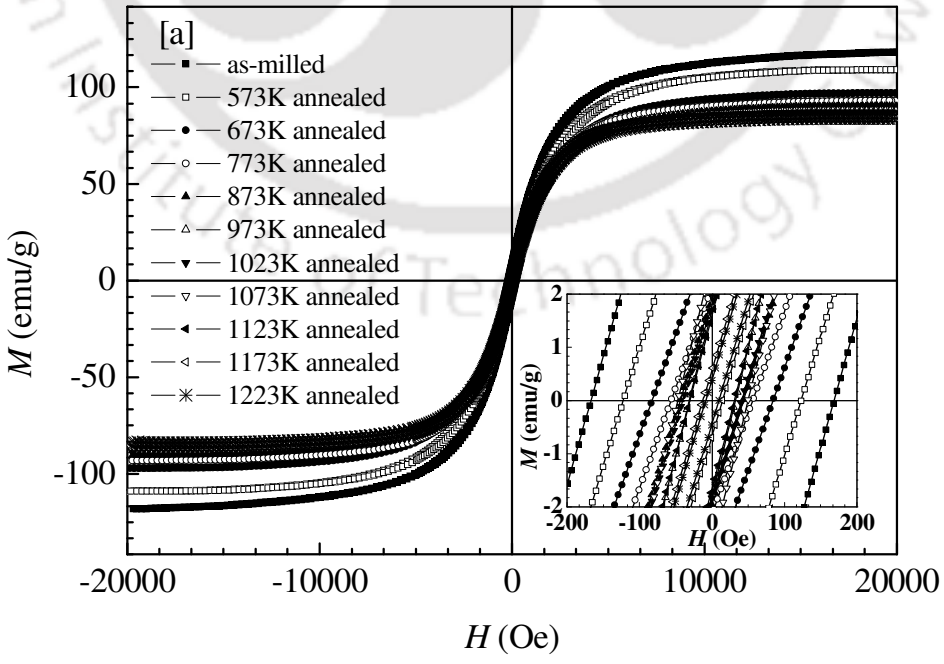

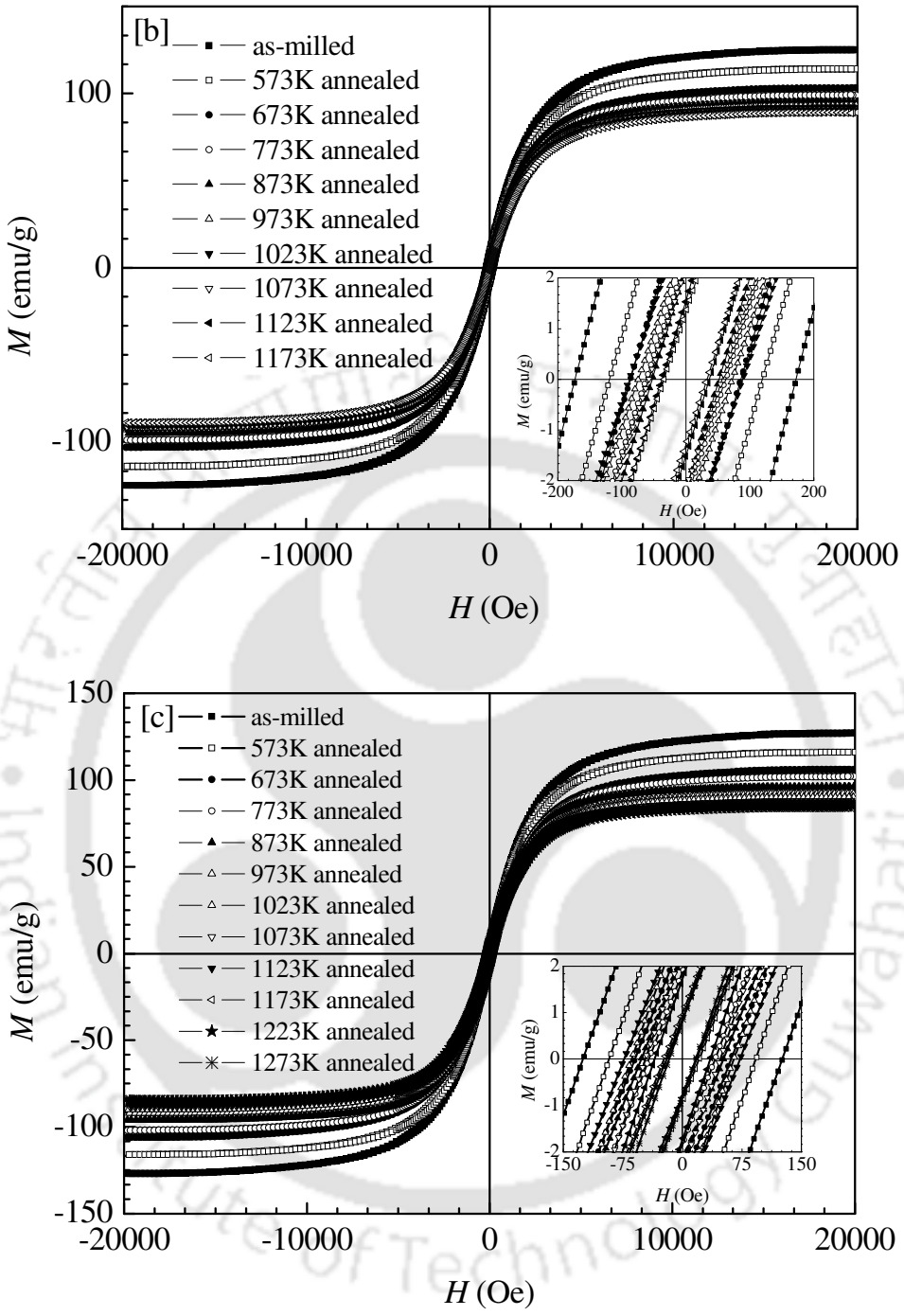

Figure 4.27: $M - H$ loops of as-milled and annealed powders of $Fe_{75}Si_{15}M_{10}$ [Al (a), B (b), Cr (c)] powders. Insets: the $M - H$ curves close to the origin are shown in expanded scale.

The variation of coercivity (H_C) of annealed $Fe_{75}Si_{20}M_5$ and $Fe_{75}Si_{15}M_{10}$ powders is shown in Figure 4.28 and Figure 4.29, respectively. The variation of average magnetic moment (μ) per Fe atom of annealed $Fe_{75}Si_{20}M_5$ and $Fe_{75}Si_{15}M_{10}$ powders is shown in Figure 4.30 and Figure 4.31, respectively. The average magnetic moment per Fe atom of Fe-Si-M powders decreases with increasing annealing temperatures which is attributed to the occurrence of atomic order during the annealing process [69,70]. A significant decrease of coercivity has been observed for the lower annealing temperatures which may be related to the possible decrease of strains during the annealing process. However, a prominent increase of coercivity in the intermediate annealing temperatures followed by decrease of coercivity in the higher annealing temperatures has been observed. The increase of the coercivity in the intermediate annealing temperature ranges can be well explained by the random anisotropy model (RAM) [23]. According to RAM, when the crystallite size is less than the ferromagnetic exchange length which is about 35 nm for Fe-Si based alloys, magnetocrystalline anisotropy reduces drastically and coercivity varies as the sixth power of crystallite size. Figure 4.32 and Figure 4.33 show the plots between coercivity (H_C) and sixth power of crystallite size (D^6) in the annealing temperature range where coercivity increased with increasing crystallite sizes for $Fe_{75}Si_{20}M_5$ and $Fe_{75}Si_{15}M_{10}$ powders, respectively. A nearly linear variation between H_C and D^6 indicates the influence of nanocrystallites on the coercivity as predicted by RAM. The decrease of coercivity in the higher annealing temperatures where coercivity decreases can be explained by the well known D^{-1} (where D is the crystallite size) law for coarse grained alloys. Plots between H_C and D^{-1} are shown in Figure 4.34 and Figure 4.35 for $Fe_{75}Si_{20}M_5$ and $Fe_{75}Si_{15}M_{10}$ powders, respectively.

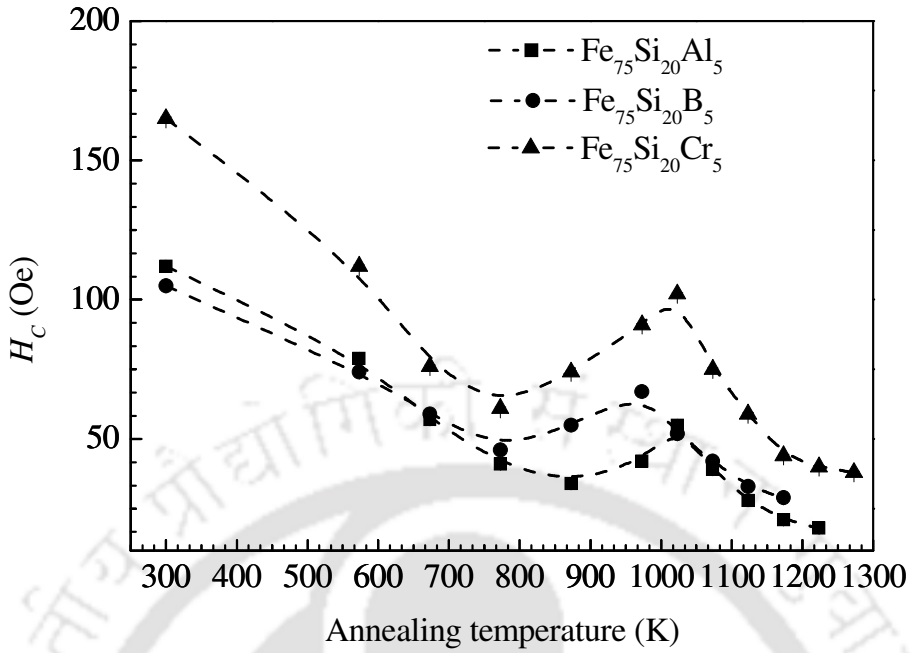

Figure 4.28: Variation of coercivity (H_C) of $Fe_{75}Si_{20}M_5$ [M=Al, B, Cr)] powders as a function of annealing temperature.

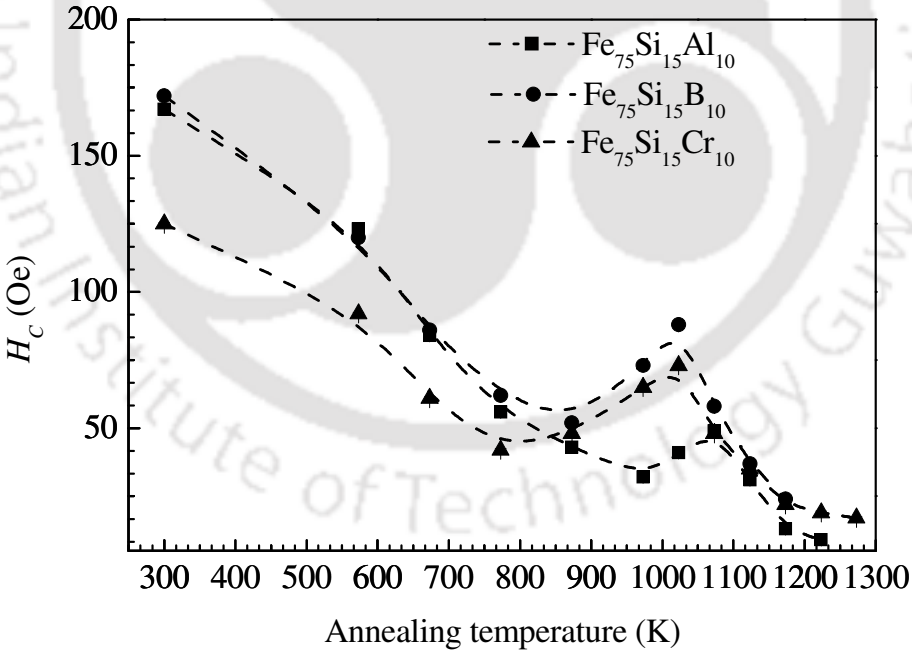

Figure 4.29: Variation of coercivity (H_C) of $Fe_{75}Si_{15}M_{10}$ [M=Al , B, Cr] powders as a function of annealing temperature.

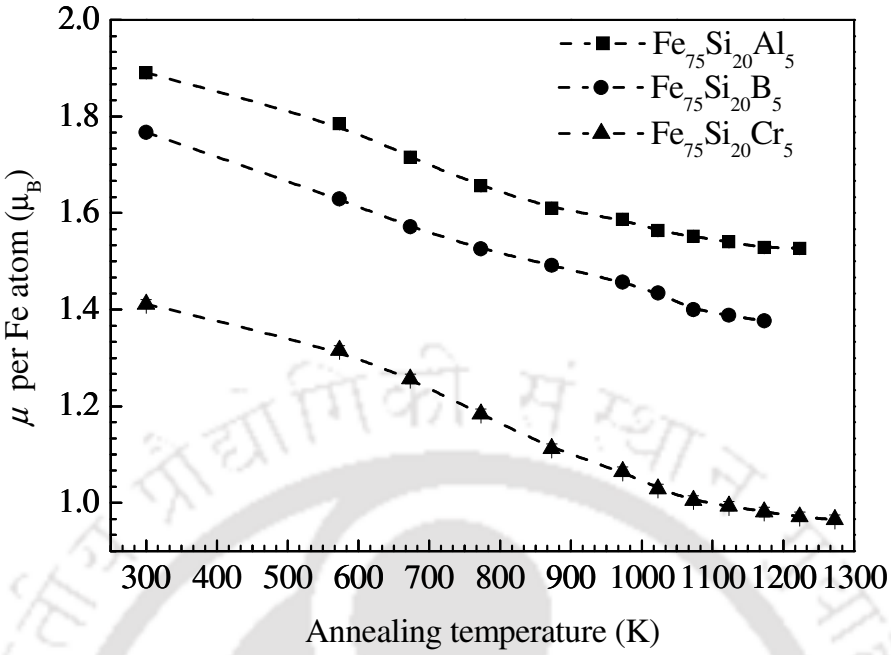

Figure 4.30: Variation of average magnetic moment (μ) per Fe atom of $Fe_{75}Si_{20}M_5$ (M=Al, B, Cr) powders as a function of annealing temperature.

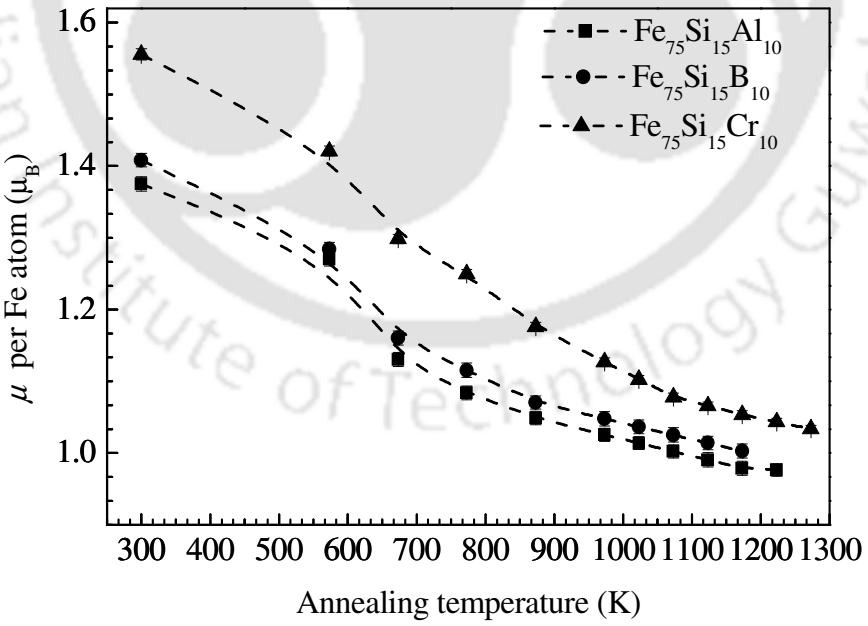

Figure 4.31: Variation of average magnetic moment (μ) per Fe atom of $Fe_{75}Si_{15}M_{10}$ (M=Al, B, Cr) powders as a function of annealing temperature.

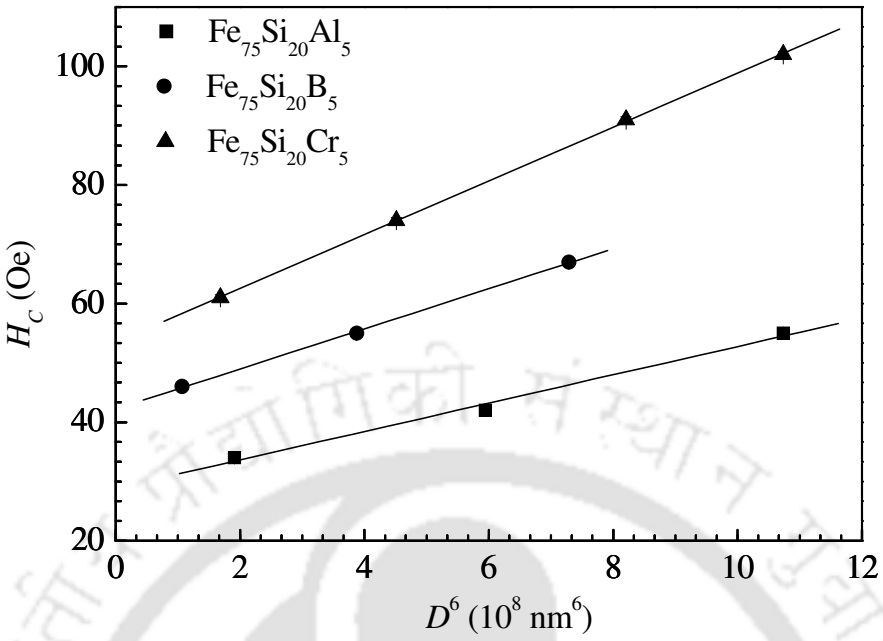

Figure 4.32: Plot between H_C and D^6 for annealed $Fe_{75}Si_{20}M_5$ (M=Al, B, Cr) powders in the regime where coercivity increases with increasing annealing temperature.

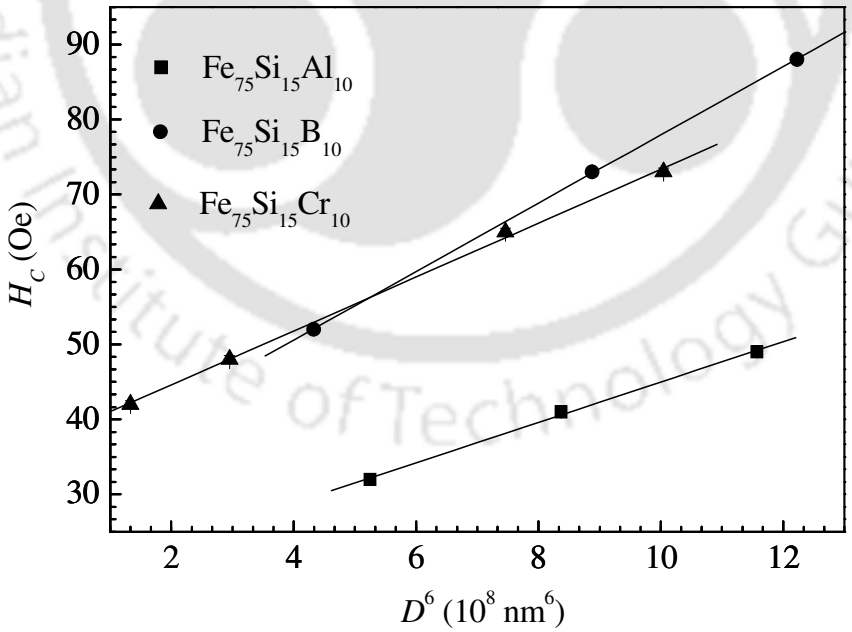

Figure 4.33: Plot between H_C and D^6 for annealed $Fe_{75}S_{15}M_{10}$ (M=Al, B, Cr) powders in the regime where coercivity increases with increasing annealing temperature.

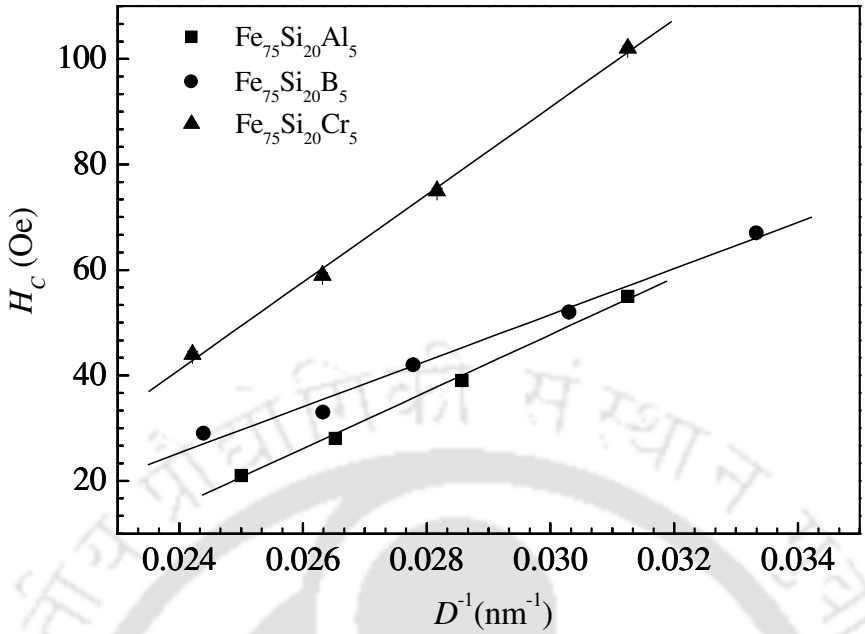

Figure 4.34: Plot between H_C and D^{-1} of $Fe_{75}Si_{20}M_5$ (M=Al, B, Cr) powders with higher crystallite sizes.

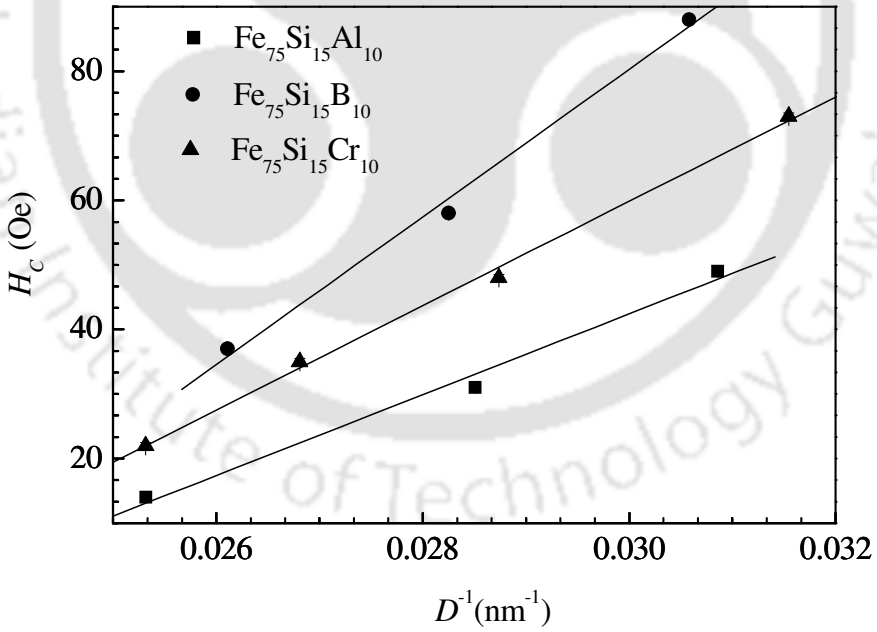

Figure 4.35: Plot between H_C and D^{-1} of $Fe_{75}Si_{15}M_{10}$ (M=Al, B, Cr) powders with higher crystallite sizes.

The effective anisotropy constant (K_{eff}) of the as-milled and annealed Fe-Si-M powders has been estimated using the law of approach to saturation. Figure 4.36 and Figure 4.37 show the variation of K_{eff} of the $Fe_{75}Si_{20}M_5$ and $Fe_{75}Si_{15}M_{10}$ powders with increasing annealing temperatures. Annealing has been observed to have a significant effect on K_{eff} values. The variations followed trends similar to the ones observed for the variation of coerivity with annealing temperatures (*cf.* Figure 4.28) and annealing time (*cf.* Figure 4.29).

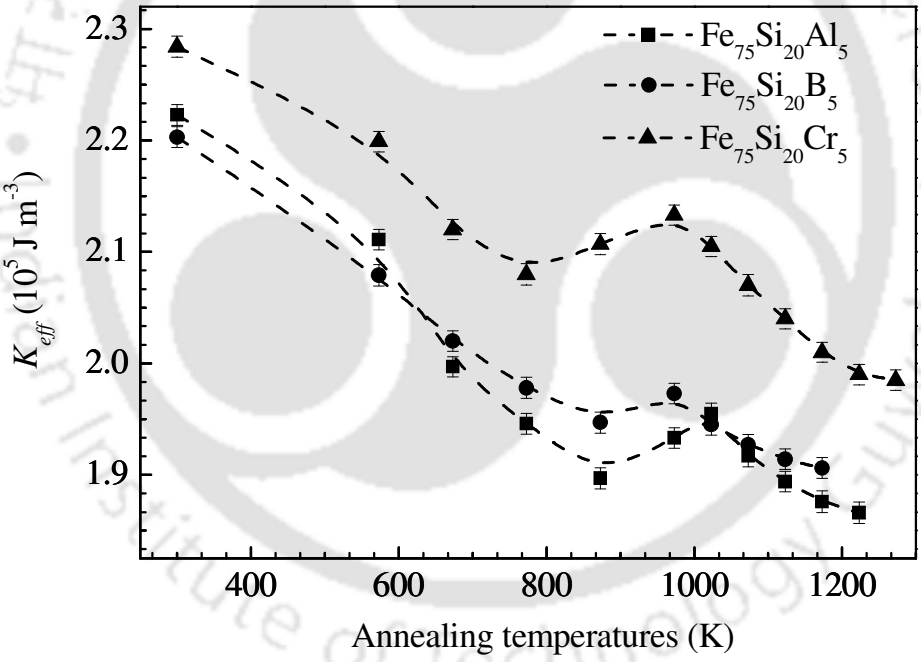

Figure 4.36: Variation of K_{eff} of $Fe_{75}Si_{20}M_5$ (M=Al, B, Cr) powders with annealing temperature.

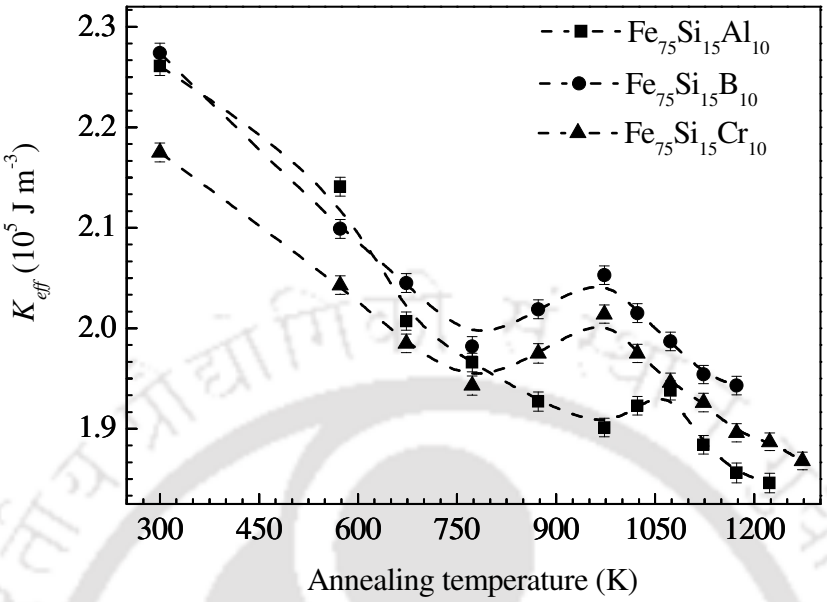

Figure 4.37: Variation of K_{eff} of $Fe_{75}Si_{15}M_{10}$ (M=Al, B, Cr) powders with annealing temperature.

4.4. Comparison of the properties of Fe-Si and Fe-Si-M powders

Annealing on mechanically alloyed Fe-Si and Fe-Si-M (M=Al, B, Cr) powders has similar effects on the structure and magnetic properties. A gradual transformation of the α-Fe(Si) phase in as-milled powders into ordered DO_3 phase (Fe_3Si) is observed on annealing at different temperatures for same time period as well as for different time periods at a particular temperature case of $Fe_{75}Si_{25}$ powders. A similar structural change to ordered DO_3 phase has been observed in all the mechanically alloyed powders with compositions $Fe_{75}Si_{20}M_5$ and $Fe_{75}Si_{15}M_{10}$ upon annealing. As both Fe_3Si and Fe_3Al have equilibrium DO_3 structure for $Fe_{75}Si_{25}$ and $Fe_{75}Al_{25}$ atomic compositions, in ordered $Fe_{75}Si_{20}Al_5$ and $Fe_{75}Si_{15}Al_{10}$ powders, some Si sites (*cf.* Figure 4.2) of DO_3 structure may be substituted by Al [41]. In the case of Fe-Si-B powders, since the diffusivity of B in Fe

matrix is very less, very few B atoms can be present in the Fe-matrix with the equilibrium phase of Fe_3Si still persisting in Fe-Si-B powders after annealing. Here, it is worth mentioning that, Fe-Si powders show equilibrium DO_3 phase in the composition range 9.5 to 26.5 atomic % of Si [66]. Transformation of disordered α-Fe(Si,Cr) phase in as-milled powders to ordered DO_3 phase has also been observed in case of $Fe_{75}Si_{20}Cr_5$ and $Fe_{75}Si_{15}Cr_{10}$ powders. Thus, the present study reveals that the ordered DO_3 phase is preserved even after 10% addition of the third element M (M=Al, B, Cr) in Fe-Si alloys. Annealing promotes growth of crystallite size and reduction of defects in the annealed powders and simultaneously induces atomic ordering.

Table 4.1: Comparison of magnetic parameters of various annealed powder compositions.

Alloy composition	Annealing temperature (K)	Coercivity H_C (Oe)	Saturation magnetization M_S (emu/g)
$Fe_{75}Si_{25}$	1273	52	136
$Fe_{75}Si_{20}Al_5$	1223	18	131
$Fe_{75}Si_{15}Al_{10}$	1223	09	85
$Fe_{75}Si_{20}B_5$	1173	29	120
$Fe_{75}Si_{15}B_{10}$	1173	34	89
$Fe_{75}Si_{20}Cr_5$	1273	38	82
$Fe_{75}Si_{15}Cr_{10}$	1273	17	85

Magnetic properties of Fe-Si and Fe-Si-M powders strongly depend on the alloy composition. The magnetic moment of the annealed Fe-Si powders has been found to be higher when compared to all the compositions annealed at the particular temperature. On

the other hand, $Fe_{75}Si_{15}Cr_{10}$ powders have been observed to have the lowest magnetic moment among all the compositions investigated in this work. Coercivity of the materials decreases drastically in all the alloy compositions upon annealing at higher temperatures. $Fe_{75}Si_{15}Al_{10}$ powders annealed at 1223 K exhibited coercivity of 9 Oe which is the lowest among the annealed powders. A comparison of the lowest coercivity of the annealed powders of different alloy compositions along with their saturation magnetization has been presented in Table 4.1.

4.5. Summary

Annealing of mechanically alloyed nanocrystalline Fe-Si and Fe-Si-M powders at elevated temperatures has significant effects on their structure and soft magnetic properties. Upon annealing, a gradual transformation of the non-equilibrium solid solution α-Fe(Si) phase in the as-milled powders to ordered DO_3 phase is observed, accompanied by growth of crystallite size and reduction of dislocation density with increasing annealing temperatures. The average magnetic moment per Fe atom decreased slightly after annealing which is attributed to the occurrence of atomic ordering. Coercivity has been observed to be dominated by dislocation density in samples annealed at lower temperatures. In samples annealed at intermediate temperatures, coercivity depends on crystallite size as predicted by random anisotropy model. In samples annealed at higher temperatures, coercivity depends on reciprocal of crystallite size, a behaviour observed in coarse grained alloys. Crystallite size comparable to ferromagnetic exchange length separates these two types of dependency of coercivity on crystallite size. Although annealing causes significant improvement of the soft magnetic properties of the

mechanically alloyed Fe-Si and Fe-Si-M powders, the residual defects present in the annealed powders result in higher coercivity values in the powders as compared to melt-spun ribbons. The correlation between structure and magnetic properties in annealed Fe-Si and Fe-Si-M powders has been found to be similar. However, the structural and magnetic parameters are strongly dependent on the alloy composition. $Fe_{75}Si_{15}Al_{10}$ powders annealed at 1223 K exhibit the lowest coercivity of 9 Oe among the samples studied in this work.

Chapter 5

Nanocrystalline Fe-Si-Cr powders derived from amorphous precursor

Amorphous $Fe_{75}Si_{15}Cr_{10}$ powders have been synthesized from elemental powders of Fe, Si and Cr by high energy ball milling in a planetary ball mill. Annealing near and above the crystallization temperature of the amorphous powders result in the formation of non-equilibrium solid solution α-Fe(Si,Cr) with nanocrystalline structure. The correlation between structure, thermal and magnetic properties of the powders is discussed in this chapter.

5.1. Experimental details

Weighed quantities of high purity (> 99.9%) elemental Fe, Si and Cr powders corresponding to the composition of $Fe_{75}Si_{15}Cr_{10}$ were taken in a hardened steel vial together with 10 mm diameter hardened steel milling balls. The powder to ball weight ratio was maintained at 1:10. The vial was filled with high purity argon gas to minimize oxidation during milling. The planetary ball mill (Insmart, India) was operated at 400

rpm. In order to avoid excessive heating, the mill was programmed to halt for 30 minutes after every 30 minutes of operation. The powders milled for 100 hours were flame sealed in fused silica ampoules at a pressure of 10^{-4} Pa and annealed in the temperature range of 573 to 973 K for 4 hours each. Further, as-milled powders were annealed at 873 K for various time periods. The as-milled and annealed powder samples were analyzed using X-Ray diffractometer (Seifert 3003 T/T), transmission electron microscope (TEM, JEOL 2100), scanning electron microscope (SEM, LEO 1430VP), differential scanning calorimeter (DSC, Perkin-Elmer DSC 7) and vibrating sample magnetometer (VSM, Lakeshore, 7410).

5.2. Structure

XRD patterns of the as-mixed, 100 hours milled and annealed powders of $Fe_{75}Si_{15}Cr_{10}$ are presented in Figure 5.1. The as-mixed powders show the characteristic Bragg reflections corresponding to the individual elements. The reflections from Fe and Cr overlap because both the elements have body centered cubic (bcc) structures with closely matched lattice parameter values. After 100 hours of milling, the reflections corresponding to Si disappear completely and the reflections corresponding to Fe or Cr reduce in intensity and broaden into humps, signaling the formation of an amorphous structure. Composition analysis of the milled powder reveals the overall composition to be $Fe_{75.4}Si_{15.2}Cr_{9.4}$. XRD patterns of the powders annealed up to a temperature of 773 K exhibited features similar to that of milled powders, which confirms that the amorphous phase is preserved up to this temperature. On the other hand, XRD patterns of the

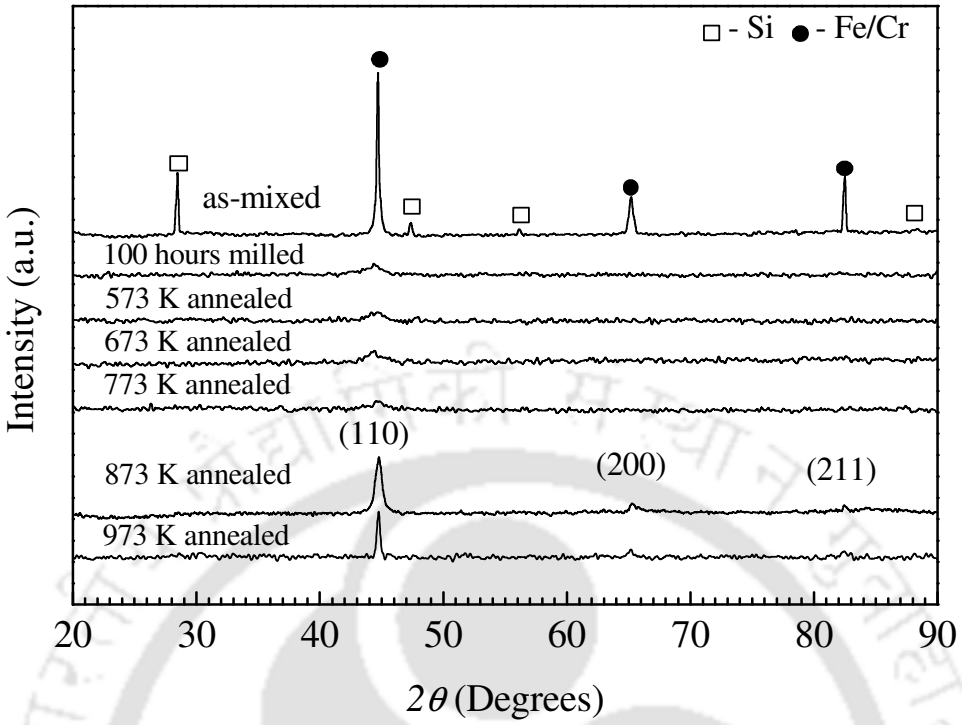

Figure 5.1: XRD patterns of as-mixed, 100 hours milled and annealed powders of $Fe_{75}Si_{15}Cr_{10}$.

powders annealed at 873 K and 973 K show the reappearance of XRD reflections at 2θ values close to those corresponding to α-Fe. The lattice parameter calculated from the peak positions of (110) reflections was 0.2859 nm for powders annealed at 873 K and 973 K. This value is slightly lower than that of pure α- Fe (0.2866 nm). This shows that the phase formed after annealing is not pure α-Fe. A higher change of the lattice parameter is expected for the formation of non-equilibrium α-Fe(Si) as the atomic radius of Si (0.118nm) is lower than that of α–Fe (0.123 nm) [40, 71]. However, as the atomic radius of Cr (0.128 nm) is higher than that of α-Fe, presence of Cr in Fe matrix would result in an increase in the lattice parameter. Thus, the phase formed after annealing of

the amorphous powders at 873 K and 973 K is α-Fe(Si,Cr). The overall compositions of the powders annealed at 873 K and 973 K were $Fe_{75.4}Si_{14.7}Cr_{9.9}$ and $Fe_{75.7}Si_{14.8}Cr_{9.5}$, respectively. The average crystallite size of the powders annealed at 873 K and 973 K were estimated from the broadening of the XRD reflections using Scherrer's formula [47]. The analyses yielded average crystallite sizes of 24 ± 1 nm and 47 ± 1 nm, for the powders annealed at 873 and 973 K, respectively.

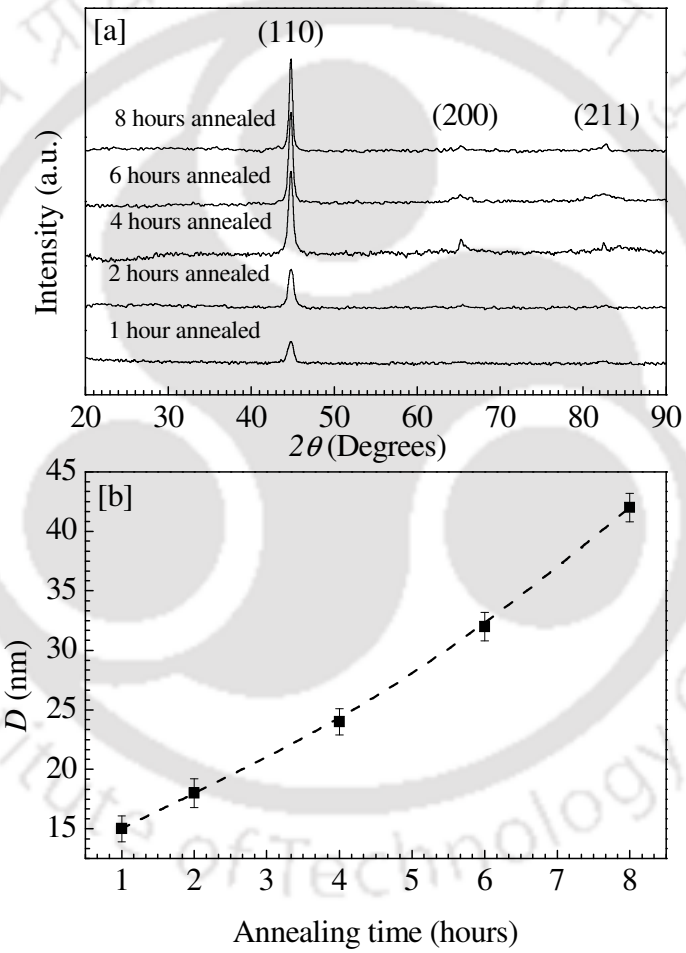

Figure 5.2: (a) XRD patterns of 100 hours milled $Fe_{75}Si_{15}Cr_{10}$ powders annealed at 873 K for different time periods. (b) Variation of average crystallite size (*D*) with different annealing time.

Figure 5.2 (a) shows the XRD patterns of amorphous powders annealed at 873 K for different time periods. Annealing resulted in the formation of non-equilibrium solid solution α-Fe(Si,Cr). Figure 5.2(b) depicts the average crystallite sizes of the powders annealed at 873 K for various time periods. A gradual increase of crystallite size was observed with increasing annealing time.

Figure 5.3 shows the bright field TEM (BF-TEM) images, selected area electron diffraction (SAED) and high resolution TEM (HRTEM) images of the 100 hours milled and annealed powders. The bright field image of the milled sample [Figure 5.3a(i)] displays the absence of any crystalline nature and the corresponding SAED pattern [Figure 5.3a(ii)] shows diffused halo ring pattern typical of an amorphous structure. There is also no evidence of any fine crystallites and/or any precipitate in the HRTEM image [Figure 5.3a(iii)]. This is in good agreement with the XRD results depicted in Figure 5.1. The BF-TEM images of the annealed samples at 873 K [Figure 5.3b(i)] and 973 K [Figure 5.3c(i)] clearly show the presence of nanocrystallites of average sizes of about 20 nm and 45 nm, respectively. These values are close to the values obtained from XRD peak analysis using Scherrer's formula. Some disordered atomic arrangements (amorphous like feature) are observed in the HRTEM images of the annealed powders. Some of those regions are encircled in the HRTEM images. SAED patterns show the polycrystalline nature of the powders with the rings corresponding to reflections from (110), (200) and (211) planes. *d*-spacings and lattice parameter calculated from the SAED patterns agree well with the values obtained from XRD peak analysis.

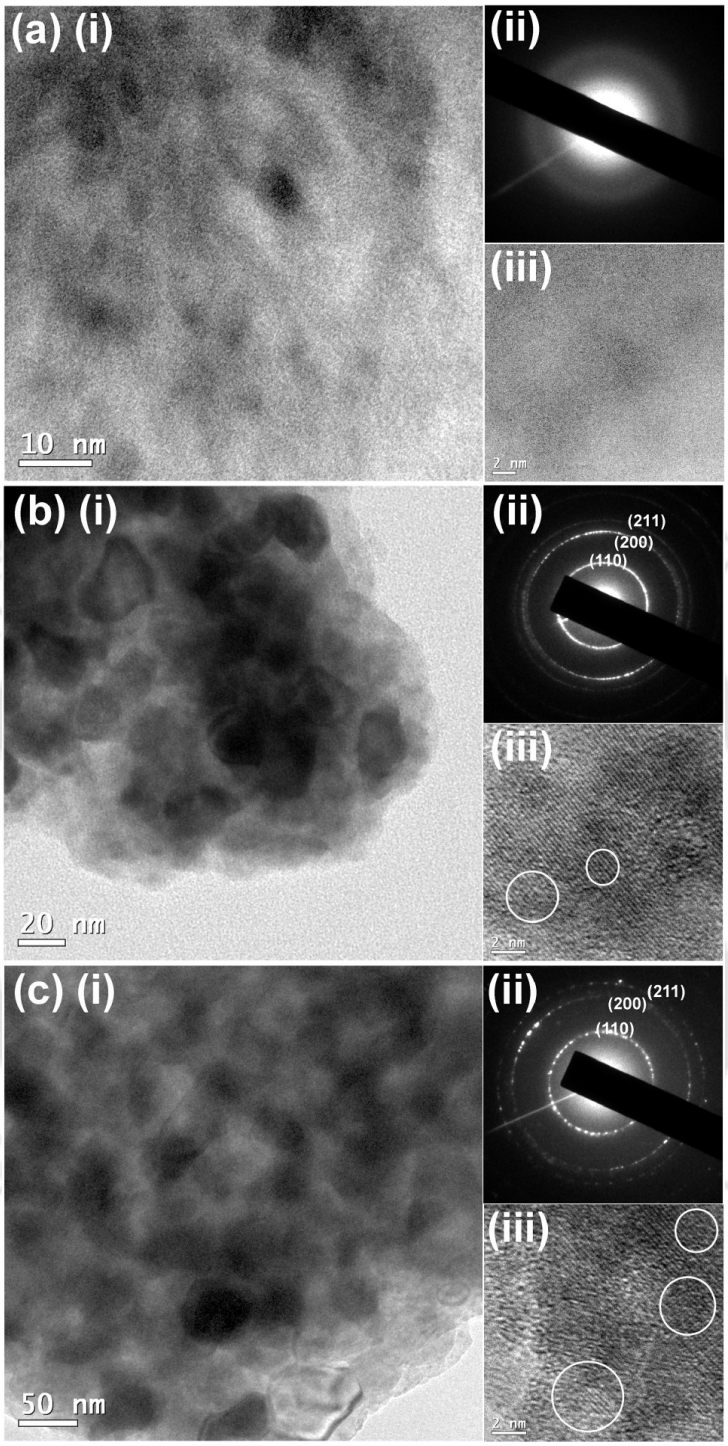

Figure 5.3: (i) BFTEM images, (ii) SAED patterns and (iii) HRTEM images of $Fe_{75}Si_{15}Cr_{10}$ powders milled for 100 hours (a), annealed at 873 K (b) and annealed at 973 K (c), respectively.

5.3. Thermal properties

Figure 5.4 shows the DSC curves of 100 hours milled and annealed powders recorded at a constant heating rate of 20 K per minute. The DSC curves reveal an endothermic process starting near 630 K followed by a sharp exothermic process with its peak value near 890 K as major features. The endothermic process observed can be readily attributed to the glass transition phenomenon [72,73]. XRD and TEM studies revealed that the crystallization of the amorphous powder occurs between 773 K and 973 K. Thereby, the sharp exothermic peak at 890 K is attributed to crystallization of α-Fe(Si,Cr). However, it should be noted that the Curie temperature (T_C) of the amorphous phase is also near to 890 K as revealed by VSM studies discussed later in the paper. Usually, a very weak signature of T_C is observed in DSC curves in ferromagnetic metallic glasses [72]. In the presently studied material, as crystallization temperature and the T_C lies very close to each other, any signature of T_C could not be distinguished from the crystallization temperature from the DSC studies. The DSC curves of the powders annealed at 873 K and 973 K do not show clear evidence of any observable thermodynamic transition, which confirms the crystallized state of the annealed powders. This result is reinforced by XRD and TEM studies as discussed earlier. Thus, all the three techniques (*viz.* XRD, TEM and DSC) give complementary yet supportive information about the amorphous nature of the 100 hours milled powders, the crystallization process and the effect of heat treatment of the amorphous powders at various temperatures.

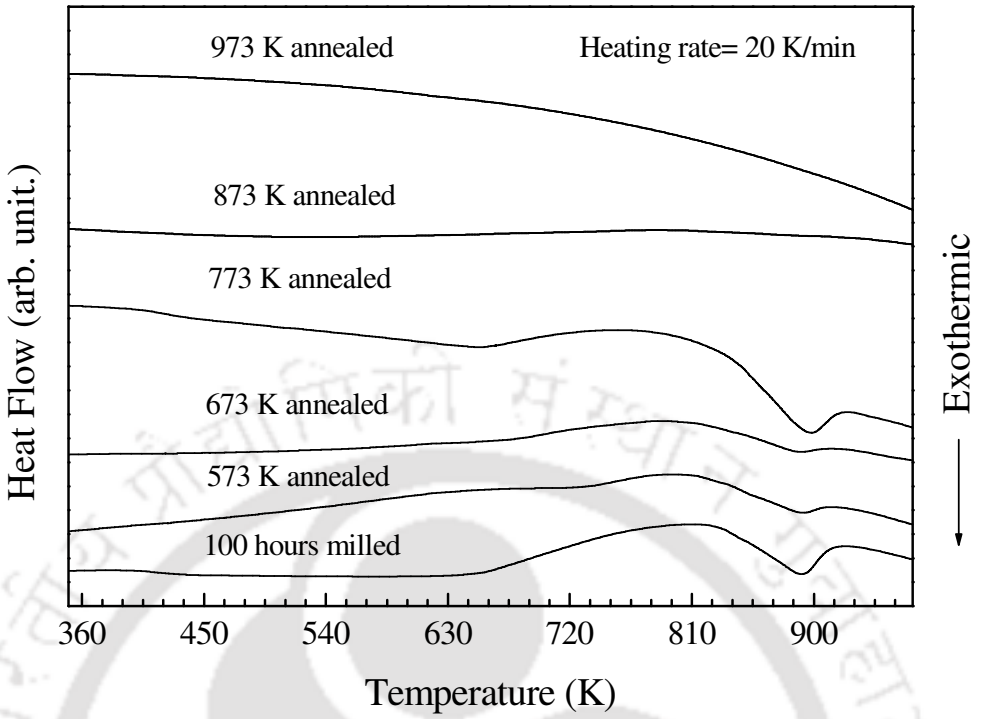

Figure 5.4: DSC curves of as-milled and annealed powders of $Fe_{75}Si_{15}Cr_{10}$.

Formation of the amorphous phase in the milled powders depends on many factors [74]. For the amorphization of any system, the free energy of the crystalline state has to be raised above that of the amorphous structure [68]. Incorporating dissimilar atoms in the matrix can raise the energy of the crystalline state by atomic (chemical) disorder [75]. The difference in structure and atomic radius of the constituent atoms play a crucial role in increasing the energy of the crystalline state of an alloy [76]. Further, large amounts of defects (dislocations and grain boundaries) introduced in the course of the milling process significantly increases the free energy of the system, which can lead to the amorphization of the powders. In the MA process, transmission of mechanical energy from the milling media to the powders and the rise of temperature inside the vial strongly influence the ultimate product of the milling process. Rise of temperature can

result in relaxation of strain (which can reduce the dislocation defects) as well as enhance the growth of crystallites. This means that only optimized milling conditions can lead to the formation of an amorphous structure. An earlier report [77] proposed that a small amount of Cr in Fe-Si based bulk glassy alloys can increase the glass forming ability as a result of the improved bonding among the constituent elements. The present studies demonstrate the optimal milling conditions for the synthesis of amorphous $Fe_{75}Si_{15}Cr_{10}$ powders.

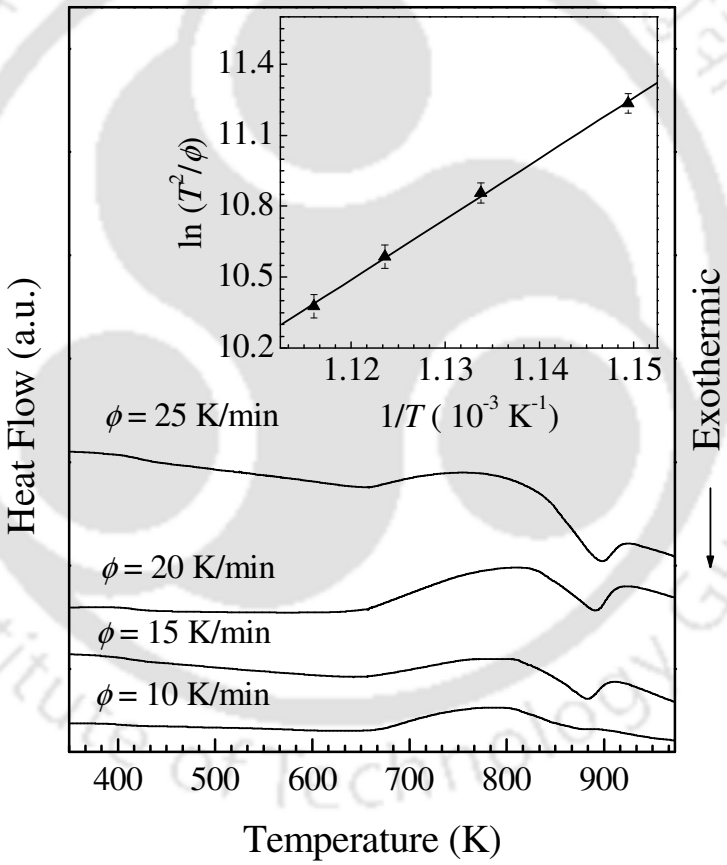

Figure 5.5: DSC curves of the 100 hours milled powders of $Fe_{75}Si_{15}Cr_{10}$ at different heating rates. Kissinger's plot corresponding to the data is shown in the inset.

DSC curves obtained at different heating rates are shown in Figure 5.5 These curves reveal that the crystallization peak temperature, T shifts with heating rate, ϕ. This behavior was used to calculate the activation energy of crystallization, E_A using Kissinger's relation [78]

$$\ln\frac{T^2}{\phi} = \frac{E_A}{RT} + C \qquad (5.1)$$

where R is a universal gas constant and C is a constant. Inset in Figure 5.5 shows the plot between $\ln(T^2/\phi)$ and $1/T$. E_A (= 213 ± 2 kJmol^{-1}) was estimated from the slope of a least squares fit to the data. This value is close to the value of 212 kJmol^{-1} estimated for lattice diffusion of Si (Cr) in microcrystalline, disordered bcc-Fe(Si,Cr) [79].

5.4. Magnetic properties

Figure 5.6 shows the magnetization versus temperature ($M - T$) plots of milled (for 100 hours), and the powders annealed at 873 K and 973 K. All the $M - T$ plots were recorded under a constant applied dc magnetic field of 100 Oe. The data of milled powders show a sharp decrease in M near 783 K, followed by a steady decrease from 823 K onwards. The former observation is related to the ferromagnetic to paramagnetic transition of the amorphous phase and the latter is associated with the crystallization of the amorphous powders. The ferromagnetic to paramagnetic transition of the crystalline phase observed in the $M - T$ plots of the milled powders has been shown as an inset in Figure 5.6. T_C of the crystallized powders are around 1020 K, which is slightly lower than the T_C of α–Fe (1043 K). The lower T_C may be related to the presence of Si and Cr in the Fe-matrix.

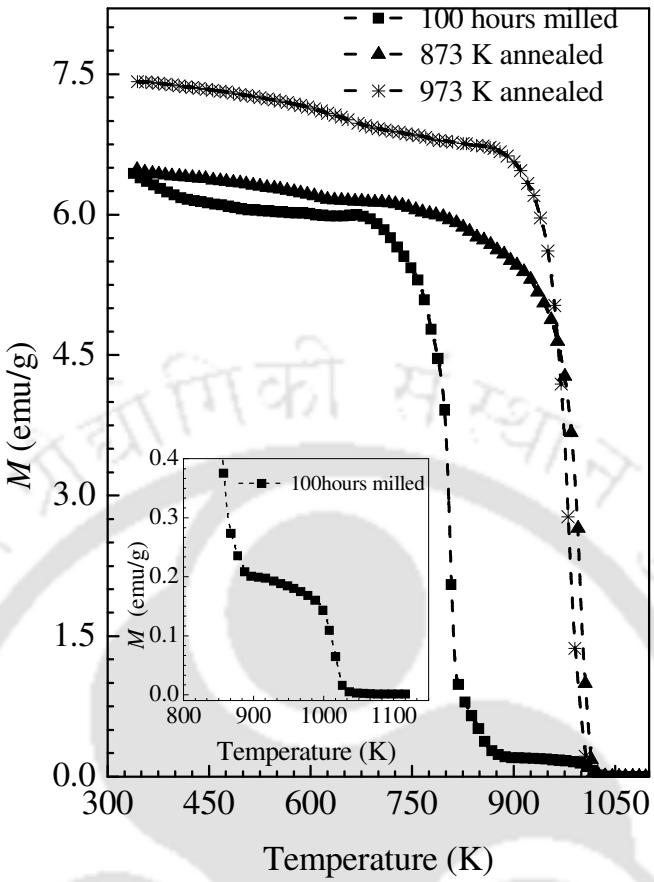

Figure 5.6: $M - T$ plots of $Fe_{75}Si_{15}Cr_{10}$ powders milled for 100 hours, and milled powders annealed at 873 and 973 K. $M - T$ plots were recorded under a field of 100 Oe.

In order to study the coercivity and saturation magnetization of the amorphous and nanocrystalline powders, room temperature hysteresis ($M - H$) loops were obtained. Figure 5.7 shows the $M - H$ loops of the powders annealed at different temperature [Figure 5.7(a)] and annealed at 873 K for different time periods [Figure 5.7(b)]. Figure 5.8 (a) shows the variation of coercivity and average magnetic moment per Fe atom (calculated at 20 kOe) of the milled and annealed powders. The coercivity of the as-milled powder is 262 Oe, which is much higher than the coercivity (~0.01 Oe) reported for melt-spun amorphous ribbons [9]. This may be attributed to the highly strained local

atomic order [80], which is strongly influenced by the large amounts of strain accumulated due to the plastic deformation occurring during the milling process. The coercivity value decreases for the powders annealed up to 773 K due to the release of strain, but increases with increasing annealing temperatures. This behavior is in contrary to those observed for melt-spun ribbons [23,81]. Since the average crystallite size of the powders annealed at 873 K is about 24 nm, it is well below the ferromagnetic exchange length of Fe-Si based alloys (which is typically about 35 nm [23]). Thus, from the considerations of the random anisotropy model [23], the effective anisotropy is expected to decrease resulting in a decrease in the coercivity of the powders. However, the increase in coercivity may be related to additional stresses induced during the annealing process [82,83]. In the presently investigated samples, some highly disordered (amorphous like) structure was observed within the nanocrystallites (*cf*. Figure 5.3 and the corresponding text in section 5.1 of this chapter). These disordered regions can contribute to the coercivity of the nanostructured phases. In order to further investigate the correlation between microstructure and coercivity of the nanostructured phases, the milled amorphous $Fe_{75}Si_{15}Cr_{10}$ powders were annealed at 873 K (near to the crystallization temperature) for different time periods and the results are depicted in figure 5.8(b). Although, the estimated crystallite size of the powder annealed at 873 K for 1 hour (16 nm) is well below the ferromagnetic exchange length of Fe-Si based materials, coercivity was found to be very high (400 Oe). Further, the coercivity increases with increasing annealing time periods. The source of this phenomenon may be due to a weak intergranular ferromagnetic coupling caused by the formation of a magnetic material with a low T_C and/or due to the development of additional disordered phases [84].

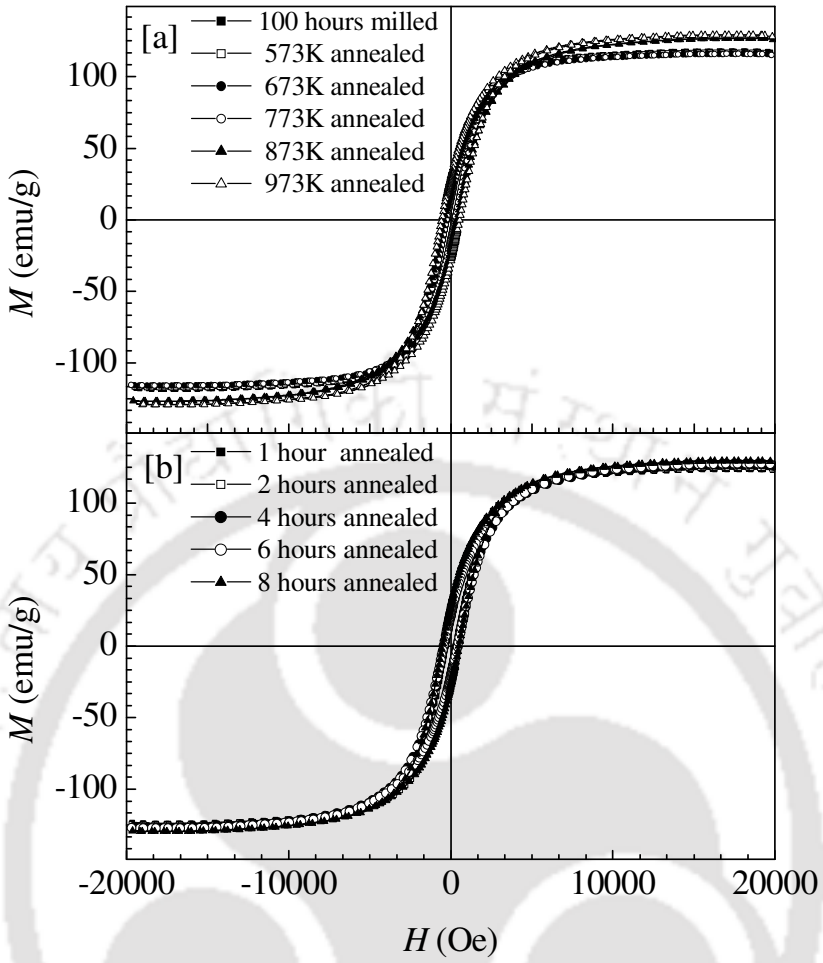

Figure 5.7: Room temperature $M - H$ loops of $Fe_{75}Si_{15}Cr_{10}$ powders (a) milled for 100 hours and annealed at different temperatures for 4 hours each, and (b) annealed at 873 K for various time periods.

The average magnetic moment per atom of Fe of the milled powders is $1.43\mu_B$ which is lower than that of α–Fe ($2.1\mu_B$). This could be due to the spatial variation of interatomic distances between the Fe neighbors which may decrease the average magnetic moments [54,55]. Further, presence of Si and Cr in the amorphous matrix can induce partial filling of *3d* bands of Fe by *3p* electrons, which can also contribute to the lowering of the average magnetic moments of Fe [35, 53]. The average magnetic moment

(μ) per Fe atom is nearly constant for the powders annealed up to 773 K. The increase in μ beyond 773 K may be related to the crystallization process and hence an improvement in the magnetic order. μ does not vary much when annealed for different times at 873 K.

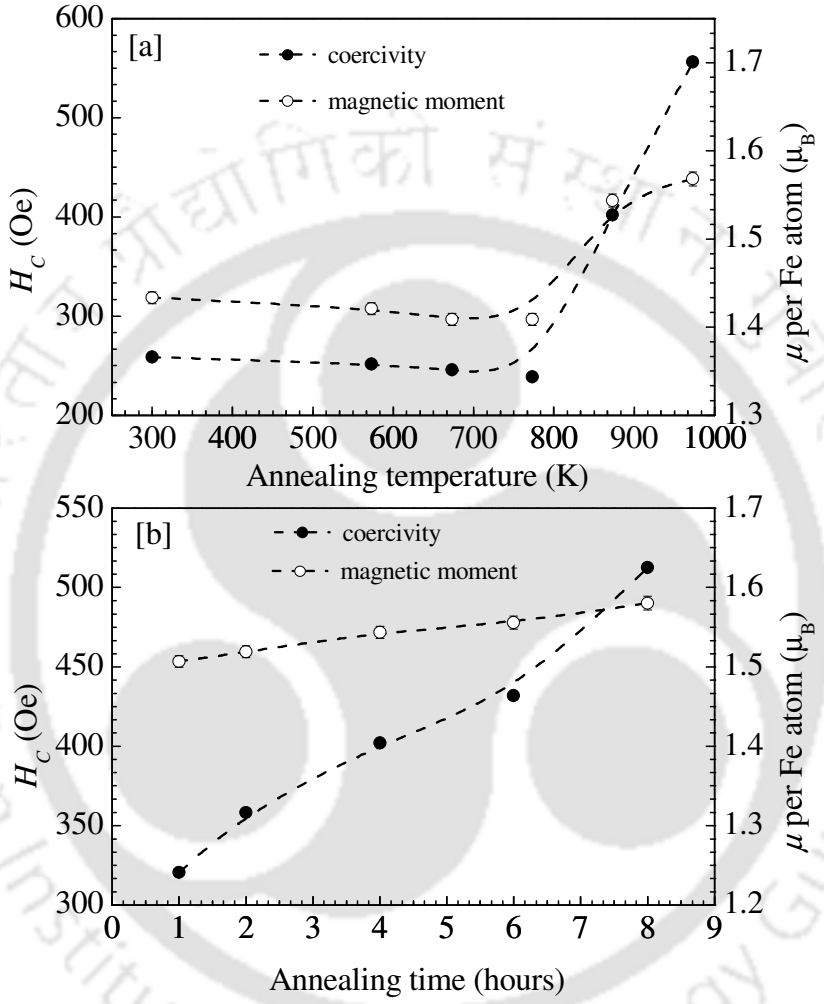

Figure 5.8: (a) H_C and μ per Fe atom of as-milled and annealed $Fe_{75}Si_{15}Cr_{10}$ powders. (b) H_C and μ of as-milled $Fe_{75}Si_{15}Cr_{10}$ powders annealed for different times at 873 K.

In order to further investigate the correlation between the microstructure and the magnetic properties, the effective anisotropy constant K_{eff} was calculated using the law of approach to saturation as discussed in chapter 3. Figure 5.9 shows the variation of K_{eff} of the powders annealed at 873 K with increasing annealing time. Inset in Figure 5.9 shows

the K_{eff} values for the powders annealed at 873 K and 973 K. The values of K_{eff} have been found to be ~10^5 Jm^{-3}, which are higher than that of bulk Fe (4.8×10^4 Jm^{-3}). The high K_{eff} values of the annealed powders can be due to the strain induced by the presence of the disordered phase within the crystallites as discussed earlier. A good correspondence between K_{eff} and coercivity has been observed in the present studies.

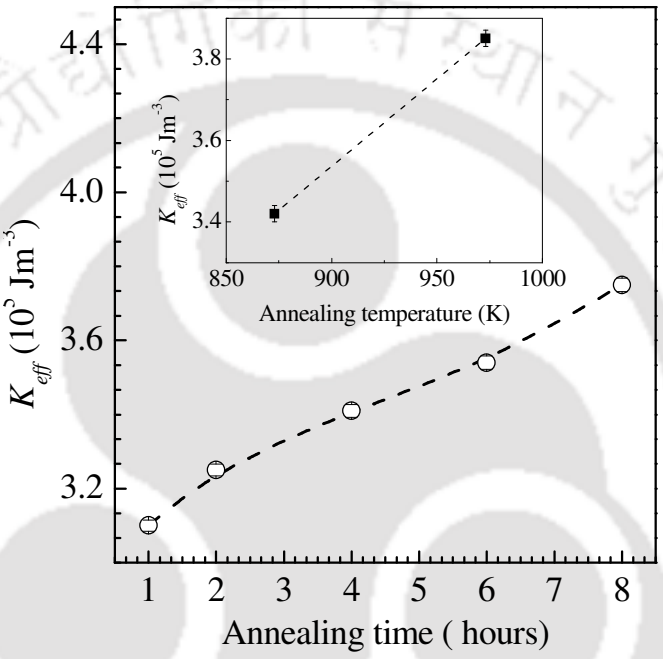

Figure 5.9: Variation of K_{eff} of $Fe_{75}Si_{15}Cr_{10}$ powders annealed at 873 K for various time periods. Inset: K_{eff} of $Fe_{75}Si_{15}Cr_{10}$ powders annealed at 873 and 973 K for 4 hours.

In amorphous materials, inhomogeneities acts as strong pinning sites and thereby influence the coercivity of the material [85]. In the case of nanocrystalline materials, defects such as the amorphous-like disordered regions inside the crystallites and grain boundaries can cause domain wall pinning and hence influence the coercivity. So, the possibility of domain wall pinning in the present samples was investigated by studying the coercivities of different minor $M - H$ loops. Figure 5.10 shows the variation of

coercivity (H_c) obtained from various minor $M - H$ loops, obtained with different maximum magnetic fields. Coercivity increases slowly [*cf.* inset in Figure 5.10] for lower applied fields and then abruptly attains saturation value at higher applied fields. The sluggish low-field behavior is an indication of domain wall pinning [62, 63].

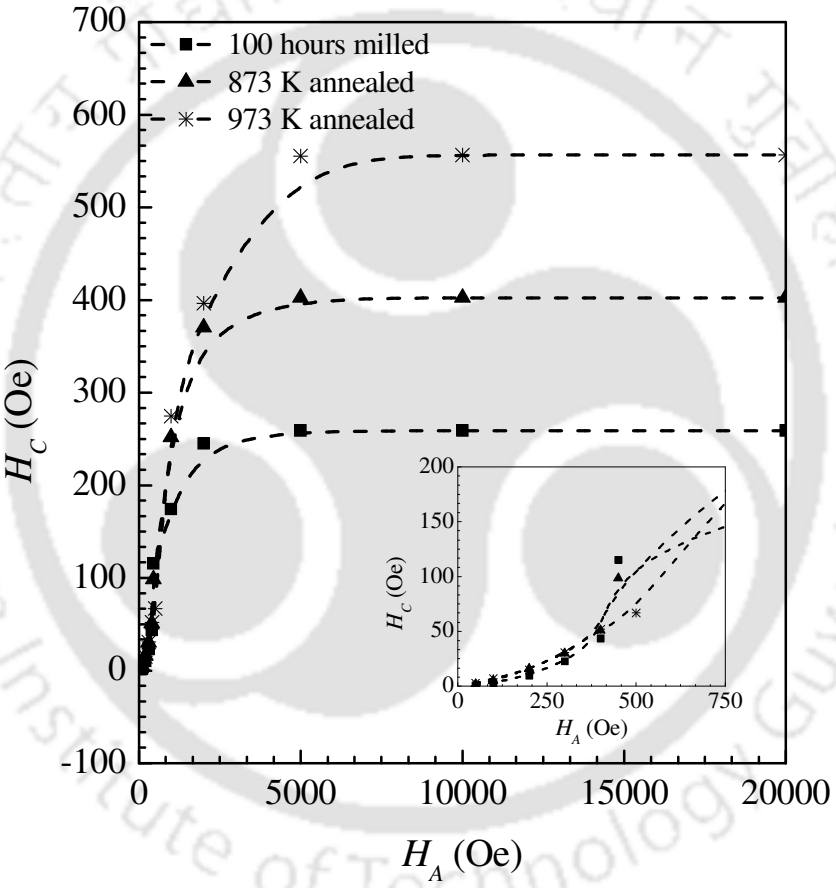

Figure 5.10: Minor hysteresis loop coercivity (H_C) of as-milled and annealed $Fe_{75}Si_{15}Cr_{10}$ powders as a function of applied field (H_A). Inset shows expanded view of the data close to the origin.

5.5. Summary

Fe-Si-Cr amorphous powders were synthesized by high energy ball milling in a planetary ball mill. Formation of the amorphous phase has been attributed to the high amounts of dislocation defects induced during the milling process and due to Cr addition to Fe-Si powders which improves the bonding nature among the constituent elements. Thermal studies reveal the crystallization temperature to be near to 873 K and the activation energy of crystallization to be 213 $kJmol^{-1}$ which is close to the value for lattice diffusion of Si (Cr) in microcrystalline, disordered bcc-Fe(Si,Cr). The average magnetic moment of the amorphous powders is lower than that of pure α-Fe which is attributed mainly to the spatial variation of nearest neighbor distances of the Fe atoms and presence of Si and Cr in Fe-matrix. Average magnetic moment of the powders has been observed to increase with the crystallization process. The increase of coercivity with increasing annealing temperature has been attributed to the possible development of additional stresses in the nanocrystallites due to the presence of some disordered atomic arrangements inside the nanocrystallites as revealed by TEM observations. The effective anisotropy of the nanocrystalline powders estimated using the law of approach to saturation shows good correspondence to the coercivity. Presence of domain wall pinning in both the amorphous and crystalline powders also supports the observed high coercivity of the powders.

Chapter 6

Conclusion and scope for future work

6.1. Conclusion

In this thesis work, nanocrystalline $Fe_{75}Si_{25}$, $Fe_{75}Si_{20}M_5$ and $Fe_{75}Si_{15}M_{10}$ (M = Al, B, Cr) powders were synthesized by mechanical alloying of elemental powders of appropriate composition. A systematic study of the evolution of structure and magnetic properties of the powders during the mechanical alloying process was carried out to understand the milling characteristics. The as milled powders were then given heat treatment at elevated temperatures and the changes occurring in the structure and magnetic properties of the powders during annealing were evaluated.

The modified Williamson-Hall method used for the estimation of crystallite size and lattice strain from the broadening of X-ray reflections of the mechanically alloyed powders was found to be more applicable as compared to the conventional Williamson-Hall method for the present samples. During the milling process, the average crystallite size of the powders decreases gradually to the order of 10 nm while the average dislocation density increases to the order of 10^{18} m^{-2} for milling time period of about 40 hours. Further, the

alloying of Fe and Si or Fe, Si and M powders have been found to be nearly complete with formation of non-equilibrium solid solutions α-Fe(Si) and α-Fe(Si,M), respectively after 40 hours of milling, as indicated by saturation values of structural parameters. Occurrence of atomic disorder during the milling process has been evidenced from the changes of the lattice parameters and magnetic moments of the powders. The coercivity of the powders increased with increasing milling time periods, which has been understood as consequence of particle size refinement and introduction of large amounts of dislocations during the course of milling. The presence of dislocations and grain boundaries increases the possibility of domain wall pinning in the milled samples. High Curie temperature of the powders as compared to melt-spun ribbons of similar compositions has been attributed to the excessive internal strains in the milled powders. Though, the correlation between the structure and magnetic properties of Fe-Si and Fe-Si-M powders has been found to be similar, the structural and magnetic parameters of each set of samples are distinctly different and strongly dependent on the alloy compositions.

Annealing of mechanically alloyed nanocrystalline Fe-Si and Fe-Si-M powders at elevated temperatures has significant effects on their structure and soft magnetic properties. Upon annealing, a gradual transformation of the non-equilibrium solid solution α-Fe(Si) phase in the as-milled powders to ordered DO_3 phase is observed. This structural transformation is accompanied by the growth of crystallite size and reduction of dislocation density as the annealing temperature is increased. The ordered DO_3 phase persists in annealed powders even after addition of 10 at.% of an additional element M (M=Al, B, Cr). The magnetic moments of the powders have been observed to be strongly dependent on the alloy compositions with $Fe_{75}Si_{25}$ ($Fe_{75}Si_{15}Cr_{10}$) powders showing the highest (lowest) values

under similar annealing conditions. Coercivity has been found to depend on crystallite size as predicted by random anisotropy model in a particular range of annealing temperatures when the dislocations defects have been reduced considerably after annealing. Although annealing causes significant improvement of the soft magnetic properties of the mechanically alloyed Fe-Si and Fe-Si-M powders with drastic decrease of coercivity at higher annealing temperatures, the residual defects present in the annealed powders contribute to their higher coercivity values. The correlation between structure and magnetic properties in annealed Fe-Si and Fe-Si-M powders has been found to be similar. However, the structural and magnetic parameters are strongly dependent on the alloy composition. $Fe_{75}Si_{15}Al_{10}$ powders annealed at 1223 K exhibit the lowest coercivity of 9 Oe among all the samples studied in this work. These results show that the dislocation defects introduced during milling could not be completely relieved by the annealing procedure adopted.

Although, nanocrystalline Fe-Si-Cr powders could be obtained by appropriate heat treatment of the mechanically alloyed amorphous precursors which is an alternative route of preparing nanocrystalline materials, the soft magnetic properties of nanocrystalline powder obtained by this process deteriorates instead of improving (as observed in melt spun ribbons). This unexpected result has been analyzed and attributed to the increase in effective anisotropy of the nanocrystalline powders due to the presence of disordered phases inside the highly strained nanocrystallites, which also enhances the possibility of domain wall pinning.

The present studies have brought out several interesting results which contribute to the understanding the evolution of magnetic properties of Fe-Si(-M) powders during milling and subsequent heat treatment. These studies have also revealed the strong correlation between structure and magnetic properties of Fe-Si and Fe-Si-M powders as well as the

possibility of improving the soft magnetic properties of mechanically alloyed Fe-Si(-M) powders.

6.2 Scope for future work

The present investigations on as milled and annealed powders of Fe-Si and Fe-Si-M (M = Al, B, Cr) have revealed that there are several aspects of interest in these materials. A study of the local atomic environment of Fe in powders milled for various time periods would help in understanding the mixing of Fe and Si (and M) and the way Si (and M) enter into α-Fe while forming the solid solution. Mossbauer studies on the disordered and ordered Fe-Si and Fe-Si-M powders would reveal the magnetic interactions in these two structures and might provide insights on reducing the magnetic hardening in these powders. Field cooled and zero field cooled low temperature investigations of these powders would also help in the understanding of the nature of the ordered and disordered phases. The natural process of introduction of dislocation defects during MA which results in high coercivity of the powders can be exploited to develop hard magnetic materials with enhanced coercivity. It is also worthy to investigate green compacted and sintered pellets of the above powders towards developing materials better suited for applications.

REFERENCES

[1] G. Herzer, *Physica Scripta* **T 49** (1993) 307.

[2] F. Ffeiffer and C. Radeloff, *J. Magn. Magn. Mater.* **19** (1980) 190.

[3] R. Boll and H. R. Hildnger, *IEEE Trans. Magn.* **MAG-19** (1983) 1946.

[4] Y. Yoshizawa, S. Oguma and K. Yamauchi, *J. Appl. Phys.* **64** (1988) 6044.

[5] W. F. Barrett, W. Brown and R. A. Hadfield, *Sci. Trans. R. Dublin Soc.* **7 (**1900) 7.

[6] D. Jiles, *Introduction to Magnetism and Magnetic Materials*, Chapman & Hall, Newyork, (1991).

[7] C. Suryanarayana, *Prog. Mater. Sci.* **46** (2001) 1.

[8] G. E. Fish, *Proceedings of IEEE* **78** (1990) 978.

[9] G. Herzer, *Proceedings of the NATO Advanced Study Insititute on Magnetic Hysteresis in Novel Materials* **338** (1996) 711.

[10] K. Suzuki, A. Makino, N. Kataoka, A. Inoue and T. Masumoto, *J. Appl. Phys.* **70** (1991) 6232.

[11] J. S. Benjamin and M. S. Bamford, *Metall. Trans.* **A8** (1977) 1301.

[12] J. R. Thompson and C. Politis, *Europhys. Lett.* **3** (1987) 199.

[13] C. C. Koch, *Nanostructured Mater.* **9** (1997) 13.

[14] H. J. Fecht, *Nanostructured Mater.* **6** (1995) 33.

[15] E. C. Stoner, *Phil. Mag*. **15** (1993) 1080.

[16] J. C. Slater, *Phys. Rev.* **49** (1936) 537.

[17] E. Stoner, *Proc. R. Soc. A* **165** (1938) 372.

[18] J. Janak, *Phys. Rev. B* **16** (1977) 255.

[19] R. Skomski, J. Coey, J. M. D. Coey and D. R. Tilley, *Studies in condensed matter physics*, Institute of Physics Publishing Ltd., (1999).

[20] S. Blundel, *Magnetism in condensed matter*, Oxford University Press, (2001).

[21] M. Johnson, P. Bloemen, F. den Broeder and J. de Vries, *Rep. Prog. Phys.* **59** (1996) 1409.

[22] A. Mager, *Ann. Phys.* **6 F** (1952) 15.

[23] G. Herzer, *IEEE Trans. Magn.* **26** (1990) 1397.

[24] R. Alben, J. J. Baker and M. C. Chi , *J. Appl. Phys.* **49** (1978) 1653.

[25] R. M. Bozorth, *Ferromagnetism*, Princeton, N. J.: D. Van Nostrand, (1951).

[26] T. J. Zhou, Z. Yu and Y. W. Du, *J. Magn. Magn. Mater.* **202** (1999) 354.

[27] J. Ding, Y. Li, L. F. Chen, C. R. Deng, Y. Shi, Y. S. Chow and T. B. Gang, *J. Alloys Compd.* **314** (2001) 262.

[28] S. Miragheai, P. Abachi, H. R. M. Hosseini and A. Bahrami, *J. Mater. Process. Tech.* **203** (2008) 554.

[29] C. Kuhrt and L. Schultz, *IEEE Trans. Magn.* **29** (1993) 2667.

[30] R. Koohkan, S. Sharafi, H. Shokrollahi and K. Janghorban, *J. Magn. Magn. Mater.* **320** (2008) 1089.

[31] Y. D. Kim, J. Y. Chung, J. Kim and H. Jeon, *Mater. Sci. Eng. A* **291** (2000) 17.

[32] S. Azzaza, S. Alleg, H. Moumeni, A. R. Nemamcha, J. L. Rehspringer and J. M. Greneche, *J. Phys.: Condens. Matter* **18** (2006) 7257.

[33] S. Guessasma and N. Fenineche, *J.Magn. Magn. Mater.* **320** (2008) 450.

[34] M. M. Raja, K. Chattopadhyay, B. Majumder and N. A. Narayanasamy, *J. Alloys Compd.* **297** (2000) 199.

[35] T. D. Shen, R. B. Schwarz and J. D. Thompson, *Phys. Rev. B* **72** (2005) 014431.

[36] T. D. Shen, K. Y. Wang, M. X. Quan and J. T. Wang, *J. Mater. Sci. Lett.* **11** (1992) 1576.

[37] A. Bahrami, H. R. M. Hosseini, P. Abachi and S. Miragheai, *Mater. Lett.* **60** (2006) 1068.

[38] E. Fechova, P. Kollar, J. Fuzer, J. Kovac, P. Petrovic and V. Kavekansky, *Mater. Sci. Eng. B* **107** (2004) 155.

[39] J. J. Sunol, L. Escoda, J. Fort, J. Perez and T. Pujol, *Mater. Lett.* **62** (2008) 1673.

[40] R. J. Perez, B. L. Huang, P. J. Crawford, A. A. Sharif and E. J. Lavernia, *Nanostructured Mater.* **7** (1996) 47.

[41] B. Zuo, N. Saraswati, T. Sritharan and H. H. Hng, *Mater. Sci. Eng. A* **371** (2004) 210.

[42] O. Kohomoto, N. Yamaguchi and T. Mori, *J. Mater. Sci.* **29** (1994) 3221.

[43] J. Q. Marcatoma, V. A. P. Rodriguez and E. M. B. Saitovitch, *Hyperfine Interactions*, **148/149** (2003) 97.

[44] R. Pizzaro, J. M. Barandiaran, F. Plazaola and J. Gutierrez, *J. Magn. Magn. Mater.* **203** (1999) 143.

[45] R. B. Schwarz, T. D. Shen, U. Harms and T. Lillo, *J. Magn. Magn. Mater* **283** (2004) 223.

[46] K. Inomata, M. Hasegawa and S. Shimauki, *IEEE Trans. Magn.* **MAG-17** (1981) 3076.

[47] B. D. Cullity and S. R. Stock, *Elements of X-ray Diffractions*, third ed., Prentice Hall, Upper Saddle River, N J, (2001).

[48] G. K. Williamson and W. H. Hall, *Acta Meteri.* **1** (1953) 22.

[49] T. Ungar and G. Tichy, *Phys. Status Solidi A***171** (1999) 425.

[50] T. Ungar, I. Dragomir, A. Revesz and A. Borbely, *J. Appl. Cryst.* **32** (1999) 992.

[51] A. Revesz, T. Ungar, A. Borbely and J. Lendvai, *Nanostruct. Mater.* **7** (1996) 779.

[52] M. O. Lai and L. Lu, *Mechanical Alloying*, Kluwer Academic, Boston, (1998).

[53] C. Djega-Mariadassou, L. Bessais, A. Nandra and J. M. Greneche, *Phys. Rev. B* **65** (2001) 014419.

[54] D. M. Blanco, P. Gorria and J. A. Blanco, *J. Magn. Magn. Mater.* **300** (2006) e339.

[55] D. M. Blanco, P. Gorria, J. A. Blanco, M. J. Perez and J. Campo, *J. Phys: Condens. Matter* **20** (2008) 335213.

[56] L. Neel, Annales Univ. Grenoble **22** (1946) 299.

[57] A. Hubert and R. Schafer, *Magnetic Domains, Analysis of microstructure*, Springer-Verlag, Berlin, (1998).

[58] A. Hernando, P. Martin, M. Lopez, T. Kulik, L. K. Verga and G. Hadjipanayis, *Phys. Rev. B* **69** (2005) 052501.

[59] W. S. Rasband, *Image J*, U. S. National Institutes of Health, Bethesda, Maryland, USA, http: //*rbs.info.nih.gov*/ij/, 1997-2008.

[60] S. V. Andreev, M. I. Bartashevich, V. I. Pushkarsky, V. N. Maltsev, A. Pamyatnykh, E. N. Tarasov, N. V. Kudravatykh and T. Goto, *J. Alloys Compd.* **260** (1997) 196.

[61] B. H. Liu, J. Ding, Z. L. Dong, C. B. Boothroyd, J. H. Yin and J. B. Yi, *Phys. Rev. B* **74** (2006) 184427.

[62] J. Zhang, S. Zhang, H. Zhang and B. Shen, *J. Appl. Phys.* **89** (2001) 5601.

[63] G. C. Hadjipanayis and A. Kim, *J. Appl. Phys.* **63** (1988) 3310.

[64] L. K. Varga, F. Mazaleyrat, J. Kovac and J. M. Greneche, *J. Phys: Condens. Matter* **14** (2002) 1895.

[65] F. L. Tang and X. Zhang, *Comput. Mater. Sci.* **40** (2007) 434.

[66] W. A. Hines, A. H. Menotti, J. I. Budnick, T. J. Burch, T. Litrenta, V. Niculescu and K. Raj, *Phys. Rev. B* **13** (1976) 4060.

[67] B. Zuo and T. Sritharan, *Acta Mater.* **53** (2005) 1233.

[68] H. Bakker, G. F. Zhou and H. Yang, *Prog. Mater. Sci.* **39** (1995) 159.

[69] T. D. Zhou, L. J. Deng and D. F. Liang, *Acta Metall. Sin. (Eng.Lett.)* **21** (2008) 191.

[70] J. W. Cable, L. David and R. Parra, *Phys. Rev. B* **16B** (1977) 1132.

[71] R. J. Perez, B. Huang, P. J. Crawford, A. A. Sharif and E. Lavernia, *Mater. Sci. Eng. A* **204** (1995) 217.

[72] A. L. Greer, *Thermochim. Acta* **42** (1980) 193.

[73] H. J. Jin, P. Wen and K. Lu, *Appl. Phys. Lett.* **83** (2003) 3284.

[74] A. Inoue, T. Zhang and T. Masumoto, *J. Non-Cryst. Solids* **156-158** (1993) 473.

[75] G. J. Fan, F. Q. Guo, Z. Q. Hu, M. X. Quan and K. Lu, *Phys. Rev. B* **55** (1997) 11010.

[76] X. Cheng, Y. Ouyang, H. Shi, X. Zhong, Y. Du and X. Tao, *J. Alloys Compd.* **421** (2006) 314.

[77] B. Shen, M. Akiba and A. Inoue, *J. Appl. Phys.* **100** (2006) 043523.

[78] H. E. Kissinger, *Anal. Chem.* **29** (1957) 1702.

[79] M. Salamon and H. Mehrer, *Philos. Mag. A* **79** (1999) 2137.

[80] J. M. D. Coey, *J. Appl. Phys.* **49** (1978) 1646.

[81] F. Shahri, A. Beitollahi, S. G. Shabestari and S. Kamali, *Phys. Rev. B* **76** (2007) 024434.

[82] H. Q. Guo, H. Kronmuller, T. Dragon, Z. H. Cheng and B. G. Shen, *Phys. Rev. B* **62** (2000) 5760.

[83] V. Franco, C. F. Conde and V. Conde, *J. Magn. Magn. Mater.* **185** (1998) 353.

[84] M. Miura and A. Obata, *IEEE Trans. Magn.* **32** (1996) 1952.

[85] T. Bitoh, A. Makino and A. Inoue, *J. Appl. Phys.* **99** (2006) 08F102.

PUBLICATIONS

IN JOURNALS:

1. Structural analysis of mechanically alloyed nanocrystalline $Fe_{75}Si_{15}Al_{10}$ powders, **M. P. C. Kalita,** A. Perumal and A. Srinivasan**,** *Mater. Lett.* **61** (2006) 824.

2. Microstructure and magnetic properties of nanocrystalline $Fe_{75}Si_{20}M_5$ (M = Al, B, Cr) powders, **M. P. C. Kalita,** A. Perumal and A. Srinivasan**,** *J. Phys D: Appl. Phys.* **41** (2008) 165002.

3. Structure and magnetic properties of nanocrystalline $Fe_{75}Si_{25}$ powders prepared by mechanical alloying, **M. P. C. Kalita,** A. Perumal and A. Srinivasan**,** *J. Magn. Magn. Mater.* **320** (2008) 2780.

4. Properties of nanocrystalline $Fe_{75}Si_{15}M_{10}$ (M – Cr, Al) powders prepared by mechanical alloying, **M. P. C. Kalita,** A. Perumal, A. Srinivasan, B. Pandey and H.C.Verma, *J. Nano. Sci. Nano Tech.* **8** (2008) 4314.

5. Mixing characterization of mechanically milled $Fe_{75}Si_{15}M_{10}$ powders using Mossbauer spectroscopy, B. Pandey, **M. P. C. Kalita**, A. Perumal, A. Srinivasan and H. C. Verma, *Hyperfine Interact.* (2008) (available on line: doi:10.1007/s 10751-008-9781-y).

6. Magnetic properties of nanostructured Fe-Si-Cr powders prepared from mechanically alloyed amorphous precursor, **M. P. C. Kalita,** A. Perumal and A.Srinivasan (communicated).

7. Evolution of atomic order and soft magnetism in mechanically alloyed nanocrystalline Fe-Si powders, **M. P. C. Kalita,** A. Perumal and A. Srinivasan (to be communicated).

8. Effect of heat treatment on structure and soft magnetic properties of Fe-Si-M (M = Al, B, Cr) powders, **M. P. C. Kalita,** A. Perumal and A. Srinivasan (to be communicated).

IN CONFERENCES:

1. Synthesis of DO_3 structured Fe-Si-Al nanocrystalline powders, **M. P. C. Kalita**, A. Perumal and A. Srinivasan, *Proc. DAE-Solid State Phys. Symposium* (Mumbai) **50** (2005) 215.

2. Preparation of non-equlibrium solid solutions of $Fe_{75}Si_{15}M_{10}$ powders by mechanical alloying, **M. P. C. Kalita**, A. Perumal and A. Srinivasan, *Proc. DAE-Solid State Phys. Symposium* (Bhopal) 2006 **51** (2007) 321.

3. Magnetic properties of mechanically alloyed nanocrystalline $Fe_{75}Si_{15}B_{10}$ powders, **M.P.C. Kalita**, A. Perumal and A. Srinivasan, *Proc. DAE-Solid State Phys. Symposium* (Mysore) **52** (2007) 385.

4 Effect of heat treatment on nanocrystalline $Fe_{75}Si_{25}$ and $Fe_{75}Si_{15}Cr_{10}$ powders, **M. P. C. Kalita**, A. Perumal and A. Srinivasan, *Physics Academy of North East (PANE)* Guwahati (2007).

****